

**AFRL-ML-WP-TR-1998-4209**

**CONTRIBUTIVE RESEARCH & DEVELOPMENT  
VOLUME 130: THE ROLE OF MECHANICS IN  
MICROELECTROMECHANICAL SYSTEMS  
(MEMS) TECHNOLOGY**



**ROBERTO BALLARINI**

**SYSTRAN CORPORATION  
4126 LINDEN AVENUE  
DAYTON, OH 45432**

**OCTOBER 1998**

**FINAL REPORT FOR 11/17/1997 – 09/30/1998**

**APPROVED FOR PUBLIC RELEASE; DISTRIBUTION UNLIMITED**

**MATERIALS AND MANUFACTURING DIRECTORATE  
AIR FORCE RESEARCH LABORATORY  
AIR FORCE MATERIEL COMMAND  
WRIGHT-PATTERSON AIR FORCE BASE OH 45433-7750**

**19990406 078**

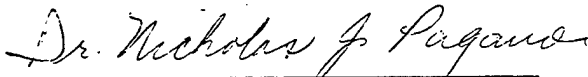
*[Faint, illegible stamp or mark]*

NOTICE

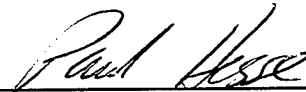
When Government drawings, specifications, or other data are used for any purpose other than in connection with a definitely related Government procurement operation, the United States Government thereby incurs no responsibility nor any obligation whatsoever; and the fact that the government may have formulated, furnished, or in any way supplied the said drawings, specifications, or other data, is not to be regarded by implication or otherwise as in any manner licensing the holder or any other person or corporation, or conveying any rights or permission to manufacture, use, or sell any patented invention that may in any way be related thereto.

This report has been reviewed by the Office of Public Affairs (ASC/PA) and is releasable to the National Technical Information Service (NTIS). At NTIS, it will be available to the general public, including foreign nations.

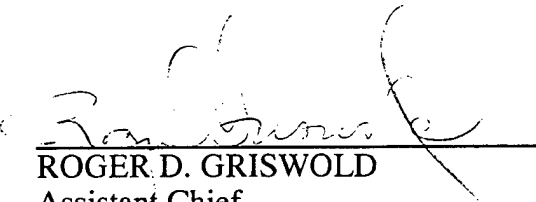
This technical report has been reviewed and is approved for publication.



DR. NICHOLAS J. PAGANO  
Project Engineer  
Mechanics & Surface Inter. Branch  
Nonmetallic Materials Division



MAJOR PAUL J. HESSE, USAF  
Chief  
Mechanics & Surface Inter. Branch  
Nonmetallic Materials Division



ROGER D. GRISWOLD  
Assistant Chief  
Nonmetallic Materials Division  
Materials & Manufacturing Directorate

“If your address has changed, if you wish to be removed from our mailing list, or if the addressee is no longer employed by your organization please notify AFRL/MLBC, Bldg. 654, 2941 P St., Suite 1, W-PAFB, OH 45433-7750 to help us maintain a current mailing list.”

Copies of this report should not be returned unless return is required by security considerations, contractual obligations, or notice on a specific document.

# REPORT DOCUMENTATION PAGE

FORM APPROVED  
OMB NO. 0704-0188

Public reporting burden for this collection of information is estimated to average 1 hour per response, including the time for reviewing instructions, searching existing data sources, gathering and maintaining the data needed, and completing and reviewing the collection of information. Send comments regarding this burden estimate or any other aspect of this collection of information, including suggestions for reducing this burden, to Washington Headquarters Services, Directorate for Information Operations and Reports, 1215 Jefferson Davis Highway, Suite 1204, Arlington, VA 22202-4302, and to the Office of Management and Budget, Paperwork Reduction Project (0704-0188), Washington, DC 20503.

<b>1. AGENCY USE ONLY (Leave Blank)</b>		<b>2. REPORT DATE</b> October 1998	<b>3. REPORT TYPE AND DATES COVERED</b> Final 11/17/97 - 09/30/98
<b>4. TITLE AND SUBTITLE</b> Contributive Research & Development Volume 130: The role of Mechanics in Microelectromechanical Systems (MEMS) Technology		<b>5. FUNDING NUMBERS</b> C F33615-94-C-5804 PE 62102F PR 4349 TA L0 WU VS	
<b>6. AUTHOR(S)</b> Roberto Ballarini		<b>8. PERFORMING ORGANIZATION REPORT NUMBER</b>	
<b>7. PERFORMING ORGANIZATION NAME(S) AND ADDRESS(ES)</b> SYSTRAN Corporation 4126 Linden Avenue Dayton, OH 45432		<b>10. SPONSORING/MONITORING AGENCY REP NUMBER</b> AFRL-ML-WP-TR-1998-4209	
<b>9. SPONSORING MONITORING AGENCY NAME(S) AND ADDRESS(ES)</b> Materials & Manufacturing Directorate Air Force Research Laboratory, Air Force Materiel Command Wright-Patterson AFB, OH 45433-7734 POC: Dr. Nicholas J. Pagano, AFRL/MLBC, (937) 255-6762		<b>11. SUPPLEMENTARY NOTES</b>	
<b>12a. DISTRIBUTION/AVAILABILITY STATEMENT</b> Approved for Public Release; Distribution is Unlimited.		<b>12b. DISTRIBUTION CODE</b>	
<b>13. ABSTRACT</b> This report present a review of recent developments in experimental and theoretical studies of the mechanical behavior of polycrystalline silicon for microelectromechanical systems (MEMS), and defines research needs to predict the life and strength of MEMS devices.			
<b>14. SUBJECT TERMS</b> Microelectromechanical Systems (MEMS), Tensile Strength, Fracture Toughness, Electrostatic Actuation, Polycrystalline Silicon (Poly-Si), Modulus of Elasticity, Subcritical Crack Growth.		<b>15. NUMBER OF PAGES</b> 156	
<b>17. SECURITY CLASSIFICATION OF REPORT</b> Unclassified		<b>18. SECURITY CLASS OF THIS PAGE.</b> Unclassified	<b>16. PRICE CODE</b>
<b>19. SECURITY CLASS OF ABSTRACT</b> Unclassified		<b>20. LIMITATION ABSTRACT</b> SAR	

Standard Form 298 (Rev 2-89)  
Prescribed by ANSI Std Z239-18  
298-102

## CONTENTS

List of Figures	iv
List of Tables	ix
Preface	x
Summary	1
Chapter 1: Variations in Mechanical Properties of Polysilicon	5
Chapter 2: Laboratory Failure of a MEMS Device	9
Part I: Review of Experimental Work	11
Chapter 3: Toyota Central Research and Development Laboratories	12
Chapter 4: Johns Hopkins University	33
Chapter 5: Berkeley Sensor and Actuator Center	48
Chapter 6: Exponent Analysis	56
Chapter 7: Case Western Reserve University	60
Chapter 8: Cornell University and University of Illinois at Urbana-Champaign	86
Part II: Review of Theoretical Work	92
Chapter 9: Statistical Methods for Predicting Elastic Constants of Polycrystalline Films	93
Chapter 10: The Effects of Heterogeneity and Anisotropy on Crack-Tip Parameters in Cracked Polycrystalline Films	112
Part IV: Suggestions for Future Research	143



## LIST OF FIGURES

### Chapter 2

- Figure 1 A MEMS device that fractured under the combination of cyclic mechanical stress, high electric field, and humid air. 9

### Chapter 3

- Figure 1 Schematic drawing of tensile testing using an electrostatic force gripping system. 13
- Figure 2 Tensile test procedure using electrostatic force. 14
- Figure 3 Thin film specimen for (a) uniform tension, (b) fracture toughness. 15
- Figure 4 Fabrication process (a) deposition of films, (b) patterning of poly-Si and Al films, (c) sacrificial etching to release poly-Si. 18
- Figure 5 SEM micrograph of three typical specimens. 19
- Figure 6 SEM micrograph of poly-Si film crystallized at (a) 600°C, (b) 700°C, and (c) 1000°C. Note the difference in grain size with increasing temperature. 19
- Figure 7 SEM chamber testing environment. 20
- Figure 8 SEM micrograph of tensile testing. Note that the specimen is subjected to eccentric loading, as evidenced by its bent shape. 21
- Figure 9 Tensile strength for different gage lengths. 23
- Figure 10 Tensile strength of poly-Si thin film; (a) undoped film, (b) P-doped film. 24
- Figure 11 Measured fracture probability as a function of tensile stress. The curve is fitted to Weibull distribution function. 26
- Figure 12 Tensile strength of poly-Si films for various annealing conditions (and grain size). 27
- Figure 13 Fracture toughness of poly-Si films for various annealing conditions (and grain size). 28
- Figure 14 Fracture surface of poly-Si thin film. 30
- Figure 15 Weibull plots normalized by the volume, surface area, and side surface area. 31

### Chapter 4

- Figure 1 Schematic of the test set-up. 35
- Figure 2 Schematic of the ISDG. 36
- Figure 3 SEM photo of the biaxial strain gage. 36
- Figure 4 A polysilicon specimen mounted in the grips of the test machine with the support strips cut. 37
- Figure 5 TEM photograph of the two-layer polysilicon specimen. The bottom layer is 2.0  $\mu\text{m}$  thick and the darker top layer is 1.5  $\mu\text{m}$  thick. 38
- Figure 6 Schematic of; (a) poly-Si pattern, (b) back-etch process as viewed at

	section A-A of (a).	39
Figure 7	SEM micrograph of tensile specimen.	40
Figure 8	A typical stress biaxial-strain plot.	41
Figure 9	Schematic of fracture specimen.	42
Figure 10	Close-up of the center crack and the gold pads.	42
Figure 11	Measured stress versus COD and comparison with theory.	43
Figure 12	Schematic of testing environment.	44
Figure 13	Eighteen specimens on a one square centimeter die.	45
Figure 14	Schematic of the specimen, with dimensions in $\mu\text{m}$ . The length, thickness, and width vary, as described in the text.	45
Figure 15	Force-displacement (left) and stress-strain (right) plots of two specimens identical in shape, but of different thickness.	46
Figure 16	Modulus and strength data for specimens of various sizes.	46

## Chapter 5

Figure 1	SEM micrograph of fracture structure test device. The six cantilever beams to be tested are attached to a shuttle which is anchored by a folded flexure structure.	48
Figure 2	Scanned video image of fracture structure test device. An off chip probe loads the shuttle of the device. Here the shortest two beams have already broken off as other beams continue to be bent.	50
Figure 3	Scanned video image of a $2.8 \mu\text{m}$ wide by $1.9 \mu\text{m}$ thick beam at a large displacement. The distance from the fixed end of the beam to the contact point is $70 \mu\text{m}$ . The beam has deflected $21.6 \mu\text{m}$ .	51
Figure 4	SEM of cantilever "beams" used for determining Young's modulus.	53
Figure 5	Plot of displacement vs. beam length for three different force settings using the Young's modulus test device.	54
Figure 6	Load-deflection for silicon whiskers at several temperatures.	55

## Chapter 6

Figure 1	In-plane resonant fatigue device.	57
Figure 2	Close-up view of notched cantilever specimen.	58
Figure 3	Time to failure versus normalized excitation.	58

## Chapter 7

Figure 1	Microstructure of polysilicon microfracture specimens: (a) shows a typical specimen; (b) shows, for an undoped CVD film, a planar view (top picture) micrograph of the grain and twin boundaries, and a cross-sectional TEM (bottom picture); (c) shows, for a boron doped CVD film, a planar view (top picture) micrograph of the grain structure, and a cross-sectional TEM (bottom picture).	62
----------	---	----

Figure 2	(a) Micrograph of wedge loaded microfracture specimen; (b) schematic drawing of microfracture specimen; (c) variables and nominal dimensions used in the mathematical model.	65
Figure 3	SEM micrograph of a fractured 6 $\mu\text{m}$ ligament B-doped specimen. The crack path is almost entirely transgranular.	66
Figure 4	(a) Sketch of two sets of interdigitated comb fingers; when a voltage is applied across this comb drive, the movable fingers will move to the left; (b) schematic drawing of the fracture device which consists of an actuator (in this sketch, the actuator has 18 pairs of comb fingers acting in parallel) and a fracture mechanics specimen.	69
Figure 5	Cross-sectional drawings depicting the device fabrication sequence: i) a thick $\text{SiO}_2$ film is grown on a silicon substrate, followed by LPCVD deposition of a polysilicon film and a $\text{SiO}_2$ film; ii) using photolithography, the device is patterned, and the top $\text{SiO}_2$ and polysilicon films are sequentially etched; iii) the top $\text{SiO}_2$ film is completely removed, and the polysilicon film is boron-doped; iv) the device is time-released in hydrofluoric acid, such that some $\text{SiO}_2$ remains beneath the large anchor pads, while the smaller features are fully released and free to move.	70
Figure 6	Transmission electron micrograph showing the microstructure of the polysilicon.	71
Figure 7	(a) SEM image of the entire fracture device (viewed at a $45^\circ$ angle); (b) a close-up of the fracture mechanics specimen; (c) a top view of the fracture mechanics specimen (rotated $90^\circ$ ) showing the dimensions (in $\mu\text{m}$ ); (d) one of the device's long support beams, buckled as-fabricated due to compressive residual stresses; (e) a high magnification image showing several of the comb fingers; the fixed and movable combs are not co-planar.	72
Figure 8	Finite element calculations showing displacements of a boron-doped device under a 600 $\mu\text{N}$ electrostatic load. The sketch greatly exaggerates the displacements; the original position of the device is outlined in blue.	77
Figure 9	Finite element calculations showing (a) the discretization of the specimen geometry and the contours of displacement magnitude and (b) the contours of maximum tensile stress in the region surrounding the notch tip.	78
Figure 10	The displacement of the fracture device versus the square of the applied voltage; the device fractured at 8.3 $\mu\text{m}$ .	79
Figure 11	S-N curves (stress to failure versus number of cycles to failure) curve for fatigue fracture.	82
Figure 12	a) SEM image of a fractured specimen, top view; b) the fracture surface of a doped specimen; c) higher magnification image of the area surrounding the crack initiation site; d) the fracture surface of an undoped specimen; e) higher magnification.	83

## Chapter 8

Figure 1	(a) Schematic (not to scale) of microinstrument and torsion sample. (b) SEM micrograph.	87
Figure 2	A calibrating beam and part of the actuator that it calibrates.	88
Figure 3	Close-up of torsion pillar.	89
Figure 4	Optical microscope close-up of buckling beam. The circles denote the deflection predicted by theory.	90
Figure 5	Twisting of a torsion sample recorded under an optical microscope.	91

## Chapter 9

Figure 1	Schematic diagram of crystal orientations in (a) $\{100\}$ , and (b) $\{110\}$ thin film textures, showing in-plane rotations, $\psi$ .	93
Figure 2	Poisson-Voronoi tessellation of microstructure for $n$ -grains ( $n=5-1000$ ).	96
Figure 3	Scatter of silicon's nominal plane strain Young's modulus $\bar{E}^n$ as a function of number of grains $n$ .	100
Figure 4	Mean value of normalized nominal plane strain Young's modulus $\bar{E}^n / \bar{E}^{isotropic}$ as functions of anisotropy parameter $A$ .	102
Figure 5	Mean value of nominal Poisson's ratio $\nu^n$ as functions of anisotropy parameter $A$ .	103
Figure 6	Coefficient of variation of nominal plane strain Young's modulus $\bar{E}^n$ as a function of number of grains $n$ .	104
Figure 7	Standard deviation of nominal Poisson's ratio $\nu^n$ as functions of anisotropy parameter $A$ .	105
Figure 8	Random field model.	107
Figure 9	Beam in tension (a), flexure (b), finite element model of moving window.	108
Figure 10	One realization of the (Young's modulus) random field.	110
Figure 11	Comparison of beam deflection using multicrystalline finite element calculations and using analytic-geometric closed form solutions.	110
Figure 12	Comparison of beam deflection using multicrystalline finite element calculations and using analytic-geometric closed form solutions.	111

## Chapter 10

Figure 1	Poisson-Voronoi tessellation of a crack in an aggregate of crystals.	117
Figure 2	Average values of normalized plane strain Young's modulus and Poisson's ratio as functions of anisotropy parameters; $\bar{\nu} = 0.0, 0.1, 0.2, 0.3, 0.4, 0.5$ .	118

Figure 3	Distributions of average plane strain modulus.	119
Figure 4	A schematic representation of the regions dominated by distinct asymptotics.	121
Figure 5	Fraction of occurrences of local stress intensity factor for highly anisotropic cubic crystals.	125
Figure 6	Fraction of occurrences of local stress intensity factor for highly anisotropic, slightly orthotropic crystals.	126
Figure 7	Fraction of occurrences of local stress intensity factor for highly anisotropic orthotropic crystals.	127
Figure 8	Scatter of normalized stress ahead of crack for several values of $n$ ( $\lambda=1$ , $A=9$ , $\bar{\nu} = 0.4$ ).	130
Figure 9	Scatter of normalized stress ahead of crack for several values of $n$ ( $\lambda=10$ , $A=9$ , $\bar{\nu} = 0.4$ ).	131
Figure 10	Fracture specimen with columnar microstructure.	138
Figure 11	Analysis of $\Delta K$ induced by remote grains: (a) specimen (b) reference grain.	139
Figure 12	Finite element mesh: (a) grain that contains the crack tip (b) remaining grains.	141
Figure 13	Normalized local stress intensity factor as a function of the angle $\lambda$ .	142

## LIST OF TABLES

### Chapter 1

Table 1	Variations in Young's modulus and tensile strength of poly-Si.	6
---------	--	---

### Chapter 3

Table 1	Properties of poly-Si thin film.	18
Table 2	Tensile strength of poly-Si thin film against the specimen size.	24
Table 3	Fitting results using the maximum likelihood method.	29

### Chapter 4

Table 1	Mechanical property data for polysilicon.	41
Table 2	Fracture toughness (MPa-m <sup>1/2</sup> ).	44

### Chapter 5

Table 1	Average beam displacement ( $\mu\text{m}$ ) at fracture for the materials tested. Uncertainties are one standard deviation of the measured displacement.	52
Table 2	Estimated maximum strain state in beams at failure (%).	52

### Chapter 7

Table 1	Critical energy release rate data.	67
Table 2	Fracture mechanics specimen dimensions. Specimen A is shown in Figure 7c. All dimensions in microns.	75
Table 3	Experimental polysilicon fracture data.	80

### Chapter 9

Table 1	Coefficient of variation of nominal plane strain Young's modulus $\bar{E}^n$ of various cubic materials versus number of grains; $c_{ij} \times 10^{-6}$ Pa shown.	101
Table 2	Comparison of predicted mean values of plane strain modulus $\bar{E}^n$ and Poisson's ratio $\nu^n$ with Voigt and Reuss bounds ( $n=1000$ ).	101

### Chapter 10

Table 1	Calculated crack tip parameters.	131
Table 2	Evaluation of the size effect for various levels of anisotropy.	142

## PREFACE

This research was conducted under Air Force Contract F33615-94-C-5804, "Contributive Research and Development", Task #140, sponsored by Air Force Research Laboratory, Materials Directorate, Non-metallic Materials Division, Structural Materials Branch at Wright-Patterson AFB, Ohio. The Air Force Program Manager was Mr. Philip Mykytiuk. The Air Force Technical Manager was Dr. Nicholas Pagano. The principal investigator was Dr. Roberto Ballarini. The Systran Corporation Program Manager was Dr. V. Nagarajan.

## SUMMARY

### PROJECT OBJECTIVES, METHODOLOGY, AND OUTLINE OF THE REPORT

#### OBJECTIVES AND METHODOLOGY

This technical report serves as the deliverable for a project that involves (1) a review of recent studies of the mechanical behavior of polycrystalline silicon used to fabricate microelectromechanical systems (MEMS) devices, (2) the development of original theoretical models and experimental techniques that will lead to improved understanding of such behavior, and (3) suggestions for future research. It is hoped that this report will serve as a document that will introduce those interested in the subject to recent developments in the field.

The scientist's original proposal defined the following objectives:

1. Provide an assessment of the state of the art of theoretical and experimental mechanics in the field of MEMS technology.
2. Develop analytical models to treat outstanding issues, such as, the appropriate scale for fracture mechanics analyses.
3. Develop fracture mechanics specimens with characteristic dimensions of the same order of magnitude as those of MEMS devices.
4. Define the research needs to predict the life and strength of MEMS devices.
5. Report on any novel MEMS applications that are important to the Air Force, such as, sensors for the detection of small cracks under fatigue or regions degraded by corrosive agents.

The methodology was comprised of the following tasks:

1. Site visits to university and industrial laboratories involved in MEMS engineering and science.
2. Literature review and critique of theoretical and experimental studies of the mechanical behavior of materials used to fabricate MEMS devices.
3. Search of evidence of failures due to residual stresses, fatigue, delamination, etc..
4. Formulation of analytical models.
5. Development of fracture mechanics specimens.
6. Identification of research needs based on Tasks 1-5.

Task 1 was accomplished through visits to the University of Michigan Center for Integrated Sensors and Circuits, the University of California at Berkeley Sensor and Actuator Center, Microcosm, and Analog Devices. As a result of the discussions he had with researchers at these organizations, the scientist quickly learned the state-of-the-art of



MEMS technology, especially the issues related to the objectives of the project. Trip (oral) reports were provided to Dr. N. Pagano of Wright Patterson Air Force Base, and are not included in this report.

Task 2 was realized as follows. On the experimental side, the scientist decided early on to concentrate solely on studies of elastic properties, tensile strength, and fracture toughness of polycrystalline silicon, the most commonly used structural material for MEMS devices. Furthermore, the scientist decided to limit this review to work published after 1995. While it is clear that additional topics are important in MEMS (stiction, wear, etc.), the properties treated in this report are the most fundamental for engineering design. Concomitant to the literature review, the scientist and his coworkers continued the development of an electrostatically loaded fracture mechanics specimen whose characteristic lengths are comparable to those of typical MEMS devices. The motivation for the electrostatic loading, which eliminates the need of external loading devices (as are used in all other test methods for polysilicon described in this report), is the development of on-chip test structures that will allow in-situ measurement of strength/fracture/fatigue of actual devices. This on-chip philosophy was well received by the MEMS device developers that the scientist visited as part of Task 1.

It is important to note that the literature review in this report is not exhaustive. Rather it is comprised of a representative cross-section of the techniques available to measure the mechanical properties of polycrystalline silicon. Furthermore, most of the research groups that were chosen for review consider mechanical testing and theoretical modeling their "bread and butter", not simply a necessary burden that is part of the development and design of specific MEMS devices.

On the theoretical side, two issues have been addressed through literature review and model development. The first is the prediction of the scatter in the nominal elastic constants of polycrystalline films. This information is needed in applications that rely on the knowledge of stiffness and its uncertainty. The two models reviewed are stochastic, the first one developed by D. Mirfendereski and coworkers at University of California at Berkeley, the other by the scientist and coworkers at Case Western Reserve University.

The second theoretical issue involves quantification of the effects of heterogeneity and anisotropy on crack tip parameters in cracked polycrystalline films. This information provides insight into the appropriate scale for fracture mechanics analyses of MEMS devices. The two models reviewed estimate the stress intensity factors and energy release rate of a relatively long crack in a polycrystalline film, and provide useful information about cracks in components that contain a relatively large number of anisotropic grains. The first, developed by K. Abdel-Tawab and coworkers at University of Texas at Austin in their study of fracture of columnar sea-ice, relies on an approximate model for the interaction of the crystals with each other and with the crack tip. The second, developed by the scientist and coworkers during the course of this project, relies on a more accurate finite element method based Monte Carlo model. Both models predict that the crack driving forces are sensitive only to the details of the grains in the immediate vicinity of the crack tip. The study of cracks whose lengths are comparable to the grain size is one of the outstanding problems that will be discussed in Part 4 of this report, as part of Task 4. The information is essential if one is to perform fracture mechanics analyses of very (in-plane) thin components of MEMS devices, such as connecting beams in resonators.

Evidence of field failures due to residual stress, fatigue, delamination cracking, etc. was sought, but very little was found. This is not surprising; the technology is new, the number of applications of MEMS is still relatively small, mechanical reliability data is not available, and the scientist suspects there is inertia to admit the possibility or experience of failures. However, one laboratory failure under service conditions was found and is reported, and suggests that long term reliability of MEMS devices necessitates a basic understanding of the fracture mechanics of polycrystalline silicon. Additional fracture mechanics phenomena, including interfacial cracking, will eventually have to be addressed, since MEMS structures comprised of layered films are being developed. An example described briefly in Part 4 is SiC coated polycrystalline silicon developed by Mehregany and coworkers at Case Western Reserve University (*K.N. Vinod, C.A. Zorman, A. Yasseen and M. Mehregany, "Fabrication of low defect density 3C-SiC on SiO<sub>2</sub> structures using wafer bonding techniques," Journal of Electronic Materials, in press*).

MEMS applications important to the Air Force are not described in this report.

## OUTLINE

The report is divided into four parts, each consisting of chapters. Part 1 (Chapters 1 and 2) serves as an introduction. Chapter 1 summarizes data for elastic modulus, strength, and fracture toughness of polycrystalline silicon films. The variability of the data clearly illustrates the need for robust measurement techniques and data bases for mechanical properties as functions of processing procedures, specimen size, etc.. Chapter 2 presents a device that failed in the laboratory as a result of static fatigue (or stress corrosion) under the action of applied loads and a humid environment. This example suggests the need to study the fracture mechanics of polycrystalline silicon, including fracture toughness and subcritical crack growth.

The experimental work performed by six research groups is summarized in Part 2, which contains Chapters 3-8. In this part of the report the scientist has essentially rewritten the papers published by the following research groups; T. Tsuchiya and coworkers at Toyota Central Research and Development Laboratories, W.N. Sharpe and coworkers at Johns Hopkins University, G. Johnson and coworkers at the Berkeley Sensor and Actuator Center, S. Brown and coworkers at Exponent (formerly Failure Analysis Associates), the scientist and coworkers at Case Western Reserve University, and M.T.A. Saif and coworkers at University of Illinois at Urbana and Cornell University. The work of this last group is associated with single crystal silicon. It is summarized in this report because it presents an on-chip strength test that does not rely on the assumption of an elastic modulus. The scientist chose this method of writing Part 2 in an effort to eliminate the interested readers' need to search for the original papers (in the MEMS community many papers appear in conference proceedings, which as a general rule are more difficult to find in libraries).

The theoretical models are presented in Part 3, which is comprised of Chapters 9 and 10. These chapters summarize, respectively, the aforementioned predictive models for elastic constants and crack driving forces.

Part 4 provides conclusions and suggestions for future research.

In this report references are provided within the text in *bold italic* fonts. This nonstandard format eliminates the need to turn to a reference section while reading the text. The following abbreviations are used throughout the text.

B-doping	boron doping
BSAC	Berkeley Sensor and Actuator Center
COD	crack opening displacement
HF	hydrofluoric acid
JHU	Johns Hopkins University
LPCVD	low pressure chemical vapor deposition
LTO	low temperature oxidation
MCNC	Microelectronics Center of North Carolina
MEMS	microelectromechanical systems
MUMPs	Multi-User MEMS Process
NSG	non-doped silicate glass
P-doping	phosphorous doping
poly-Si	polycrystalline silicon
PSG	phosphosilicate glass
RIE	reactive ion etching
SEM	scanning electron microscope
SNL	Sandia National Laboratories
TEM	transmission electron microscope
TCRDL	Toyota Central Research and Development Laboratories
UCB	University of California at Berkeley
UM	University of Michigan
UI	University of Illinois
WPAFB	Wright Patterson Air Force Base

## ACKNOWLEDGEMENTS

The scientist acknowledges the following individuals for fruitful discussions, and for providing original electronic files of original figures that allowed excellent reproduction of the master manuscript; Roger T. Howe, Chris Keller, George C. Johnson and Peter T. Jones (BSAC), Toshiyuki Tsuchiya (TCRDL), William N. Sharpe, Jr. (JHU), Stuart Brown (Exponent), Kensall D. Wise, Liwei Lin, Carlos H. Mastrangelo and Clark T.-C. Nguyen (UM), Stephen Bart (Microcosm), Nicholas R. Swart (Analog Devices), M. Taher A. Saif (UI), Maarten P. de Boer (SNL), and Nick Pagano (WPAFB).

## CHAPTER 1

### VARIATIONS IN MECHANICAL PROPERTIES OF POLYSILICON

Until recently the MEMS community has focused on the development of fabrication processes and clever devices. Based on his discussions with the individuals acknowledged in the previous section, the scientist concluded that in order for MEMS technology to reach its full potential, durability and reliability issues of designed products need to be addressed. Therefore basic understanding of the mechanical behavior of the materials used to make devices is paramount, especially for devices that are expected to survive overloads, a large number of cycles of load, or harsh environments. As mentioned previously, in this report attention is limited to poly-Si. The most basic static structural design of a poly-Si device requires the knowledge of Young's modulus (and perhaps Poisson's ratio) and tensile strength. The endurance limit, as obtained from an S-N curve, is needed to ensure that the structure will not fracture under cyclic loads. Flaw-tolerant designs involve fracture toughness, and long term reliability necessitates quantification of subcritical crack growth rates (as discussed in Chapter 2).

While efforts at measuring Young's modulus and tensile strength of poly-Si for MEMS devices have been made over the last decade, the data base is sparse, and properties vary significantly as a result of differences in specimen configuration and size, property measurement techniques, and device fabrication procedures. Fracture toughness, stress corrosion behavior, and fatigue life data is even more scarce. The variations in stiffness and strength are clearly illustrated through Table 1, which presents in (less detail) the data reported by W.N. Sharpe (*W.N. Sharpe, Jr., B. Yuan and R.L. Edwards, "Variations in mechanical properties of polysilicon", Proceedings of 43rd International Symposium of the Instrumentation Society of America, Orlando, FL, pp. 179-188, 1997*; *W.N. Sharpe, Jr., B. Yuan, R.L. Edwards and R. Vaidyanathan, "Measurements of Young's modulus, Poisson's ratio, and Tensile Strength of Polysilicon", Proceedings of the Tenth IEEE International Workshop on Microelectromechanical Systems, Nagoya, Japan pp. 424-429, 1997*) for Young's modulus and tensile strength of polycrystalline silicon, measured since 1989. The last two entries in this table were made by the scientist.

**Table 1- Variations in Young's modulus and tensile strength of poly-Si.**

Reference	Modulus (GPa)	Strength (GPa)
Tabata [S1]	160	-
Tai [S2]	123	-
Walker [S3]	190	-
Koskinen [S4]	164-176	2.69-3.37
Maier-Schneider [S5]	151-162	
Michalicek [S6]	163	
Biebl [S7]		2.11-2.84
Biebl [S8]	130-168	
Biebl [S9]	170	
Read [S10]	140	0.7
Kahn [S11]	150	
Gupta [S12]	142-147	
Jones [S13]		1.9
Tsuchiya [S14]	167	2.0-2.7
Sharpe [S15]	163-173	1.14-1.27
Marxer [S16]		3.89
Kahn [S17]		4.0-4.9

The above referenced paper provides a much more detailed description of (1) the various types and number of tests used to derive the data, (2) material processing procedures (type of doping, annealing temperature, etc.), (3) standard deviations of the strength and stiffness, and (4) measurement error estimates. As presented, this table simply illustrates the relatively large variations in the most fundamental mechanical properties; Young's modulus varies from 120-190 GPa, and the tensile strength varies from 0.7-4.9 GPa (the smaller values correspond to direct tension, while the large values are characteristic of flexure). These variations in turn provide a powerful argument for studying the mechanical behavior of poly-Si.

Indeed, Sharpe suggested and organized a round-robin program for measuring the stiffness and strength of poly-Si. This involved having (1) MCNC fabricate (during the same fabrication run) the test structures used by four different research groups, (2) each group make their measurements of Young's modulus and tensile strength, and (3) the

results presented to the MEMS community. The results of this very successful exercise are presented in Part 4.

The references quoted in the Table above are listed next for the reader that may want to read the original papers.

[S1] *O. K. Tabata, Kawahata, S. Sugiyama and I. Igarashi, "Mechanical property measurements of thin films using load-deflection of composite rectangular membranes,"* *Sensor and Actuators*, 20, pp. 135-141, 1989.

[S2] *Y.-C. Tai and R.S. Muller, "Measurement of Young's modulus on microfabricated structures using a surface profiler,"* *IEEE Micro Electro Mechanical Systems*, pp. 147-152, 1990.

[S3] *J.A. Walker, K.J. Gabriel and M. Mehregany, "Mechanical Integrity of Polysilicon Films Exposed to Hydrofluoric Acid Solutions,"* *Journal of Electronic Materials*, 20, pp. 665-670, 1991.

[S4] *J. Koskinen, E. Steinwall, R. Soave and H.H. Johnson, "Microtensile testing of free-standing polysilicon fibers of various grain sizes,"* *Journal of Micromechanics and Microengineering*, Vol. 25, pp. 13-17, 1993.

[S5] *D. Maier-Schneider, J. Maibach, E. Obermeir and D. Schneider, "Variations in Young's modulus and intrinsic stress of LPCVD-polysilicon due to high-temperature annealing,"* *Journal of Micromechanics and Microengineering*, Vol. 5, pp. 121-124, 1995.

[S6] *M.A. Michalicek, D.E. Sene and V.M Bright, "Advanced modeling of micromirror devices,"* *Proceedings of the International Conference on Integrated Micro/Nanotechnology for Space Applications, NASA & Aerospace Corp. Publication*, pp. 214-229, 1995.

[S7] *M. Biebl and H.V. Philipsborn, "Fracture strength of doped and undoped polysilicon,"* *Transducers '95-Euroensors IX, Proceedings of the 8<sup>th</sup> International Conference on Solid-State Sensors and Actuators, and Euroensors IX, Stockholm, Sweden, June '95*, pp. 72-75, 1995.

[S8] *M. Biebl, G. Brandl and R.T. Howe, "Young's modulus of in situ phosphorous-doped polysilicon,"* *Transducers '95-Euroensors IX, Proceedings of the 8<sup>th</sup> International Conference on Solid-State Sensors and Actuators, and Euroensors IX, Stockholm, Sweden, June '95*, pp. 80-83, 1995.

[S9] *M. Biebl, T. Scheiter, C. Hierold, H.V. Philipsborn and H. Klose, "Micromechanics compatible with an 0.8 mm CMOS process,"* *Sensors and Actuators A, Vol 46-47*, pp.593-597, 1995.

[S10] *D.T. Read and J.C. Marshall, "Measurements of fracture strength and Young's modulus of surface-micromachined polysilicon," Microlithography and Metrology in Micromachining II, SPIE Vol. 2880, Austin, Texas, pp. 56-63, 1996.*

[S11] *H. Kahn, S. Stemmer, K. Nandakumar, A.H. Heuer, R.L. Mullen, R. Ballarini and M.A. Huff, "Mechanical properties of relatively thick, surface micromachined polysilicon films," the Ninth Annual International Workshop on Micro Electro Mechanical Systems, San Diego, California, USA, pp. 343-353, 1996.*

[S12] *R.K. Gupta, P.M. Osterberg and S.D. Senturia, "Material properties measurements of micromechanical polysilicon beams," Microlithography and Metrology in Micromachining II, SPIE Vol. 2880, Austin, Texas, pp. 39-45, 1996.*

[S13] *P.T. Jones and G.C. Johnson, "Micromechanical structures for fracture testing of brittle thin films," Micro-Electro-Mechanical Systems, ASME DSC-Vol. 59, pp. 325-330, 1996.*

[S14] *T. Tsuchiya, O. Obata, J. Sakata and Y. Taga, "Specimen size effect on tensile strength of surface micromachined polycrystalline silicon thin films," Proceedings of the Tenth IEEE International Workshop on Microelectromechanical Systems, Nagoya, Japan, pp. 529-534, 1997.*

[S15] *W.N. Sharpe, Jr., B. Yuan, R. Vaidyanathan and R.L. Edwards, "Measurement of Young's modulus, Poisson's ratio, and tensile strength of polysilicon," Proceedings of the Tenth IEEE International Workshop on Microelectromechanical Systems, Nagoya, Japan, pp. 424-429, 1997.*

[S16] *C. Marxer, M.-A. Gretillat, N.F. de Rooij, R. Battig, O. Anthamatten, B. Valk and P. Vogel, "Reliability considerations for electrostatic polysilicon actuators using as an example the REMO component, Sensors and Actuators A 61, pp. 449-454, 1997.*

[S17] *H. Kahn, R. Ballarini, R.L. Mullen and A.H. Heuer, "Electrostatically actuated failure of microfabricated polysilicon fracture mechanics specimens," submitted for publication, 1998.*

## CHAPTER 2

### LABORATORY FAILURE OF A MEMS DEVICE

This chapter provides evidence that poly-Si is associated with static fatigue. This time dependent failure mechanism, defined as environmentally assisted subcritical crack growth under an applied stress, must therefore also be studied if long-term reliability of MEMS devices operating in an aggressive environment is to be achieved.

Figure 1 shows a fractured REMO (a light modulator) component developed in Switzerland by the Institute of Microtechnology, University of Neuchâtel, and Ascom (a telecommunications company) (*C. Marxer, M.-A. Gretillat, N.F. de Rooij, R. Battig, O. Anthamatten, B. Valk and P. Vogel, "Reliability considerations for electrostatic polysilicon actuators using as an example the REMO component, Sensors and Actuators A 61, pp. 449-454, 1997; C.R. Marxer, "Silicon micromechanics for applications in fiber optic communication," Doctor of Science Dissertation, University of Neuchâtel, 1997).*

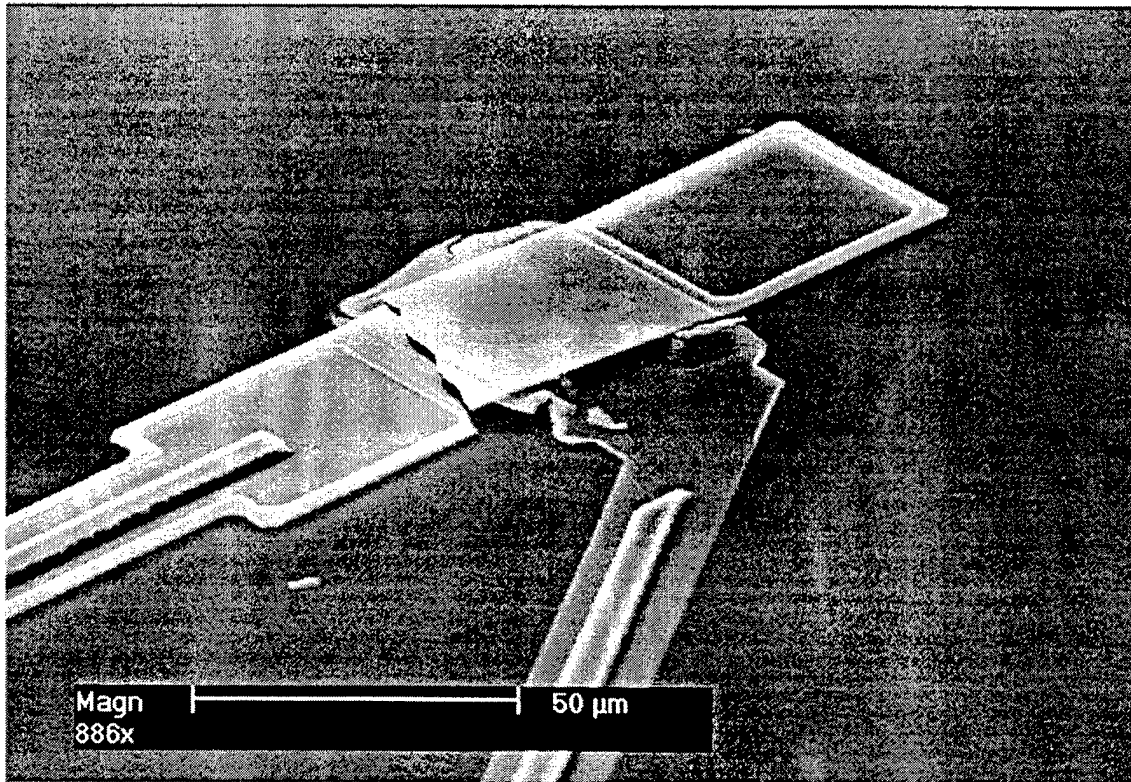


**Figure 1- A MEMS device that fractured under the combination of cyclic mechanical stress, high electric field, and humid air (Reference provided in text).**



This device is an optical transceiver system with a minimum of components, achieved by integrating a photodiode on the modulator chip. The poly-Si actuator includes a freestanding membrane with a nominal thickness of 464 nm, separated from the underlying electrode by an air gap of 1.6  $\mu\text{m}$ . In order for the device to perform its function, the membrane must deform 300 nm under the action of electrostatic forces. The electric field associated with this displacement is as high as 60 V  $\mu\text{m}^{-1}$ .

The authors performed a standard reliability analysis of the device, which consisted of the following steps.

1. A finite element analysis of the device was performed, yielding a maximum stress equal to 0.13 GPa.
2. The average and standard deviation of the tensile strength, evaluated experimentally using 200  $\mu\text{m}$  long and 2.8  $\mu\text{m}$  wide beams, were 3.89 GPa and 0.53 GPa, respectively. The data was fitted to the Weibull reliability function  $R(\sigma) = \exp[-(\sigma/\sigma_0)^m]$ , where  $\sigma$  is the applied stress. This produced a Weibull modulus  $m=7.5$  and  $\sigma_0 = 4.15\text{GPa}$ .
3. Using these results, they calculated a practically zero probability of failure for the maximum stress of 0.13 GPa.

The predictions of the analysis were confirmed experimentally. In dry air, no failure was observed. However, the rupture shown in Figure 1 was achieved in one week's time through the application of a field of 50 V  $\mu\text{m}^{-1}$  (corresponding to a stress of 100 MPa) and 80% humidity. The cyclic mechanical loads were produced by superimposing a 30 V peak-to-peak AC square signal of 500 kHz on a DC bias. Two failure mechanisms are observed; rupture of the free-standing membrane, and delamination of the fixed poly-Si electrode.

This is not a surprising result; Connally and Brown (*J.A. Connally and S.B. Brown, "Slow crack growth in single-crystal silicon," Science, Vol. 256, pp. 1537-1539, 1992*) demonstrated that slow crack growth can occur in single crystal silicon.

This work clearly illustrates the need for a basic understanding of environmentally assisted subcritical crack growth in poly-Si MEMS devices. As will be shown in Chapter 7, preliminary data on tension-compression fatigue loading of poly-Si in dry air suggests that subcritical crack growth can also occur with very little (and perhaps no) humidity.

# **PART I**

## **REVIEW OF EXPERIMENTAL WORK**

**CHAPTER 3 TOYOTA CENTRAL RESEARCH AND DEVELOPMENT  
LABORATORIES**

**CHAPTER 4 JOHNS HOPKINS UNIVERSITY**

**CHAPTER 5 BERKELEY SENSOR AND ACTUATOR CENTER**

**CHAPTER 6 EXPONENT**

**CHAPTER 7 CASE WESTERN RESERVE UNIVERSITY**

**CHAPTER 8 CORNELL UNIVERSITY AND UNIVERSITY OF ILLINOIS AT  
URBANA**

## CHAPTER 3

### TOYOTA CENTRAL RESEARCH AND DEVELOPMENT LABORATORIES

#### 1. INTRODUCTION

This chapter, which summarizes the work conducted at Toyota Central Research and Development Laboratories (Nagakute Aichi 480-11 Japan) by Toshiyuki Tsuchiya and co-workers, is based on the following three references.

- [1] *T. Tsuchiya, O. Tabata, J. Sakata, and Y. Taga, "Tensile testing of polycrystalline silicon thin films using electrostatic force grip," Transactions of Institute of Electrical Engineers of Japan, Vol. 116-E, No.10, pp. 441-446 (1996).*
- [2] *T. Tsuchiya, O. Tabata, J. Sakata, and Y. Taga, "Specimen size effect on tensile strength of surface micromachined polycrystalline silicon thin films," Journal of Microelectromechanical Systems, Vol.7, No.1, pp. 106-113 (1998).*
- [3] *T. Tsuchiya, J. Sakata, and Y. Taga, "Tensile strength and fracture toughness of surface micromachined polycrystalline silicon thin films prepared under various conditions," Materials Research Society Proceedings, Vol. 505 (in press).*

This group developed a testing procedure for measuring the tensile strength of poly-Si thin films through direct tension. They subsequently introduced a smooth edge notch in their specimen to measure the fracture toughness (actually the bending strength in the vicinity of a stress concentrator, since their notch is of finite radius). As mentioned by the authors, the dimensions of the specimen are comparable to those of connecting beams in typical MEMS devices (surface micromachined resonators, for example); thus the experimentally derived data is directly applicable to design and reliability of MEMS devices.

Reference [1] describes the experimental procedure, as well as preliminary results on the effects of specimen length on the tensile strength of undoped films. The results of a more detailed and complete study of size effects and doping on the tensile strength are presented in Reference [2]; the experimental data is presented through Weibull plots and Weibull parameters, with separate normalizations by volume, surface area, and side surface area. The effects of grain size (which depends on annealing temperatures) on the tensile strength and fracture toughness are studied in Reference [3].

#### 2. GENERAL DESCRIPTION OF EXPERIMENTAL TECHNIQUE

Mechanical testing of thin films poses many challenges, including how to grip the specimen to a loading device. This group's ingenious design takes advantage of relatively weak electrostatic forces to grip a thin film ( $2\mu\text{m}$  thick) specimen to a probe, thus eliminating

the need for mechanical grips or adhesives. Moreover, because the silicon wafer that contains the specimen can be placed into and removed from the testing chamber without being touched, there is very little danger of damaging the specimen before testing. The work is truly seminal, as evidenced by the fact that at least one research group (JHU, whose work is summarized in the next chapter) has substituted their adhesive based gripping system with the electrostatic system.

Figure 1 is a schematic of the test set-up. One end of the specimen is fixed to a (silicon wafer) substrate. The other end, which is free-standing, is fixed to a probe by an electrostatic force. The probe is a conductive silicon wafer covered with an insulating film of silicon nitride ( $\text{Si}_3\text{N}_4$ ). Figure 2 shows how the tensile loading is applied to the specimen. A sufficiently high voltage is applied between the specimen (which has the same electrical potential as the substrate) and the probe. The charge on their surfaces generates an electrostatic force that fixes them to each other. As this voltage is maintained, the tensile load is introduced by moving the probe with a piezoelectric actuator. One nice feature of this gripping device is the stable release procedure subsequent to fracture. By applying the opposite pole voltage between the probe and the substrate, the charge remaining on the specimen generates a repulsive force that releases it from the probe, and an attractive force that fixes it to the substrate. The unattractive feature of the loading device is that the applied force, as seen in Figure 2, is eccentric with respect to the neutral axis of the specimen. Therefore the specimen develops bending stresses. These have not been calculated nor considered in the data reduction.

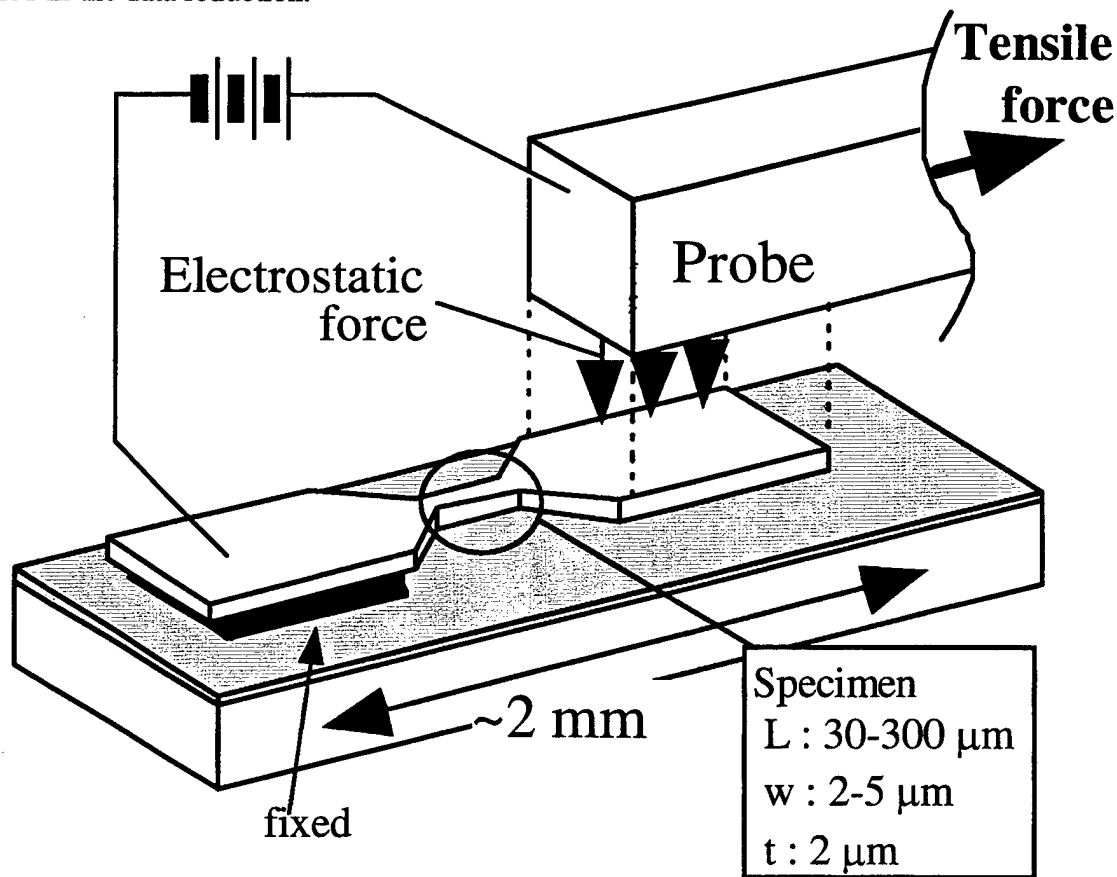


**Figure 1- Schematic drawing of tensile testing using an electrostatic force gripping system (Reference [2]).**

Figure 3 shows the geometry and nominal dimensions of the uniform tension and fracture toughness specimens. It is important to note that MEMS processing procedures can result in significant differences between design and as fabricated dimensions. In the current design, the design values of gage length  $L$  and width  $w$  vary, respectively, from 30-300 $\mu\text{m}$  and 2-5 $\mu\text{m}$ . As discussed subsequently, this allows the strength and toughness to be measured as functions of specimen size. The notch depth  $c$ , which is targeted for 1 $\mu\text{m}$  or 2 $\mu\text{m}$ , was measured as 0.81 $\mu\text{m}$  or 1.87 $\mu\text{m}$ . The notch tip radius was reported in Reference [3] as 0.23  $\mu\text{m}$ . A private communication with T. Tsuchiya puts this value at 0.6  $\mu\text{m}$ , and finite element derived stress concentration factors of 5.8 for  $w=2$ ,  $c=1$ ,  $a=2$ , and 8.0 for  $w=5$ ,  $c=2$ ,  $a=4$ .

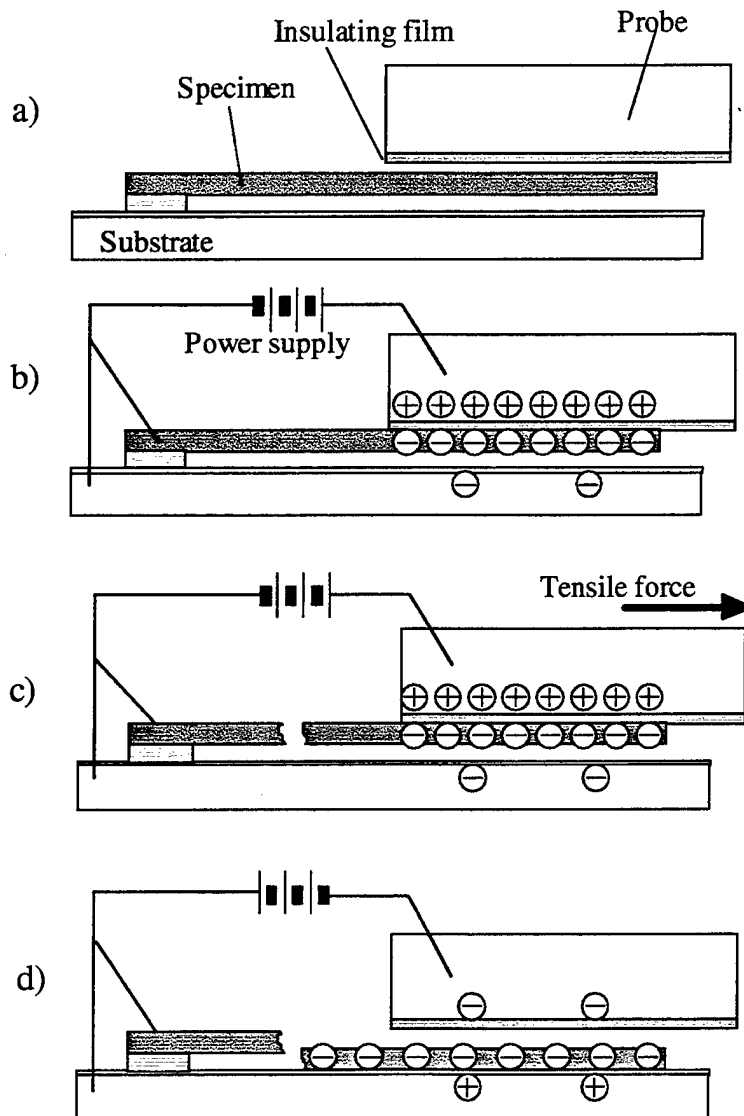
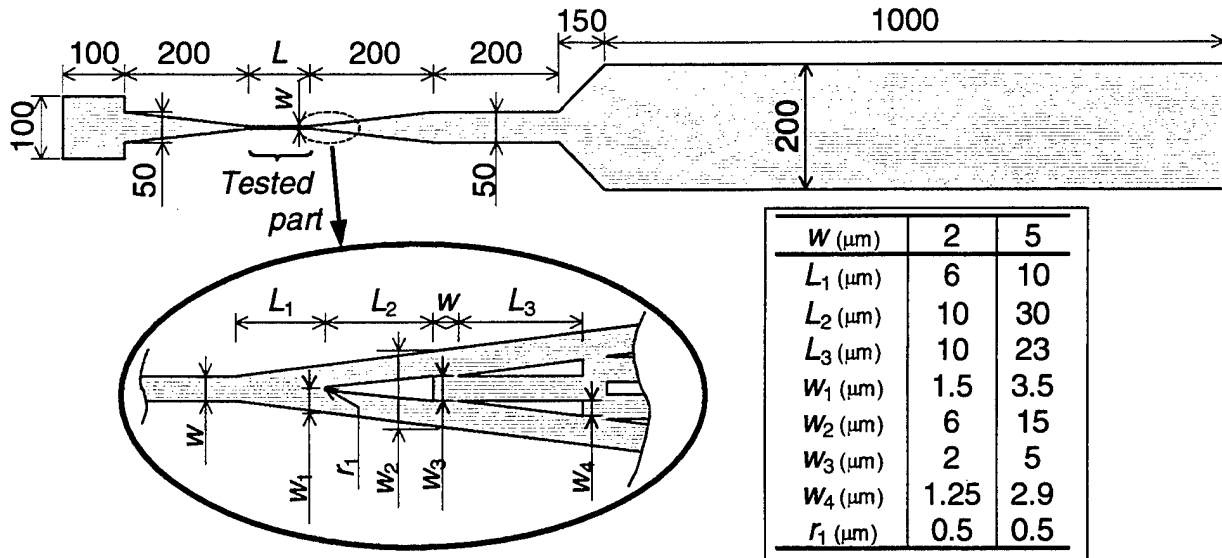
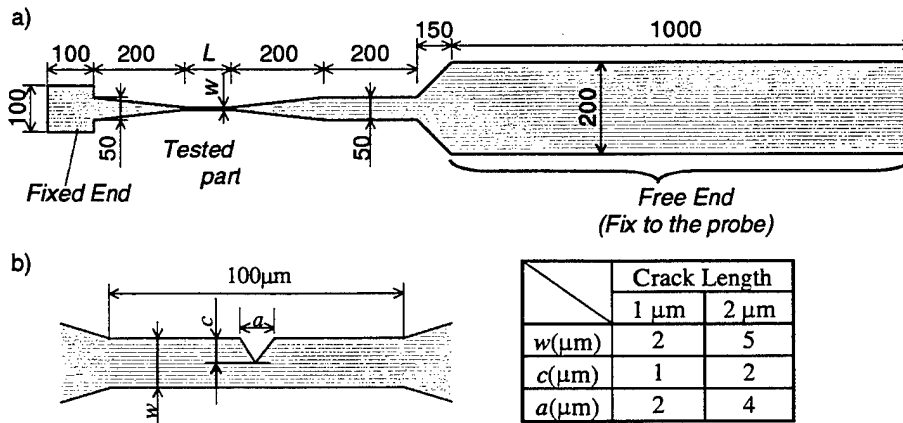


Figure 2- Tensile test procedure using electrostatic force (Reference [2]).



(a)



(b)

Figure 3- Thin film specimen for (a) uniform tension (Reference [2]), (b) fracture toughness (Reference [3]).

### 3. CONCEPTUAL DESIGN OF GRIPPING SYSTEM

To better understand the types and magnitudes of forces that make this experiment work (and the one described in Chapter 4), it is instructive to review the calculations involved in its conceptual design. The gripping force  $F_v$  is calculated as the electrostatic force acting perpendicularly to two parallel electrodes

$$F_v = \frac{\epsilon_0 S}{2d^2} V^2 \quad (1)$$

where  $S$  is the area of the free end of the specimen,  $d$  is the gap between the probe and the free end,  $V$  is the applied voltage, and  $\epsilon_0 = 8.854 \times 10^{-12} \text{ F/m}$  is the permittivity constant (of air in this case). In order for the specimen to stick to the probe, its weight should be less than  $F_v$ . This provides

$$\frac{\epsilon_0 S}{2d^2} V^2 - mg = \frac{\epsilon_0 S}{2d^2} V^2 - St\rho g > 0 \quad (2)$$

where  $g$  is the acceleration due to gravity, and  $m$ ,  $t$  and  $\rho$  are the mass, thickness, and density of the specimen, respectively. The applied voltage associated with electrical breakdown of the insulating film (several MV/cm) is 100V. For this voltage a several micron thick polysilicon film ( $\rho = 2.33 \times 10^3 \text{ kg/m}^3$ ) will stick at a gap  $d=1\text{mm}$ .

In order for the specimen not to slip relative to the probe, a force parallel to the tensile force is required. This force is comprised of a horizontal electrostatic force  $F_h$  and a friction force  $F_f$ , given by

$$F_h = -\frac{\epsilon_0 \epsilon_r w_g}{2d_1} V^2 \quad (3)$$

$$F_f = \mu F_v \quad (4)$$

where  $w_g$  is the width of the free end, and  $d_1$  and  $\epsilon_r$  are, respectively, the gap and dielectric constant between electrodes. When the specimen is fixed,  $d$  is equal to the thickness of the  $\text{Si}_3\text{N}_4$  insulating film ( $d=0.2 \mu\text{m}$  and  $\epsilon_r=8$ ). The resultant of these two forces must be greater than the fracture tensile force  $F_t$ , which is given in terms of the tensile strength  $\sigma_f$ , thickness  $t$ , and width  $w$ , as  $\sigma_f wt$ . The following sensitivity analysis shows that the friction force is much larger than the horizontal electrostatic force. Assume that the coefficient of friction  $\mu = 0.3$ . Since the tensile strength is on the order of 2-5GPa, the largest value of  $F_t$  is about 0.1N. Assuming, for the sake of argument, that the free end of the specimen is square,  $S = w_g^2$ , for 100V the necessary dimensions of the electrode are  $200\mu\text{m} \times 200\mu\text{m}$ . As a result,

$F_f$  is three orders of magnitude larger than  $F_h$ .

#### 4. SPECIMEN FABRICATION

The specimens described in References [1]-[3] were fabricated using standard micromachining technology. They are poly-Si films crystallized from an amorphous film. The authors favor crystallized polycrystalline silicon films because they are associated with a tensile residual stress, making them suitable for micromachined devices, and because their grain size can be controlled by the annealing temperature. Crystallization occurs above 600°C, the grain size decreasing with increasing annealing temperature. In Reference [1], the annealing temperature was 1000°C. In Reference [3], the effects of annealing temperature and associated grain size were investigated by testing films that were amorphous, or annealed at 600°C, 700°C, or 1000°C; in this paper the effects of additional annealing at 1000°C were also investigated. The effects of P-doping were studied in Reference [2].

The specimen is fabricated using the surface micro-machining process shown in Figure 4. The following key steps were reported in Reference [1].

1. A LPCVD amorphous silicon film is deposited at 520°C on the substrate, which is comprised of a 0.2 $\mu\text{m}$  thick LPCVD Si<sub>3</sub>N<sub>4</sub> insulating film and a 2 $\mu\text{m}$  plasma CVD NSG sacrificial film.
2. The amorphous film is crystallized by annealing in nitrogen at 1000°C.
3. In Reference [2] P-doping of the poly-Si film was performed using POCl<sub>3</sub> at 1000°C. The grain size of the poly-Si film is 0.3 $\mu\text{m}$ , irrespective of the doping.
4. The film is patterned into the shape of the specimen by photolithography and RIE. An aluminum pad electrode is fabricated on the fixed end of the specimen. The free end of the specimen has many etching holes which shorten the time needed for sacrificial etching time.
5. The sacrificial layer is removed by wet etching with HF.
6. The specimen is rinsed with distilled water, dipped with hot p-dichlorobenzene, and then dried. This last step prevents the specimen from sticking to the substrate.

Figure 5 shows a scanning electron micrograph of three typical specimens. The properties of the non-doped and P-doped poly-Si films, as reported in Reference [2], are shown in Table 1. The internal stress and the Young's modulus were measured on a rectangular membrane structure using the pressure-deflection technique (*O. Obata, K. Kawahara, S. Sugiyama, and I. Igarashi, "Mechanical property measurement of thin films using load-deflection of composite rectangular membranes," Sensors and Actuators, Vol. 20, pp. 135-141, 1989*).

In Reference [3] films with different average size grains were fabricated by annealing at 600°C, 700°C and 1000°C. Scanning electron microscope (SEM) micrographs of the different microstructures produced by these temperatures are shown in Figure 6; the 600°C and 1000°C annealed films are comprised of spherical grains of approximate size 2 $\mu\text{m}$  and 0.3 $\mu\text{m}$ , respectively, while the 700°C annealed film contains oval grains of about 0.7 $\mu\text{m}$  size. As discussed previously, some of the films went through an additional annealing at 1000°C, which had no effect on the grain size.



**Table 1 Properties of poly-Si thin film (Reference [2]).**

	non-doped	P-doped
Grain size	0.3 $\mu\text{m}$	0.3 $\mu\text{m}$
Thickness	1.8 $\mu\text{m}$	2.4 $\mu\text{m}$
Internal Stress	76MPa	-7.0MPa
Young's modulus	163GPa	167GPa

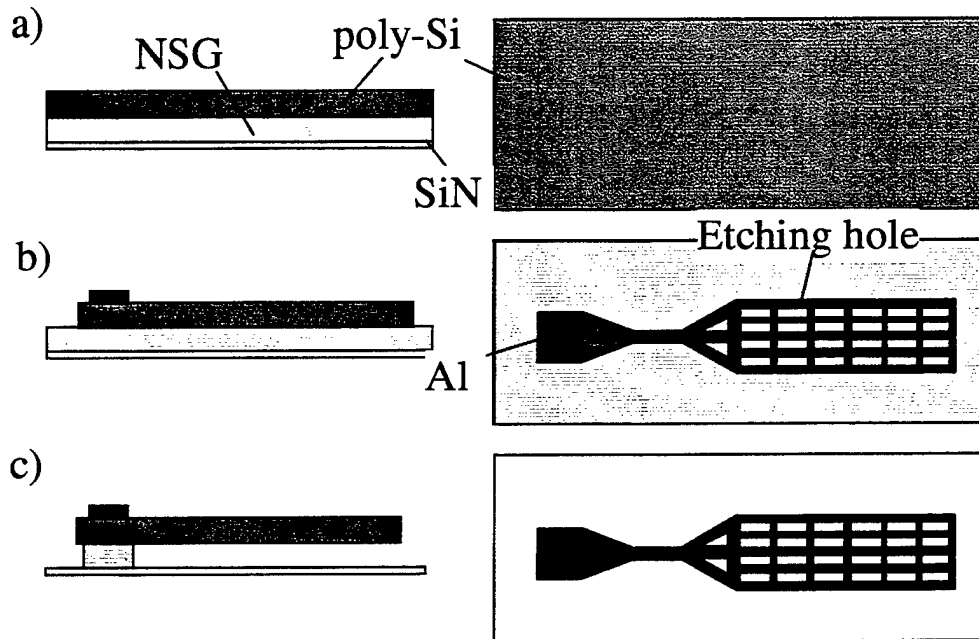


**Figure 4- Fabrication process (a) deposition of films, (b) patterning of poly-Si and Al films, (c) sacrificial etching to release poly-Si (Reference [2]).**

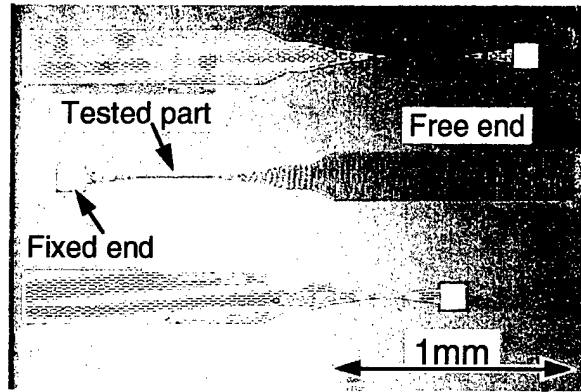
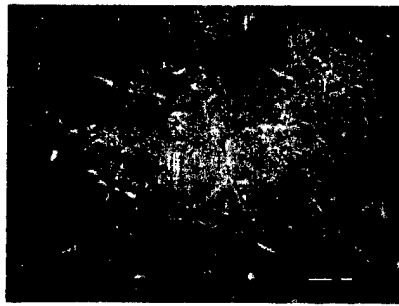
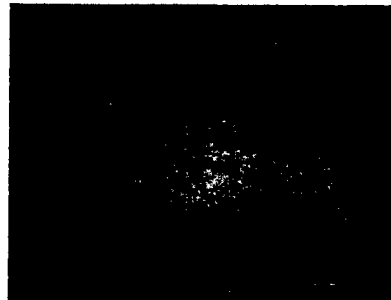


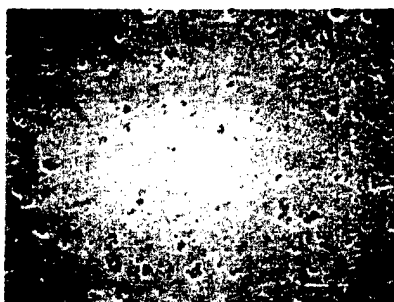
Figure 5- SEM micrograph of three typical specimens (Reference [1]).



(a)



(b)



(c)

Figure 6- SEM micrograph of poly-Si film crystallized at (a) 600°C, (b) 700°C, and (c) 1000°C (Reference [3]). Note the decrease in grain size with increasing temperature.

### 5. TESTING PROCEDURE

As shown schematically in Figure 7, the tension test is conducted (in a vacuum) inside an SEM chamber. This figure shows the locations of the piezoelectric actuator, the strain gauge that measures the force, and the strain gauge that measures the displacement. Figure 8 is an SEM micrograph of the probe gripping a specimen. This figure clearly shows the eccentric nature of the loading device, and the resulting bending of the specimen. The ratio of maximum bending stress to axial stress is  $6\epsilon/t$ , where  $\epsilon$  is the distance from the line of action of the force to the neutral surface of the specimen within the gauge section.

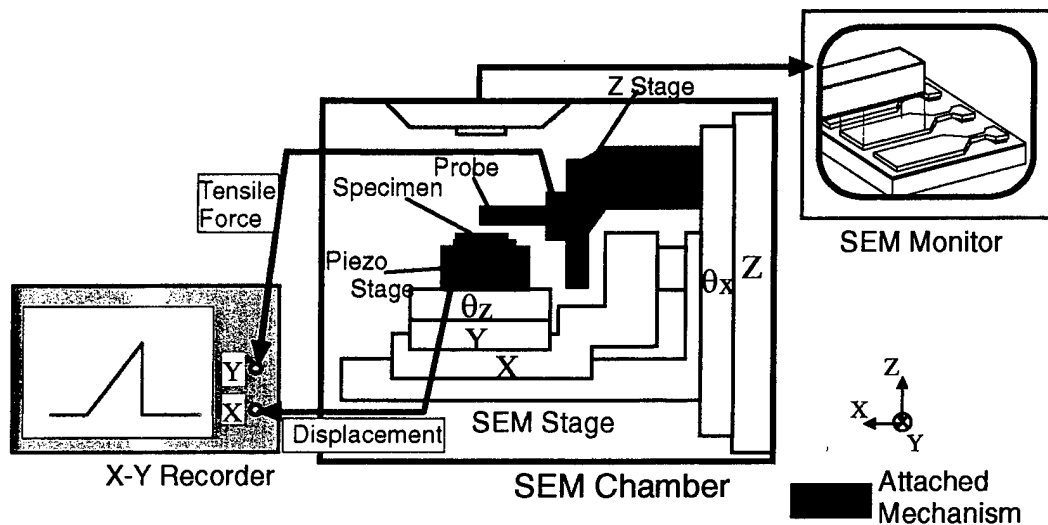


Figure 7- SEM chamber testing environment (Reference [3]).

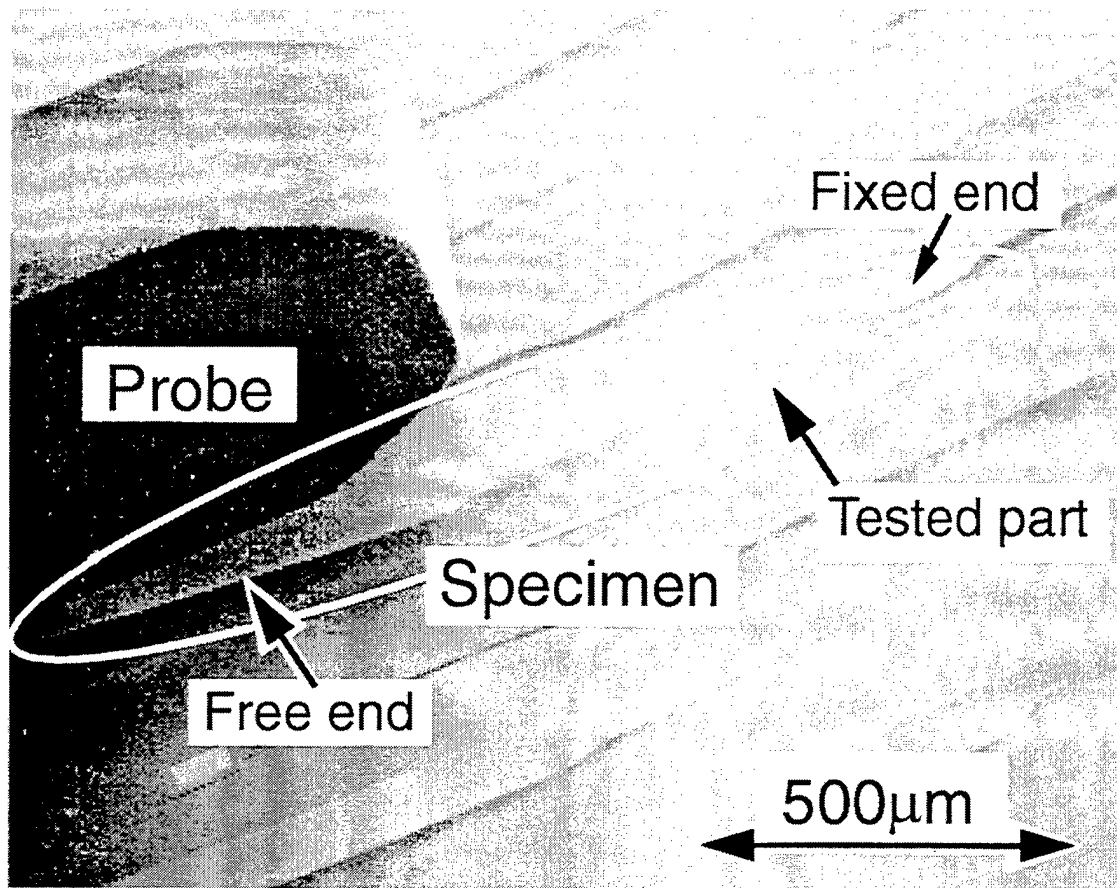


Figure 8- SEM micrograph of tensile testing (Reference [2]). Note that the specimen is subjected to eccentric loading, as evidenced by its bent shape.

## 6. RESULTS

This section is divided into three parts. The effects of specimen size and grain size on the tensile strength are presented first. This is followed by the effects of grain size on fracture toughness. The final section discusses fracture initiation site.

### Tensile strength

#### Effect of specimen size and doping

Fracture is always brittle, and initiates at random positions within the tested length. The tensile strength for various gage lengths, as reported in Reference [1], is presented in Figure 9. In this figure,  $n$  represents the number of specimens tested. As expected for this brittle material, the average strength decreases with increasing gage length. This size effect is studied in a more systematic fashion in Reference [2], as discussed next.

The mean strength, standard deviation, and Weibull modulus for the un-notched specimens, taken from Reference [2], are summarized in Table 2. The mean and the range of the tensile strength are shown in Figure 10.

Because the authors assumed that the strength data follows a Weibull distribution,

the following results for this extreme value distribution are stated for completeness. The probability of failure under an applied stress  $\sigma$  is given as

$$F = 1 - \exp\left\{-\frac{\sigma^m}{\alpha} V_E\right\} \quad (5)$$

where  $m$  is the Weibull modulus,  $V_E$  is the effective volume of the tested part, and  $\alpha$  is a constant. The mean tensile strength  $\mu$  and variance  $Var$  are given by

$$\mu = \left(\frac{\alpha}{V_E}\right)^{1/m} \Gamma\left(\frac{1+m}{m}\right) \quad (6)$$

$$Var = \left(\frac{\alpha}{V_E}\right)^{2/m} \left[ \Gamma\left(\frac{2+m}{m}\right) - \Gamma^2\left(\frac{1+m}{m}\right) \right] \quad (7)$$

where  $\Gamma(x)$  is the Gamma function. It follows that the mean strengths  $\mu_1$  and  $\mu_2$  of specimens with effective volumes  $V_{E1}$  and  $V_{E2}$  are related by

$$\frac{\mu_2}{\mu_1} = \left(\frac{V_{E1}}{V_{E2}}\right)^{1/m} \quad (8)$$

For a fixed  $\alpha$  and  $V_E$ , a plot of Equation (7) would show that as  $m$  decreases, the scatter increases.

The fracture probability functions from Reference [2] are plotted in Figures 11. These were fitted to the Weibull distribution function using a least square method, the resulting parameter  $m$  tabulated in Table 2. It is first noted that the fitted distributions do not fit the data very well at the tail ends; this is not surprising because many more data points are required to accurately fit such distributions.

The strengths of the un-doped specimens reported in Reference [1] are very close to those reported in Reference [2]; this gives confidence to the reproducibility of the results. It is observed that the mean strength of the P-doped films is slightly lower than of the un-doped films. However, the strength of the un-doped films exhibits, for the same size specimen, a larger scatter (Weibull modulus 5.3-6.9) than that of the P-doped films (Weibull modulus 8.7-12.6).

The most important result of this work is perhaps the implication that if poly-Si is to be used to its full potential (in terms of strength), processing techniques must be adjusted to mitigate the variability in strength. This is demonstrated clearly by considering the ratio of allowable stress  $\sigma^{all}$  to mean strength for a prescribed reliability. Assume for the sake of argument that the data is indeed Weibull. Combining Equations (5) and (6) this ratio becomes

$$\frac{\sigma^{all}}{\mu} = \frac{[-\ln(1-F)]^{1/m}}{\Gamma\left(\frac{1+m}{m}\right)} \quad (9)$$

If reliability considerations demand that only one part in a million fail ( $F = 10^{-6}$ ), then for  $m=5, 6.5$  and  $10$ , the allowable stress is only 6.8%, 12.8% and 26% of the mean strength. In other words, these levels of variability in strength require a very conservative design approach.

As discussed in the final section of this chapter, there is evidence that in these films, the fracture initiates at surface flaws formed by the sacrificial etching procedure. Therefore the most effective way of reducing scatter in strength is through improved processing procedures that mitigate the development of these stress concentrators.

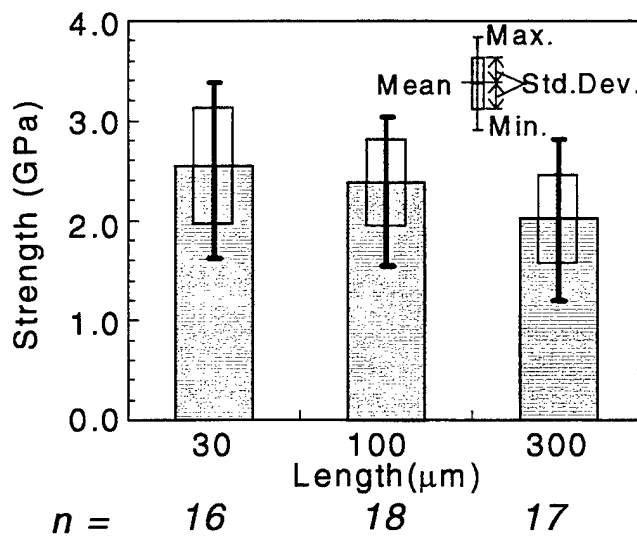
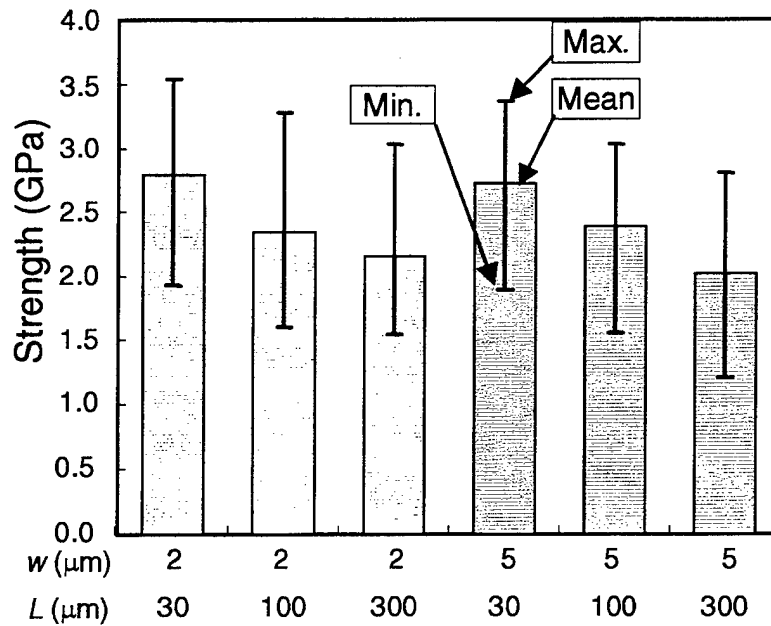


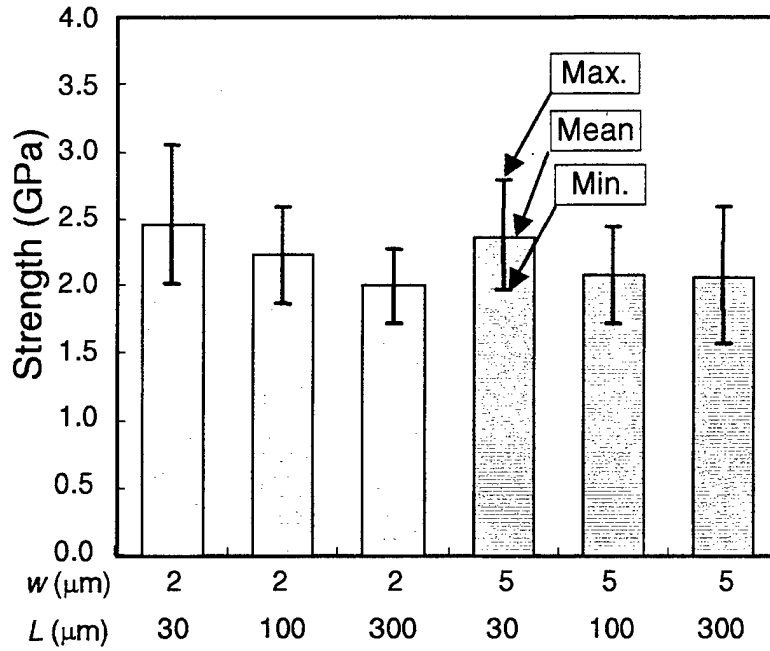
Figure 9- Tensile strength for different gage lengths (Reference [1])

**Table 2 Tensile strength of poly-Si thin film against the specimen size**  
(Reference [2]).

	non-doped						P-doped					
	2			5			2			5		
Width ( $\mu\text{m}$ )												
Length ( $\mu\text{m}$ )	30	100	300	30	100	300	30	100	300	30	100	300
Sample Number	11	14	17	13	18	17	11	12	11	13	12	15
Mean Strength (GPa)	2.8	2.3	2.2	2.7	2.4	2.0	2.5	2.2	2.0	2.4	2.1	2.1
Std. Dev. (GPa)	0.61	0.52	0.45	0.48	0.44	0.45	0.37	0.20	0.20	0.25	0.19	0.26
Weibull modulus	5.3	6.0	6.0	6.9	6.3	5.4	8.7	12.0	9.9	10.1	12.6	9.3



(a)



(b)

Figure 10- Tensile strength of poly-Si thin film; (a) un-doped film, (b) P-doped film (Reference [2]).



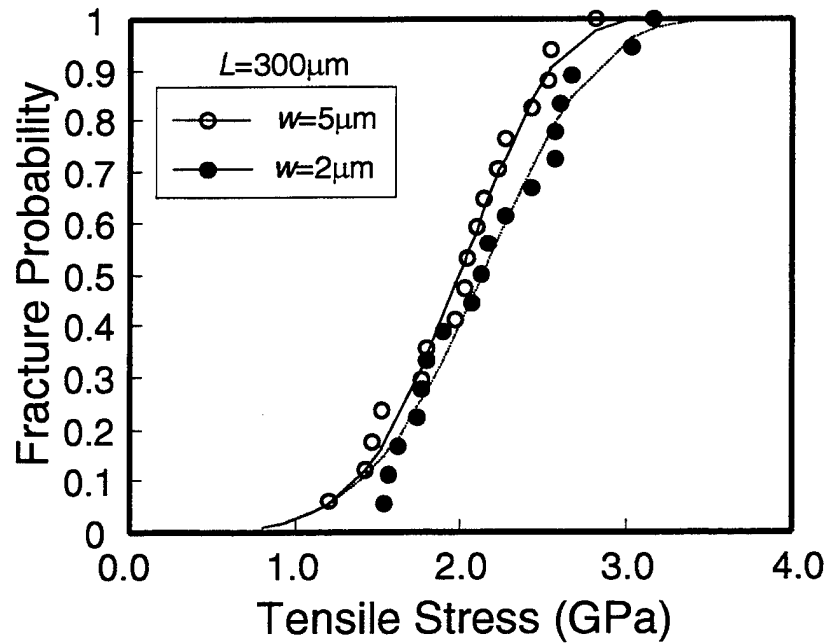
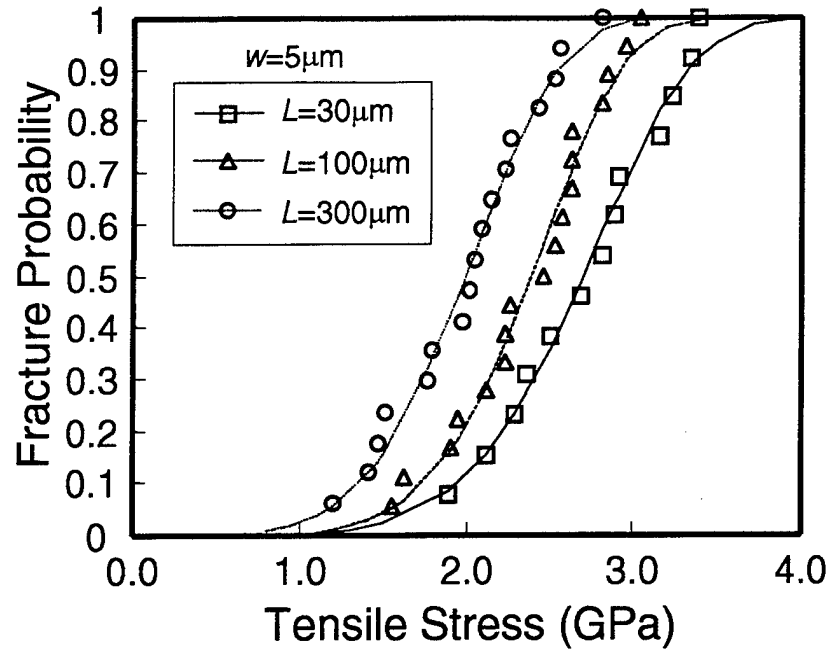
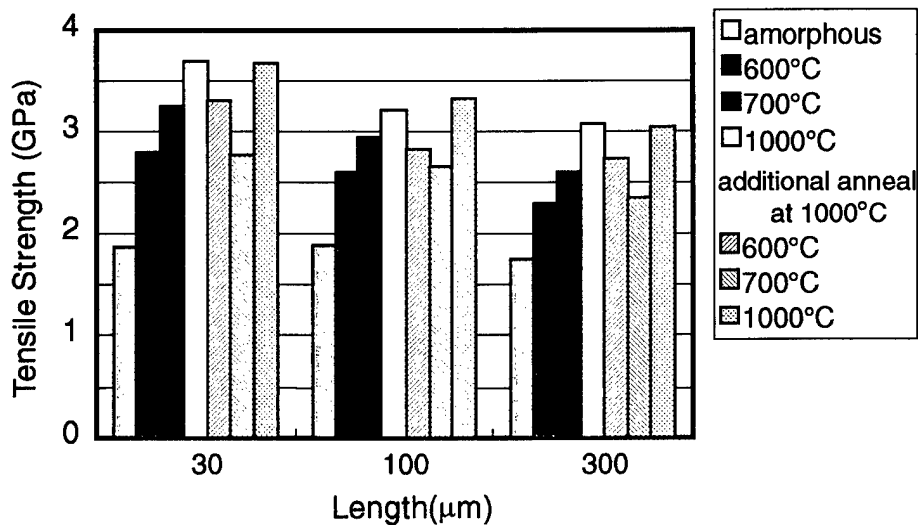


Figure 11- Measured fracture probability as a function of tensile stress. The curve is fitted to Weibull distribution function (Reference [2]).

## Effect of grain size

In Reference [3] the effects on tensile strength of the previously described different annealing conditions and their associated grain size were studied. The results are presented in Figure 12. It is observed that for all specimen sizes, amorphous films have the lowest average tensile strength, and that the strength increases with increasing annealing temperature (decreasing grain size). The authors attributed the lower strength in the amorphous films to the presence of 0.4% hydrogen. For the specimens that were subjected to additional annealing, there seems to be a mixed pattern; the additional annealing slightly strengthened the 600°C specimens, slightly weakened the 700°C specimens, and had no effect on the 1000°C specimens.



**Figure 12- Tensile strength of poly-Si films for various annealing conditions (and grain size (Reference [3])).**

## Fracture toughness

The notched beam shown in Figure 3(b) was used to measure the fracture toughness ( $K_{Ic}$ ). Assuming that the notch is a sharp crack of equal depth, available handbook formulas were used, together with the fracture load, to derive the nominal fracture toughness values in Figure 13. It is observed that these values range from 1.9 to 4.5 MPa-m<sup>1/2</sup>.

Because the notch tip has a radius comparable to other characteristic dimensions (the most important being the lengths of the notch and uncracked ligament), these results do not represent the true toughness of the material; this parameter requires propagation from an atomically sharp crack. The results can, at best, be used to determine the bending strength in the region of a stress concentrator (5.8 for  $w=2$ ,  $c=1$ ,  $a=2$ , and 8.0 for  $w=5$ ,  $c=2$ ,  $a=4$ ), or the critical J-integral for the given notch-tip radius. This method of presenting results obtained

using a finite radius notch is favored and recommended by the scientist and his coworkers, as discussed in Chapter 7.

In Reference [3] the authors also back calculate an initial flaw size for the tension specimens, and concluded that while the critical flaw sizes did not correlate well with grain size, they did correlate well with the surface pits produced by the etching procedure. While the conclusion may be correct, the procedure they used is questionable. The critical stress is proportional to the fracture toughness and the inverse of the square root of the critical flaw size (knowledge of two parameters provide the third). The authors used the critical stress from the tension test, the fracture toughness from the notch tension specimens, and determined the flaw size. This procedure is questionable because the notch tests, as discussed previously, do not provide the true toughness.

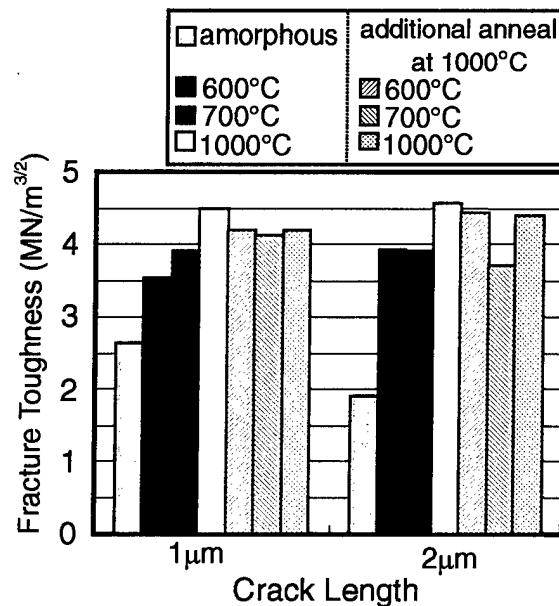


**Figure 13- Fracture toughness of poly-Si films for various annealing conditions (and grain size (Reference [3])).**

#### Determination of fracture initiation site

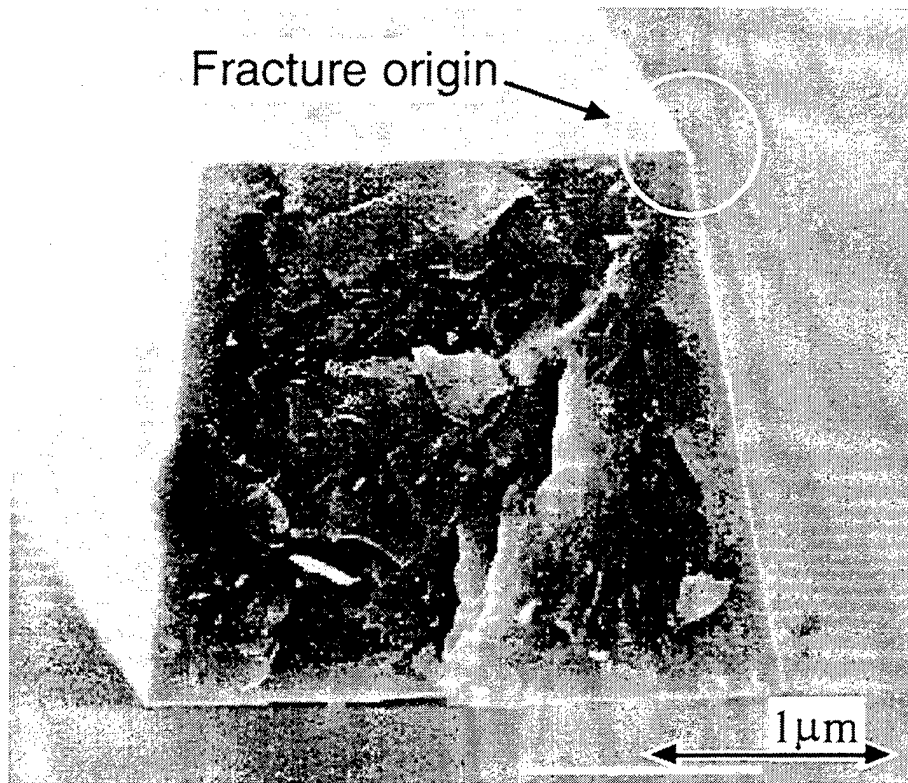
The ideal method of determining where fractures initiate is inspection of the fracture surfaces. Figure 14 taken from Reference [2], shows a typical fracture surface, and indicates that the fracture origin is on the surface of the specimen. According to the authors, this was typical of all observed fracture surfaces. Similar fracture surfaces were observed by the

scientist and coworkers, as described in Chapter 7.

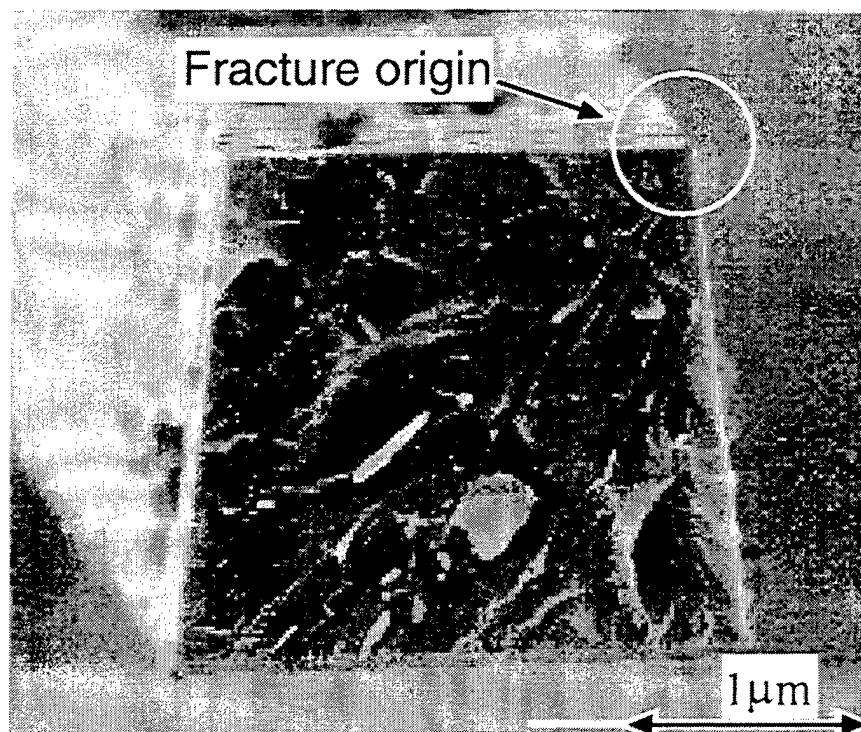
The authors also used an unconventional statistical method to determine whether the fracture initiated within the volume, on the total surface, or on the side surface. They used the maximum likelihood method to fit the data to the Weibull distribution function using these geometric parameters in Equation (5). The results are shown in Table 3 and Figure 15. Table 3 presents the Weibull moduli  $\hat{m}$ , the likelihood functions  $\hat{L}$ , and reliability coefficients  $R^2$  for each of these geometric parameters.  $R^2$ , calculated by EXCEL, is a normalized residual of the sum of the squared difference between the measured values and the fitted values. The functions with the length and the side surface area are associated with (very slightly and statistically insignificant) larger values of the likelihood function and reliability coefficients. The authors concluded that these slight differences suggest surface flaw driven fracture.

**Table 3 Fitting results using the maximum likelihood method  
(Reference [2]).**

	fitting parameter		length	width	all surface area	side surface area	volume
			$l$	$w$	$S$	$S_s$	$V$
non-doped	Weibull modulus	$\hat{m}$	6.3	5.0	6.5	6.3	6.6
	likelihood function	$\log \hat{L}$	-1927	-1943	-1927	-1927	-1930
	reliability coefficient	$R^2$	0.818	0.546	0.803	0.818	0.763
P-doped	Weibull modulus	$\hat{m}$	10.0	7.9	10.2	10.0	10.3
	likelihood function	$\log \hat{L}$	-1541	-1555	-1544	-1541	-1548
	reliability coefficient	$R^2$	0.790	0.523	0.775	0.790	0.732



a) non-doped film



b) P-doped film

Figure 14- Fracture surface of poly-Si thin film (Reference [2]).

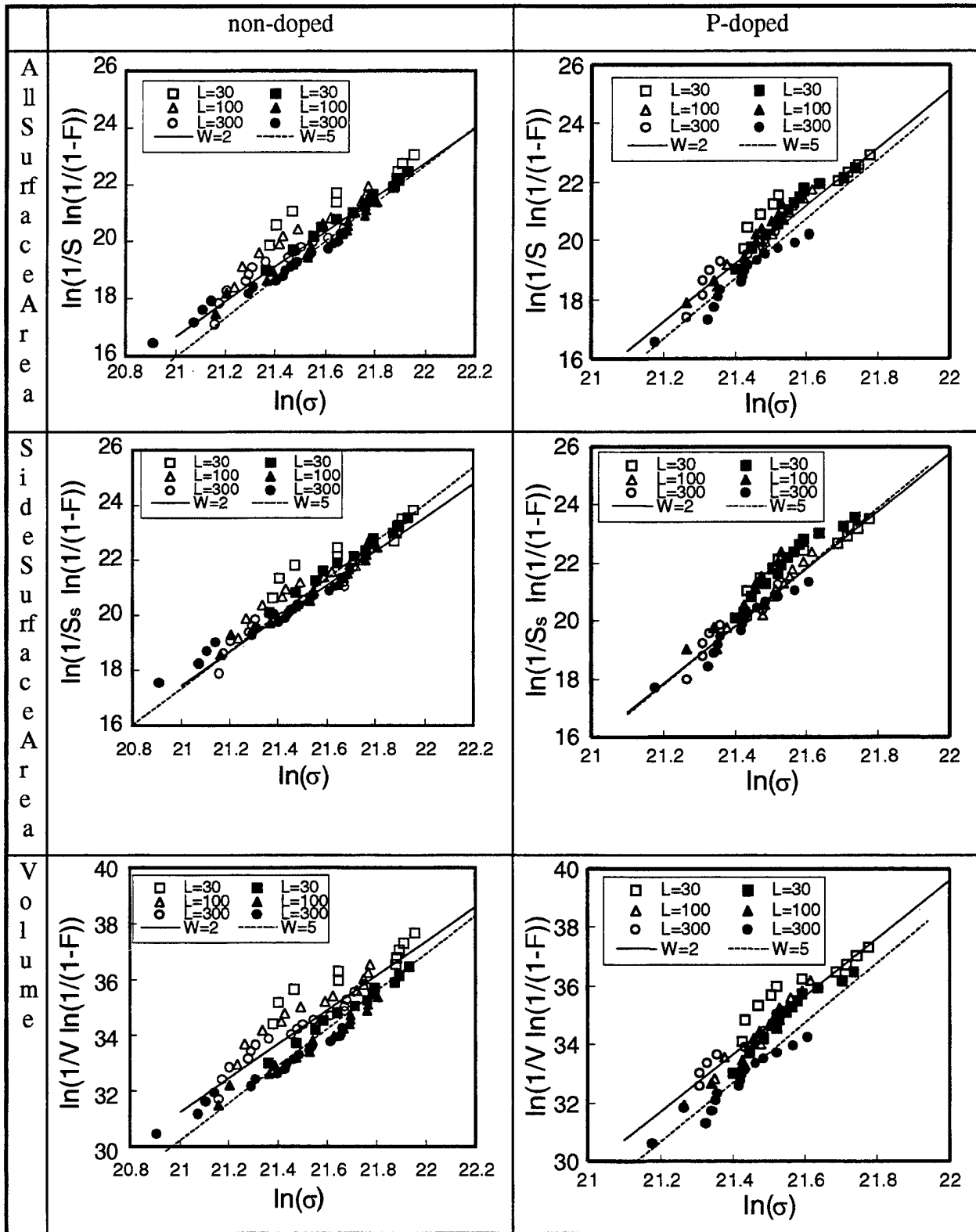


**Figure 15- Weibull plots normalized by the volume, the surface area, and side surface area (Reference [2]).**

## **7. CRITIQUE**

The electrostatic loading system developed by the research group at TCRDL is truly path-breaking; it offers an effective method for loading thin films with characteristic dimensions comparable to those of typical MEMS devices. The group has also started on the correct path as they use their system to (1) gain a better understanding of the effects of processing procedures on the mechanical properties of poly-Si, (2) reducing the data using standard statistical analyses, which together with stress analysis, provide some measure of device reliability, and (3) identifying the origin of fracture and methods of mitigation.

## CHAPTER 4

### JOHNS HOPKINS UNIVERSITY

#### 1. INTRODUCTION

This chapter summarizes the development by W.N. Sharpe, Jr. and coworkers, at Johns Hopkins University, of a testing environment for measuring the Young's modulus, Poisson's ratio, direct tensile strength, and fracture toughness of poly-Si thin films. This group's efforts have produced the following publications (the list was kindly provided by W.N. Sharpe, Jr.).

[1] B. Yuan, and W.N. Sharpe, Jr., "Mechanical Testing of Polysilicon Thin Films with the ISDG", *Experimental Techniques*, vol.21, no.2, p. 32-5, 1997.

[2] W.N. Sharpe, Jr., R. Vaidyanathan, B. Yuan, G. Bao and R.L. Edwards, "Effect of Etch Holes on the Mechanical Properties of Polysilicon" *Journal of Vacuum Science & Technology*, vol.15, no.5, pp. 1599-603, 1997.

[3] W.N. Sharpe, Jr., B. Yuan and R.L. Edwards, "A New Technique for Measuring the Mechanical Properties of Thin Films", *Journal of Microelectromechanical Systems*, Vol. 6, No. 3, pp.193-199, 1997.

[4] D.J. Chang and W.N. Sharpe, Jr., *Mechanical Analysis and Properties of MEMS Materials, Microengineering for Aerospace Systems*, The Aerospace Press of The Aerospace Corporation, in press, 1998.

[5] W.N. Sharpe, Jr. and B. Yuan, "Mechanical Testing of MEMS Materials", *Proceedings of the 1995 SEM Spring Conference on Experimental Mechanics*, Grand Rapids, pp. 698 - 701, 1995.

[6] W.N. Sharpe, Jr., B. Yuan, R. Vaidyanathan, and Edwards, R. L., "Direct Measurements of Young's Modulus and Tensile Strength of Polysilicon", *Late News Proceedings of the Solid-State Sensor and Actuator Workshop*, Hilton Head Island, SC, pp. 27 - 28, 1996.

[7] W.N. Sharpe, Jr., B. Yuan, R. Vaidyanathan and R.L. Edwards, "New Test Structures and Techniques for Measurement of Mechanical Properties of MEMS Materials", *Proceedings of the SPIE Symposium on Microlithography and Metrology in Micromachining II*, Austin, TX, pp. 78-91, 1996.

[8] W.N. Sharpe, Jr., B. Yuan, R.L. Edwards and R. Vaidyanathan, "Measurements of Young's modulus, Poisson's ratio, and Tensile Strength of Polysilicon", *Proceedings of the Tenth IEEE International Workshop on Microelectromechanical Systems*, Nagoya, Japan, pp. 424-429, 1997.

[9] W.N. Sharpe, Jr., B. Yuan and R.L. Edwards., "Variations in Mechanical Properties of Polysilicon", *Proceedings of 43rd International Symposium of the Instrumentation Society of America*, Orlando, FL, pp. 179-188, 1997.

[10] W.N. Sharpe, Jr., D.A. LaVan and R.L. Edwards., "Mechanical Properties of LIGA-Deposited Nickel for MEMS Transducers", *Proceedings Transducers '97*, Chicago, IL, pp. 607-610, 1997.

[11] W.N. Sharpe, Jr. and R.L. Edwards., "Advances in Tensile Testing of



*Polysilicon Thin Films*", *Applications of Experimental Mechanics to Electronic Packaging*", ASME EEP-VOL. 22/AMD-VOL. 226, pp. 113-116, 1997.

[12] W.N. Sharpe, Jr., D.A. LaVan, and A. McAleavey, "Mechanical Testing of Thicker MEMS Materials", *Micro-Electro-Mechanical Systems (MEMS)*, ASME DSC-Vol. 62/HTD-Vol. 354, pp. 93-97, 1997.

[13] W.N. Sharpe, Jr., R. Vaidyanathan, B. Yuan and R.L. Edwards, "A New Technique for Measuring Poisson's Ratio of MEMS Materials", *Materials for Mechanical and Optical Microsystems Symposium, Materials Research Society*, pp. 185-190, 1998.

[14] W.N. Sharpe, Jr. and B. Yuan, "Fracture Tests of Polysilicon Film", presented at *Thin Films - Stresses and Mechanical Properties - Symposium NN, Materials Research Society* and submitted to the proceedings (December, 1997).

[15] W.N. Sharpe, Jr., K. Turner and R.L. Edwards, "Polysilicon Tensile Testing with Electrostatic Gripping", presented at *Microelectromechanical Structures for Materials Research - Symposium N, Materials Research Society* and accepted for publication in the proceedings (April, 1998).

[16] W.N. Sharpe, Jr., K. Turner and R.L. Edwards, "Measurements of the Effect of Specimen Size on Young's Modulus and Tensile Strength of Polysilicon", *Late News Proceedings of the Solid-State Sensor and Actuator Workshop, Hilton Head Island, SC*, accepted for publication (June 1998).

What makes the above referenced work unique is the use of laser interferometry to accurately measure the relative displacements (of gold lines deposited on the specimen) needed to calculate axial and lateral strains. As a result, the authors have measured not only the tensile strength and fracture toughness (using a finite radius center notch) of poly-Si, but also its Young's modulus and Poisson's ratio.

The first generation testing procedure, described in References [1]-[14], uses an adhesive to grip the ends of the (3.5  $\mu\text{m}$  thick, 600  $\mu\text{m}$  wide, and 4000  $\mu\text{m}$  long) tensile specimen to a testing machine. Very reproducible results were obtained, suggesting that the experimental and material processing procedures are consistent and reproducible.

Unfortunately, the fabrication is associated with only one specimen per die, and involves a time consuming etching procedure. Moreover, the dimensions of the specimen in the plane of the film are relatively large compared to typical components of MEMS devices, and therefore the scatter in the experimental measured properties is not expected to represent the scatter in typical device components.

For these reasons, the group developed a second generation testing system, described in References [15]-[16], which involves an electrostatic gripping procedure similar to the one developed by Tsuchiya and coworkers (described in the previous chapter). This significant modification makes it possible to produce many different size specimens, each of smaller dimensions, on one die. This author's opinion is that when the system is fine tuned, it will be the most reliable system available for in-laboratory fundamental studies on mechanical properties of poly-Si.

Because the above referenced work is associated with two different procedures, this chapter is divided into two parts. The first describes the development of the first generation gripping system and the laser interferometry technique, as well as the

measurements made with this system of Young's modulus and Poisson's ratio, tensile strength, and fracture toughness. The second part summarizes the group's adoption of the electrostatic gripping device and preliminary results of Young's modulus, Poisson's ratio, tensile strength, and fracture toughness.

## 2. FIRST GENERATION GRIPPING SYSTEM

### General description of experimental technique

A schematic of the testing environment is shown in Figure 1. The tensile specimen, which is described subsequently, is placed between two grips, one attached to a fixed base, the other to a linear air bearing that eliminates friction in the loading mechanism. The force is applied through a piezoelectric translator (with a range of  $180\mu\text{m}$  and resolution of  $0.09\mu\text{m}$ , as reported in Reference [7]), and measured by a 4.5N load cell (with resolution of  $0.0045\text{N}$ , as reported in Reference [7]). The test is run under displacement control.

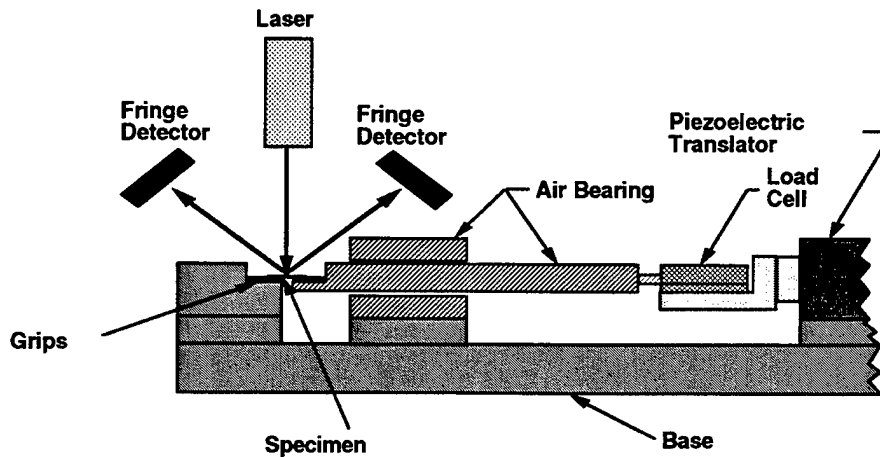


Figure 1- Schematic of the test setup (Reference [8]).

The Interferometric Strain/Displacement Gage (ISDG) is used for measuring strains. This optical technique measures the relative displacement between reflective gage markers, as shown schematically in Figure 2. In this work the markers are gold lines,

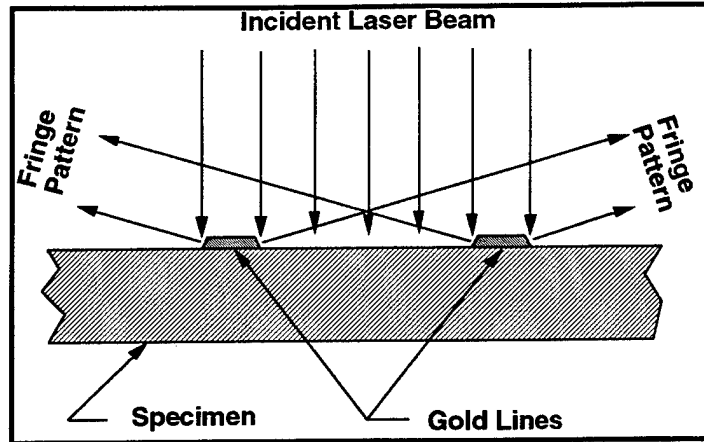
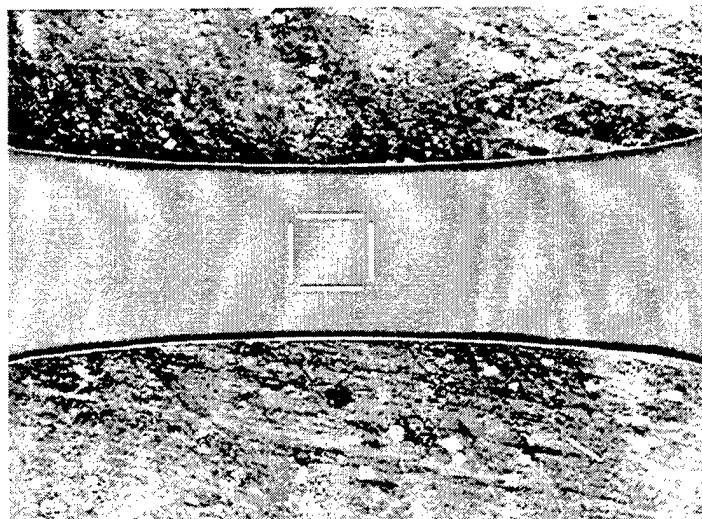


Figure 2- Schematic of the ISDG (Reference [8]).

$10\mu\text{m}$  wide,  $0.5\mu\text{m}$  high,  $200\mu\text{m}$  long, and  $250\mu\text{m}$  apart, as shown in the SEM micrograph of Figure 3. In this figure there are two sets of lines, one set perpendicular to the other. One set is used to measure the relative displacement in the direction of the applied force, the other in the direction perpendicular to the applied force. This allows measurement of both Young's modulus and Poisson's ratio. As explained subsequently, these lines are deposited on the specimen during processing.

Strain is measured as follows. An incident laser beam is used to illuminate the gold lines. The edges of the lines produce diffracted reflections that overlap and interfere. This produces fringe patterns that move as the lines undergo relative displacement. The motion of the fringe patterns is measured with fringe detectors, and in turn the strain is calculated. The authors report in Reference [8] that their ISDG system is associated with a relative uncertainty of  $\pm 3\%$ . The phenomena that contributes to this uncertainty is stated in Reference [8]. The optical principles and practical aspects of the ISDG technique have been reviewed by W.N. Sharpe, an authority on these systems, in *W.N. Sharpe, Jr., "An interferometric strain displacement measurement system," NASA Technical Memorandum 101638, 1989.*



**Figure 3- SEM photo of the biaxial strain gage (Reference [8]).**

### **Description of specimen**

The poly-Si specimen is shown mounted, using an adhesive, in the grips of the test machine in the center of Figure 4. There are two support strips parallel to the specimen that prevent damage of the specimen during fabrication and handling. These are cut (with a diamond saw), as shown in the figure, immediately before testing. Details of the alignment and precautions taken during handling, gluing and curing are presented in Reference [7].

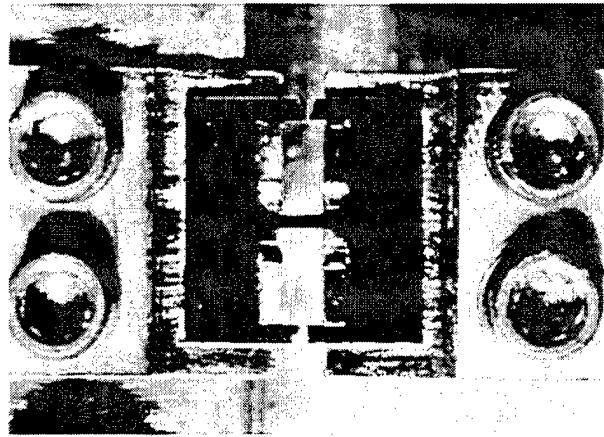


**Figure 4- A polysilicon specimen mounted in the grips of the test machine with the support strips cut (Reference [8]).**

### **Specimen fabrication**

The 3.5 $\mu\text{m}$  thick, P-doped poly-Si thin film specimens are manufactured at MCNC using the so called MUMPs surface micromachining process. They are released and prepared for testing at Johns Hopkins University. The steps needed to fabricate the specimen are quite involved, and the details are not repeated here. They can be recovered in References [7]-[8]. Only a brief description of the material and the back-etching procedure are described next.

It is important to note that MEMS devices fabricated at MCNC are comprised of two layers of poly-Si, deposited by LPCVD, each contained within sacrificial layers of PSG. The bottom layer of PSG is separated from a supporting silicon substrate by a layer of silicon nitride. The as-deposited films are amorphous; a fine grain, low internal stress, polycrystalline microstructure is achieved by annealing for one hour at 1050 $^{\circ}\text{C}$  (each layer is annealed separately). As shown in the cross-sectional TEM micrograph of Figure 5, the thickness of the first (second) deposit is 2 $\mu\text{m}$  (1.5 $\mu\text{m}$ ). It is observed that this final structure is nearly columnar. The poly-Si is doped during the annealing from the surrounding PSG. In Reference [8] it is reported that the PSG layer that separates the poly-Si layers was removed during processing, and that the second polysilicon layer was

deposited directly on top of the first.

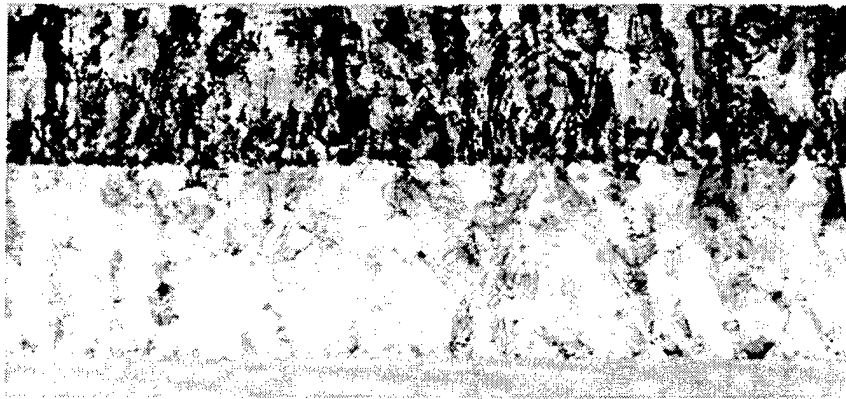


**Figure 5- TEM photograph of the two-layer polysilicon specimen. The bottom layer is 2.0  $\mu\text{m}$  thick and the darker top layer is 1.5  $\mu\text{m}$  thick (Reference [8]).**

Figure 6a shows a schematic of the specimen contained within a one-centimeter square carrier frame that includes the grip ends and the support strips. Figure 6b shows the evolution of section A-A, from the as received configuration to the final released configuration. The second (from the top) schematic in Figure 6b shows the ceramic carrier that was attached, for handling purposes, to the front of the die using an adhesive wax.

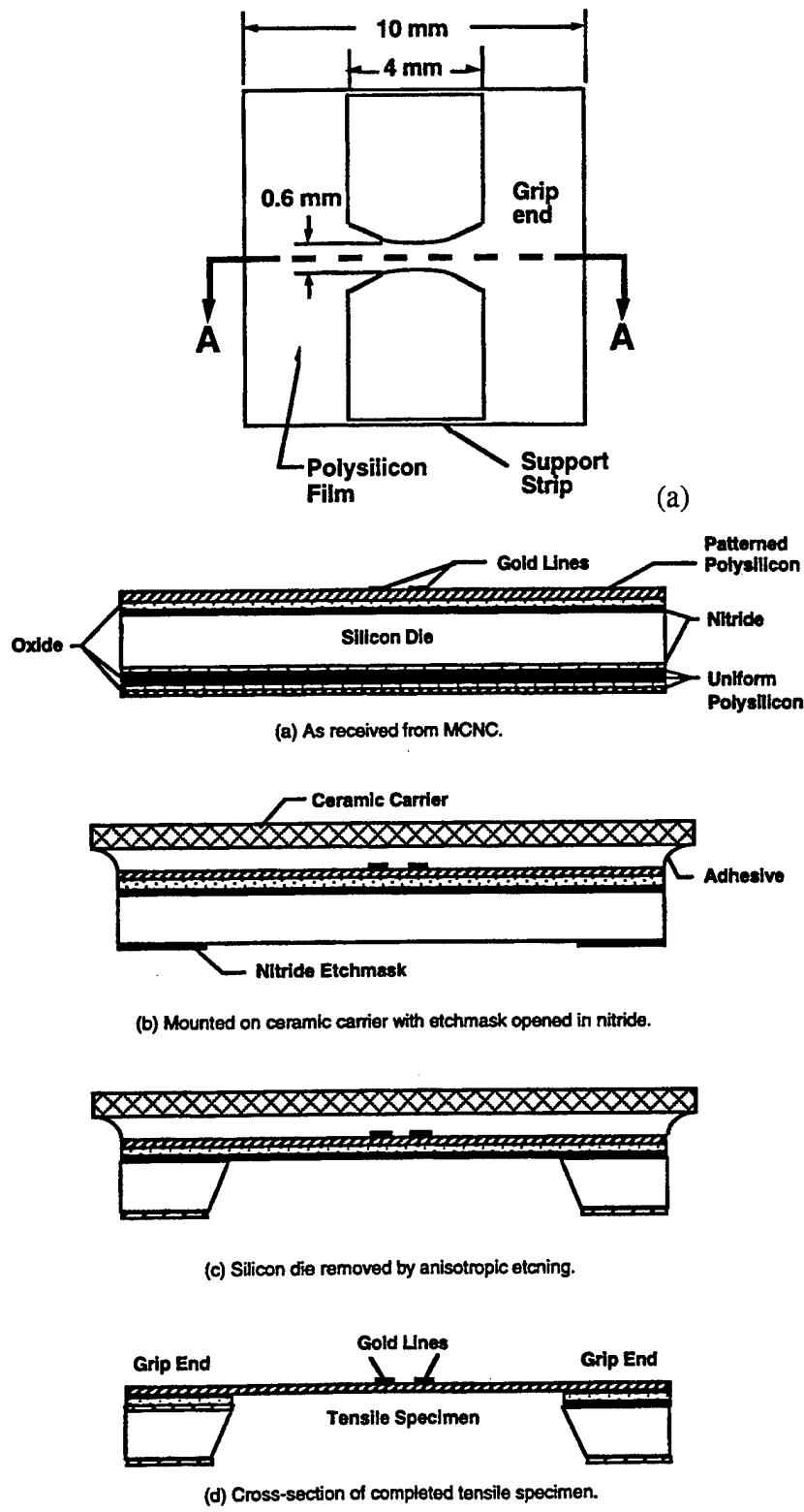


Figure 6- Schematic of; (a) poly-Si pattern, (b) back-etch process as viewed at section A-A of (a) (Reference [7]).

An SEM micrograph showing an oblique view of the specimen, taken from

Reference [7], is shown in Figure 7.

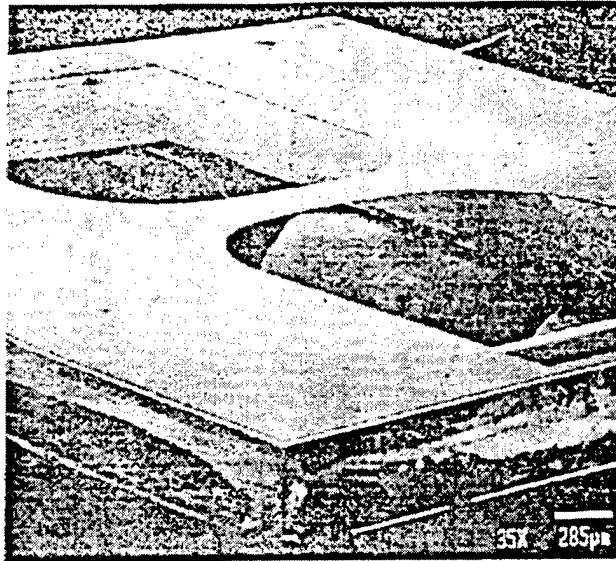
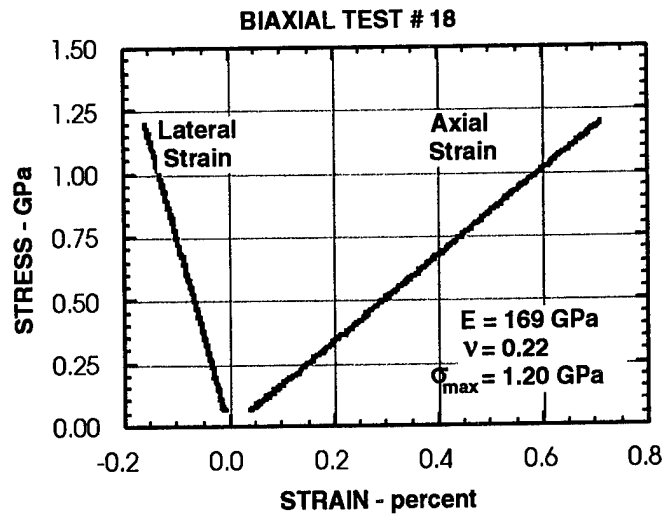


Figure 7- SEM micrograph of tensile specimen (Reference [7]).

## Results

### Young's modulus, Poisson's ratio, and tensile strength

Typical stress-strain curves are shown in Figure 8. As stated by the authors in Reference [8], the specimen buckles out-of plane when the support strips are cut, and therefore a preload is applied before initiation of displacement controlled loading. The figure indicates a tensile strength of 1.2GPa, Young's modulus of 169GPa and Poisson's ratio of 0.22. This latter measurement is the first on poly-Si.



**Figure 8- A typical stress biaxial-strain plot (Reference [8]).**

Table 1 presents the data for 48 tests on specimens produced during five MUMPs production runs. Ten specimens were tested from MUMPs 6, 10, and 11, and nine were tested from MUMPs 8 and 12. Note that it is this data that is reported in the previous chapter describing variations in mechanical properties of polycrystalline silicon.

**Table 1- Mechanical property data for polysilicon (Reference [8]).**

MUMPs	Young's Modulus (GPa)	Poisson's Ratio	Tensile Strength (GPa)
6	163 ± 4.78	-	1.23 ± .200
8	173 ± 6.94	-	1.27 ± .107
10	173 ± 2.00	-	1.14 ± .155
11	168 ± 7.15	0.22 ± .015	1.19 ± .155
12	168 ± 1.59	0.22 ± .003	1.17 ± .100
<b>All Data</b>	<b>169 ± 6.15</b>	<b>0.22 ± .011</b>	<b>1.20 ± .150</b>

The statistical analyses performed by the authors showed that (1) at 95% confidence the average tensile strength of 1.2GPa is statistically equal to the average strength of the individual runs, (2) at 95% confidence the average Young's modulus of 169GPa is statistically different than the average of MUMPs 6 and of MUMPs 10, (3) the coefficient of variation for all of the Young's modulus data, all of the strength data, and all of the Poisson's ratio data are, respectively, 3.6%, 12.5% and 5%. All and all the results suggest that the tests and the fabrication processes are very consistent and reproducible.

### Fracture toughness

In Reference [14] the authors used the experimental procedure to measure the



fracture toughness of poly-Si, from the MUMPs 13 run, using the specimen shown schematically in Figure 9. The fabrication process is not reported; it is similar to the one described previously for the tensile specimens. It should be mentioned that this group tried to use the first generation device to measure fracture toughness, but was not successful (Reference [7]).

This fracture mechanics configuration consists of a  $3000\mu\text{m}$  wide by  $4000\mu\text{m}$  long strip which contains a  $100\mu\text{m}$  central crack. The relevant dimensions of the crack are shown in the figure. The crack-tip radius is reported in Reference [14] as  $1\mu\text{m}$ . In these experiments the ISGD system is used, with the gold pads shown in Figure 2, to measure the COD at the center of the crack. Note that because the pads are at a finite distance from the crack surfaces, the relative displacement that is measured is not exactly the COD. A photograph of the center crack and the gold pads is shown in Figure 10.

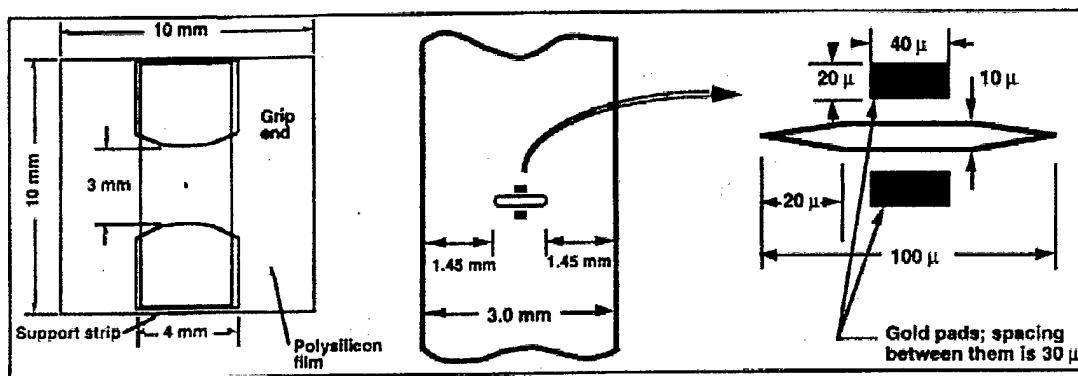


Figure 9- Schematic of fracture specimen (Reference [14]).

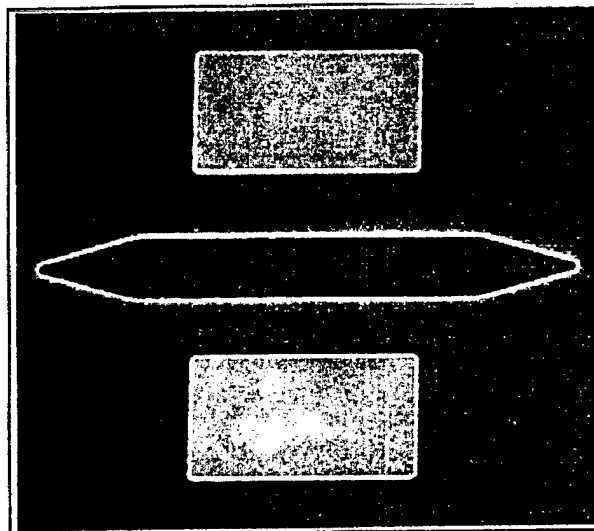


Figure 10- Close-up photograph of the center crack and the gold pads (Reference [14]).

If the crack in this configuration were mathematically sharp, the stress intensity

factor and plane stress COD at the center of the crack would be

$$K = \frac{P}{A} \sqrt{\pi a}$$

(1a)

$$COD = 2 \frac{Pa}{AE}$$

(1b)

where  $P$ ,  $a$  and  $A$  are, respectively, the applied force, half-crack length, and cross-sectional area. Young's modulus in Equation (1b) was assumed to be 169GPa; this value corresponds to the average value measured in the tests described in the previous section.

The results of the 12 tests are presented in Figure 11 (COD) and Table 2 (fracture toughness). It is observed that the agreement between the theoretical and measured COD is reasonable. The differences are due to the fact that the crack is of finite thickness and not sharp, and that the COD is measured away from the crack surfaces.

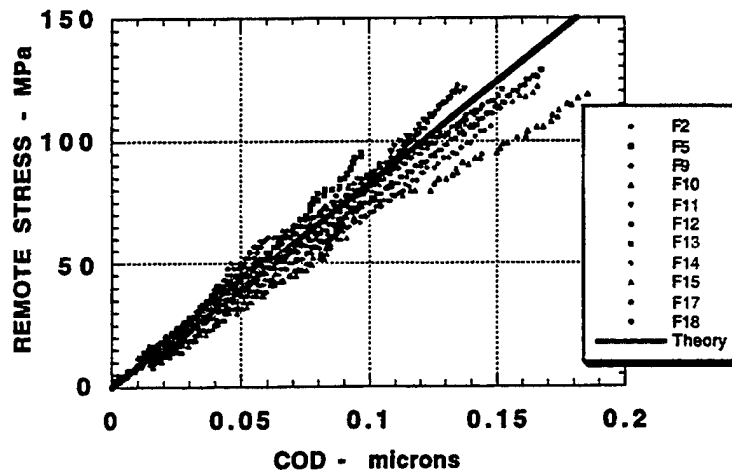


Figure 11- Measured stress versus COD and comparison with theory (Reference [14]).

The average fracture toughness, its standard deviation, and its coefficient of variation are, respectively,  $1.41 \text{MPa}\cdot\text{m}^{1/2}$ ,  $\pm 0.15 \text{MPa}\cdot\text{m}^{1/2}$ , and 11%. The fracture toughness of single crystal silicon is anisotropic, its range typically reported as  $0.7\text{-}1.2 \text{MPa}\cdot\text{m}^{1/2}$  (R. Ballarini, R.L. Mullen, Y.Yin, H. Kahn, S. Stemmer and A.H. Heuer, "The fracture toughness of polysilicon microdevices: a first report," *Journal of Materials Research*, Vol. 12, No. 4, April 1997).

The values in Table 2 may not represent the true fracture toughness because the notch tip is of finite radius. However, since this radius is much smaller than the other dimensions, the values are expected to be closer to the true toughness than those reported

by Tsuchiya (in the previous chapter) and by Ballarini and coworkers (whose work is described in the next chapter).

Test	F2	F3	F9	F10	F11	F12	F13	F14	F15	F16	F17	F18
$K_{max}$	1.14	1.19	1.32	1.49	1.51	1.52	1.51	1.28	1.53	1.38	1.42	1.61

Table 2- Fracture toughness ( $\text{MPa}\cdot\text{m}^{1/2}$ ) (Reference [14]).

### 3. SECOND GENERATION GRIPPING SYSTEM

#### General description of experimental technique

Because of the previously discussed limitations of the first generation experimental procedure, the authors replaced the adhesive based gripping system with an electrostatic one similar to the one developed at TCRDL and described in the previous chapter. A schematic of the second generation environment is shown in Figure 12. One end of the specimen, which is described subsequently, is attached to a  $550\mu\text{m}$  wide probe through electrostatic forces. This probe, which is cut from a silicon chip and insulated by a  $600\text{ nm}$  thick layer of nitride, is in turn mounted to a load cell (as reported in Reference [15], two load cells were used, with ranges of 5 and 100 grams). Alignment of the specimen is achieved by mounting the load cell and probe on a manual three-axis translation stage. The other end of the specimen is attached to a five-axis piezoelectric stage (with a resolution of  $20\text{ nm}$ , as reported in Reference [15]), which allows precise alignment, and whose movement produces a tensile force on the specimen.

Two methods of strain measurement are applied; both correct for the stiffness of the load cell. On the narrower specimens the movement of the piezoelectric stage is monitored with a  $100\mu\text{m}$  range capacitance gage. On the wider specimens, the ISGD system is also used.

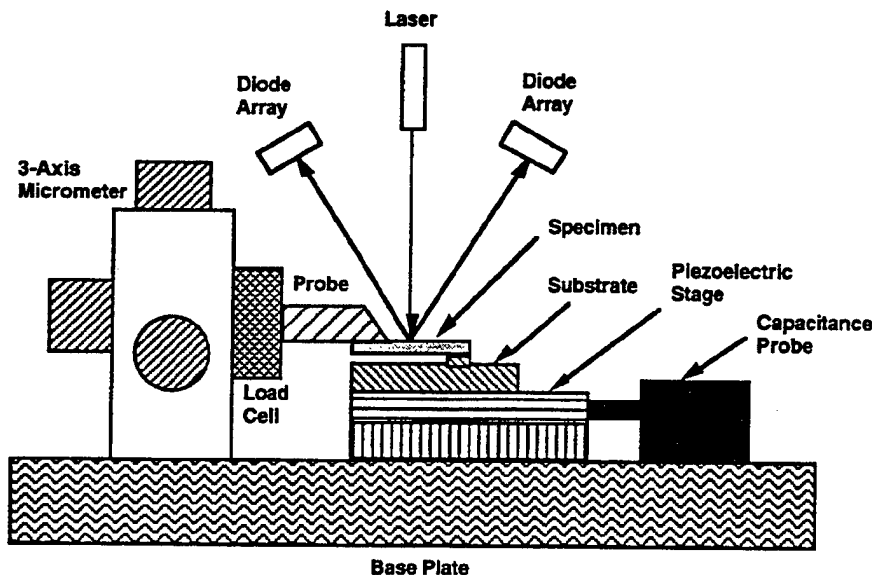


Figure 12- Schematic of testing environment (Reference [15]).

### Specimen fabrication

The specimens were fabricated on the MUMPs 19 and 21 runs. Figure 13 shows the 18 specimens that come on each one square centimeter die. Figure 14 shows a schematic of an individual specimen, showing the dimensions of the free end (which is attached to the probe) and the fixed end. Note that the  $600\mu\text{m}$  width of the free end is slightly larger than the  $550\mu\text{m}$  probe width. Apparently this difference made it more convenient to align the specimen. Size effects were studied by varying the thickness, width, and length of the specimens. One row of specimens was made  $1.5\mu\text{m}$  thick, the other  $3.0\mu\text{m}$  thick. Each row contained one  $50\mu\text{m}$  wide (in the test section) specimen, two that were  $20\mu\text{m}$  wide, three  $5\mu\text{m}$  wide, and three  $2\mu\text{m}$  wide. Three specimens are  $500\mu\text{m}$  long (in the straight section), three are  $200\mu\text{m}$  long, two are  $50\mu\text{m}$  long, and one is  $20\mu\text{m}$  long. The dimensions of the smallest specimen, which was  $1.5 \times 2 \times 20\mu\text{m}$ , are comparable to those of a typical MEMS component (an attachment beam, for example).

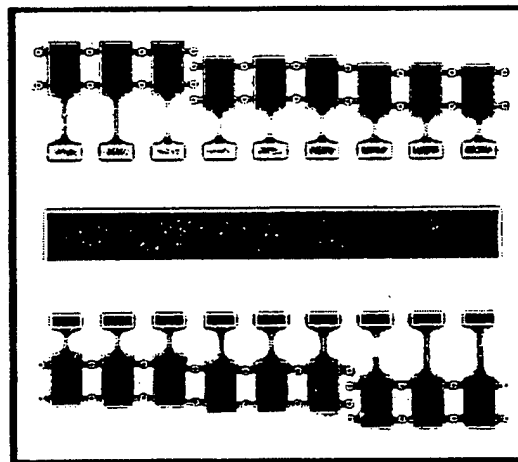


Figure 13- Eighteen specimens on a one square centimeter die (Reference [15]).

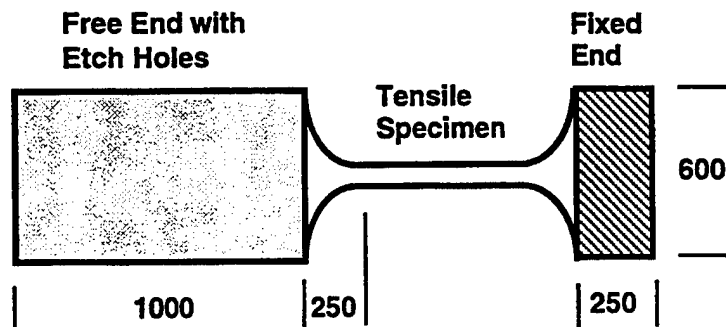


Figure 14- Schematic of the specimen, with dimensions in  $\mu\text{m}$ . The length, thickness, and width vary, as described in the text (Reference [15]).

## Results

As stated by the leading author at the MRS 1998 Spring meeting, because the second generation system is relatively new, the results presented next are preliminary.

Young's modulus was calculated from the specimen's force-displacement plot; for the wider specimens it was also calculated from strain calculated from the relative displacements measured using the ISGD system. Using these two methods proved important, as explained next. Typical plots for two specimens with identical dimensions in the plane of the film ( $20\mu\text{m} \times 500\mu\text{m}$ ), but of different thicknesses ( $1.5\mu\text{m}$  versus  $3.5\mu\text{m}$ ), are shown in Figure 15. It is observed that, for the thicker specimen, the values of modulus determined using the two methods is practically the same. For the thinner specimen, on the other hand, the values are significantly different. This discrepancy is currently being investigated.

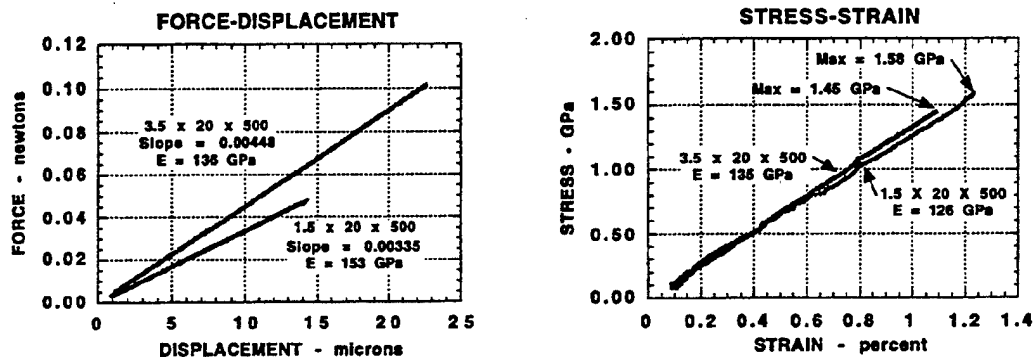


Figure 15- Force-displacement (left) and stress-strain (right) plots of two specimens identical in shape, but of different thickness (Reference [15]).

Figure 16 presents the measured Young's modulus and tensile strength of all the specimens. Those for the  $600\mu\text{m}$  wide specimens were taken from Reference [8] and included for comparison purposes. It is observed that the scatter in the Young's modulus measurements is significant. At this point it may be premature, but it seems that the strength exhibits the size effect typical of brittle materials; the widest specimens from Reference [8] are, on the average, the weakest.

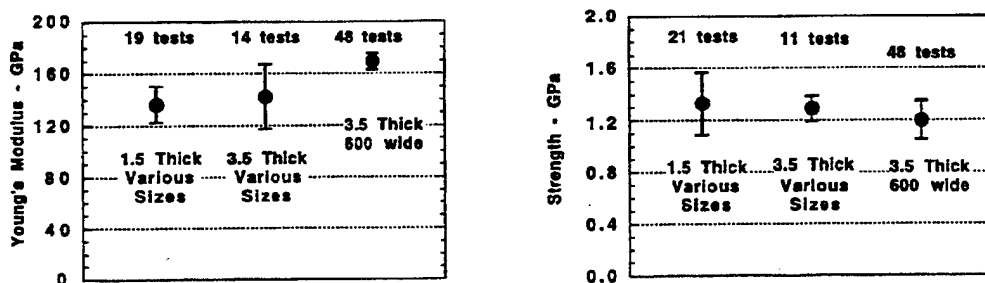


Figure 16- Modulus and strength data for specimens of various sizes (Reference [15]).

#### 4. CRITIQUE

The first generation testing environment introduced the use of laser interferometry to accurately measure strains in poly-Si processed using MEMS technology. It was used to produce very valuable data for elastic modulus, Poisson's ratio, and the direct tensile strength of poly-Si thin films.

The second generation system, which combines the use of electrostatic gripping with laser interferometry, allows measurements on specimens whose dimensions are comparable to MEMS devices. In the scientist's opinion, when the system described in this chapter is fine-tuned, it will be the most robust testing environment for measuring the elastic modulus and direct tensile strength of poly-Si films.

## CHAPTER 5

### BERKELEY SENSOR AND ACTUATOR CENTER

#### 1. INTRODUCTION

This section describes the experiments conducted by P.T. Jones, G.C. Johnson and R.T. Howe at the University of California at Berkeley (UCB), to measure the tensile strength and Young's modulus of poly-Si at scales relevant to microelectromechanical devices. Their work will appear as

[1] *P.T. Jones, G.C. Johnson and R.T. Howe, "Fracture strength of polycrystalline silicon," to appear in Proceedings of the 1998 MRS Spring Meeting, San Francisco.*

This group tested P-doped specimens from MCNC's MUMPs19 and MUMPs21 production runs, and undoped specimens produced at UCB. Their tests on the MCNC material represents their contribution to the previously mentioned round-robin program for measuring tensile strength and Young's modulus of poly-Si films. A comparison of the results for the two different MCNC MUMPs runs showed that there were no run-to-run variations of mechanical properties using the nominally identical process. As expected, a comparison of the results for the MCNC material and the Berkeley material showed that differences in processing can result in variations of mechanical properties.

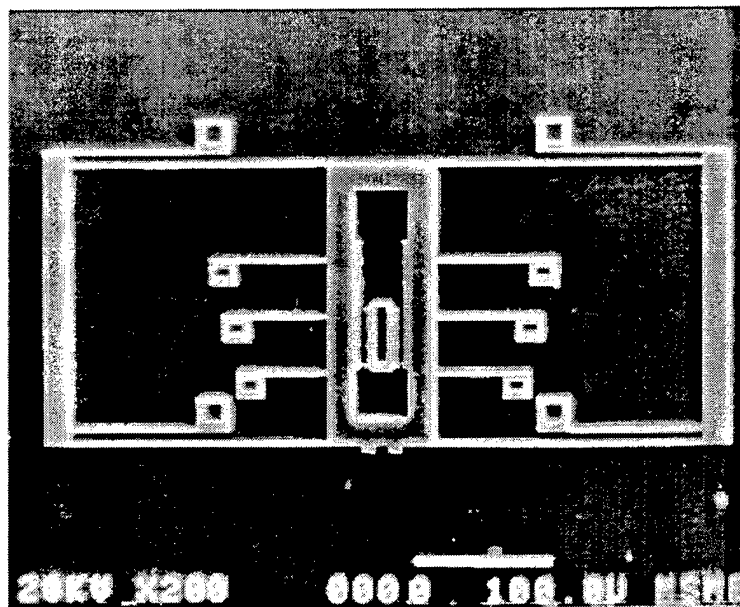


Figure 1: SEM micrograph of fracture structure test device. The six cantilever beams to be tested are attached to a shuttle which is anchored by a folded flexure structure (Reference [1]).

This group's device determines the fracture (tensile) strain of poly-Si films by measuring the displacement at fracture of a series of cantilever beams bending in the plane of the film. The displacement is related to the strain through the analytical solution of the elastica. Concomitantly a different device, consisting of a series of beams of different length bending out of the plane of the film, is used to measure Young's modulus. Assuming the films are isotropic, the fracture strain and Young's modulus are used to determine the (bending) tensile strength.

## 2. GENERAL DESCRIPTION OF EXPERIMENTAL PROCEDURE

Figure 1 shows a SEM micrograph of the  $500\ \mu\text{m} \times 320\ \mu\text{m}$  test structure used to measure the fracture strain. Six cantilever beams (three different length pairs) are attached to a shuttle, which in turn is anchored to the substrate by a folded-flexure frame. The beams are nominally  $2\ \mu\text{m}$  thick,  $3\ \mu\text{m}$  wide, and have lengths of  $50\ \mu\text{m}$ ,  $60\ \mu\text{m}$ , or  $70\ \mu\text{m}$ . The authors measured the thickness and width, respectively, as  $1.9\ \mu\text{m}$  and  $2.8\ \mu\text{m}$  (*private communication with P.T. Jones*). The frame is designed to permit a relatively large displacement of the beams in the plane of the film, and relatively small in-plane rotation and out-of-plane displacement of the assembly.

The authors mention the following advantages of this device over uniaxial structures.

1. Its small size allows a large number of devices to be fabricated on a single die. This, coupled with the fact that as many as six data points could be obtained from a single device, allows a large amount of statistical data to be obtained.
2. The state of strain in the beam is independent of the thickness of the film; therefore the thickness need not be measured. Moreover, this allows application of the test device to the study of bending of other materials such as deep-etched single crystal silicon, or even hexsil structures (*C.G. Keller and R.T. Howe, "Hexsil tweezers for teleoperated micro-assembly," Proceedings IEEE. The Tenth Annual International Workshop on Micro Electro Mechanical Systems. An Investigation of Micro Structures, Sensors, Actuators, Machines and Robots, Nagoya, Japan, 26-30 Jan. 1997. New York, NY, USA: IEEE, 1997. p. 72-7*).
3. The beam can achieve large deformations before fracture. This is an advantage since the displacement measurement resolution is  $0.2\ \mu\text{m}$ .
4. The dimensions of the specimens are comparable to those of typical MEMS components.
5. The structural layer of the device can be defined using only a single mask. It is noted in Reference [1] that the tested devices were fabricated using a minimum of two masks; one defines the anchor region, the other defines the structural layer.

The authors also note that the force on the beam cannot be directly measured. This necessitates, as explained subsequently, a different device to determine the Young's modulus.



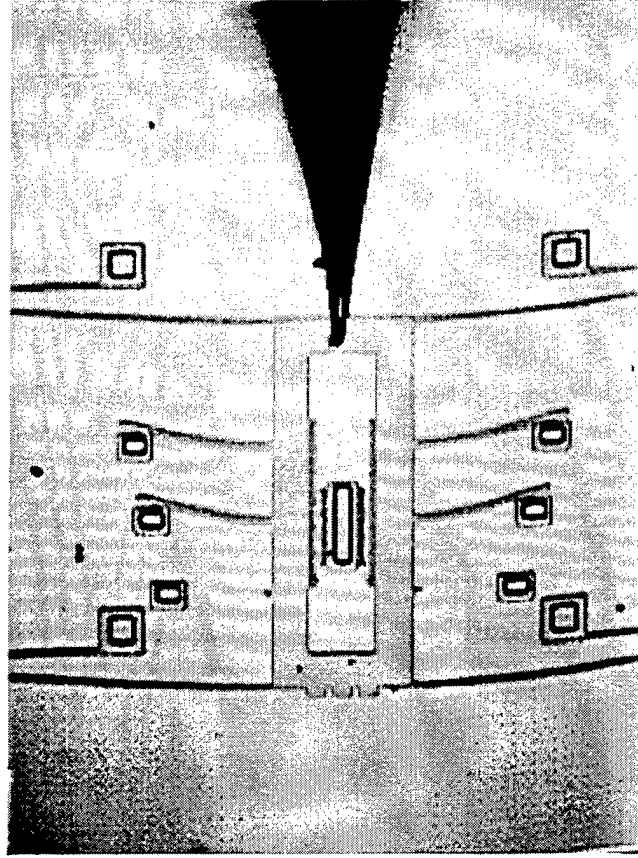


**Figure 2- Scanned video image of fracture structure test device. An off chip probe loads the shuttle of the device. Here the shortest two beams have already broken off as other beams continue to be bent (Reference [1]).**

As shown in Figure 2, the beams are loaded when they come into contact with anchored square structures as the shuttle is pushed, at a continuous rate of  $0.025 \mu\text{m/s}$ , by an off-chip probe. The shuttle is marked with a vernier scale. A video system monitors to a  $0.2 \mu\text{m}$  resolution the shuttle's displacement, and the vernier is used to determine the fracture displacement of each beam. This latter displacement is used in conjunction with the elastica solution to determine the fracture strain. The analysis, which is standard and not presented here, appears in *P.T. Jones, G.C. Johnson, "Micromechanical Structures for Fracture Testing of Brittle Thin Films," ASME International Mechanical Engineering Congress and Exposition Micro-Electro-Mechanical Systems (MEMS), DSC-Vol. 59, p. 325-330, 1996*. A close-up view of one beam is shown in Figure 3, which clearly demonstrates that the end of the beam undergoes a relatively large displacement.

The following uncertainty arises. The design is symmetric with respect to the direction of loading, and as a result, two beams of equal length are tested simultaneously. It is unlikely that both fracture at the same exact time. After the first beam breaks, symmetry is lost, and fracture of the second beam may occur at a different strain level. The authors considered this issue (*private communication with P.T. Jones*). They did not observe rotation of the shuttle during testing of the shortest four beams. In some tests,

only one of the last of the longest beams remains intact, and the shuttle shifts upwards; the results from these tests are discarded. As a check, they compared the failure strains of the longest beams with those of the shorter beams, and found a close match.

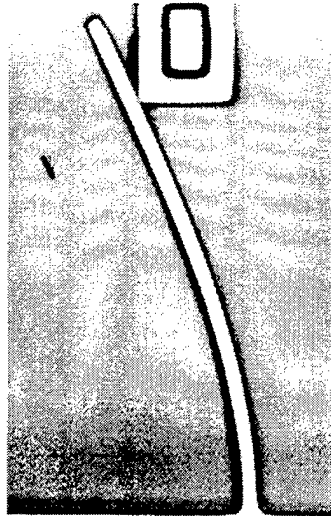


**Figure 3- Scanned video image of a  $2.8\ \mu\text{m}$  wide by  $1.9\ \mu\text{m}$  thick beam at a large displacement. The distance from the fixed end of the beam to the contact point is  $70\ \mu\text{m}$ . The beam has deflected  $21.6\ \mu\text{m}$  (Reference [1]).**

### 3. SPECIMEN FABRICATION

The above referenced paper does not provide the details of the fabrication processes. These could easily be recovered from UCB and MCNC. What is described in the following.

The MCNC films were deposited at  $610^\circ\text{C}$ , and then sandwich-P-doped (as described in the JHU summary) during a 1 hour furnace anneal at  $1050^\circ\text{C}$ . The structures released from MUMPs19 were both furnace dried and super-critical carbon dioxide dried (*G.T. Mulhern, D.S. Soane and R.T. Howe, "Supercritical carbon dioxide drying of microstructures," Transducers '93, pp. 296-299, 1993*).

The Berkeley undoped poly-Si was deposited at  $610^\circ\text{C}$  and 300 mTorr, sandwiched by LTO and furnace annealed at  $950^\circ\text{C}$  for  $\frac{1}{2}$  hour.

### 4. FRACTURE TENSILE STRAIN RESULTS

The measured average displacement at fracture and average strain at fracture are shown, respectively, in Tables I and II (these were reproduced from Reference [1]).

**Table I- Average Beam Displacement ( $\mu\text{m}$ ) at Fracture for the Materials Tested. Uncertainties are one standard deviation of the measured displacement (Reference [1]).**

	MUMPS21 CO <sub>2</sub> Dry	MUMPS19 Furnace Dry	MUMPS19 CO <sub>2</sub> Dry	BSAC
50 $\mu\text{m}$ beams	13.5 $\pm$ 1.2	13.1 $\pm$ 1.4	13.2 $\pm$ 1.6	10.4 $\pm$ 0.9
60 $\mu\text{m}$ beams	18.6 $\pm$ 2.3	18.6 $\pm$ 2.5	17.7 $\pm$ 1.7	14.7 $\pm$ 2.0
70 $\mu\text{m}$ beams	25.4 $\pm$ 4.1	27.1 $\pm$ 3.6	25.7 $\pm$ 2.4	20.1 $\pm$ 2.3
Beams Tested	92	64	68	76

**Table II- Estimated Maximum Strain State in Beams at Failure (%) (Reference [1]).**

	MUMPS21 CO <sub>2</sub> Dry	MUMPS19 Furnace Dry	MUMPS19 CO <sub>2</sub> Dry	BSAC
Average	1.5 $\pm$ 0.2	1.5 $\pm$ 0.2	1.5 $\pm$ 0.2	1.2 $\pm$ 0.1
Minimum	0.81	1.10	1.18	0.90
Maximum	1.94	1.91	1.89	1.73

The authors' results and conclusions are summarized as follows.

1. A Student's t-test of the data suggests that the fracture strain of the MUMPs poly-Si is statistically different than that of the Berkeley poly-Si. The authors attribute this to differences in processing (including the fact that one material is doped, the other undoped), which results, among other things, in different levels of side-wall roughness.
2. No statistical difference exists between the fracture strains of (MCNC) specimens that were super-critically carbon dioxide dried and those that were furnace dried.
3. All MUMPs specimens have the same average fracture strain.

## 5. YOUNG'S MODULUS DEVICE AND RESULTS

The force applied to the specimen in the fracture strain device cannot be measured directly. Therefore the authors used the device suggested by Tai (*Y.C. Tai, "IC-Processed Polysilicon Micromechanics: Technology, Material, and Devices," Dissertation - University of California at Berkeley, 1989*) to determine Young's modulus of the MUMPs21 poly-Si films. As shown in Figure 4, it is comprised of an array of relatively wide cantilever beams 15  $\mu\text{m}$  wide, 2  $\mu\text{m}$  thick. Their lengths varied from 25 to 1000  $\mu\text{m}$  in 5  $\mu\text{m}$  steps. However, most of the beams were too compliant for testing (*private communication with P.T. Jones*). A Dektak 3030 profiler is used to measure the

out-of-plane displacement of the free ends of the cantilever beams for a variety of applied loads. The Young's modulus  $E$  may be determined from the equation

$$E = \frac{4(1-\nu^2)PL^3}{\delta bh^3}$$

(1)

where  $\nu$  is Poisson's ratio (assumed to be 0.25),  $P$  is the applied end load,  $L$  is the length of the beam,  $\delta$  is the end displacement of the beam,  $b$  is the width of the plate, and  $h$  is the film thickness. The displacement of the end of the beam is measured relative to small anchored plates on either side of the beam.

It is important to note that the modulus determined using this device is associated with bending out the plane of the film, while the fracture strain specimens bend in the plane. There is no evidence that suggests the films tested are isotropic. Indeed, the MCNC films are typically columnar, as described in the work at JHU, and probably transversely isotropic. This point will apparently be discussed further in the summary of the round-robin tests (private communication with P.T. Jones).

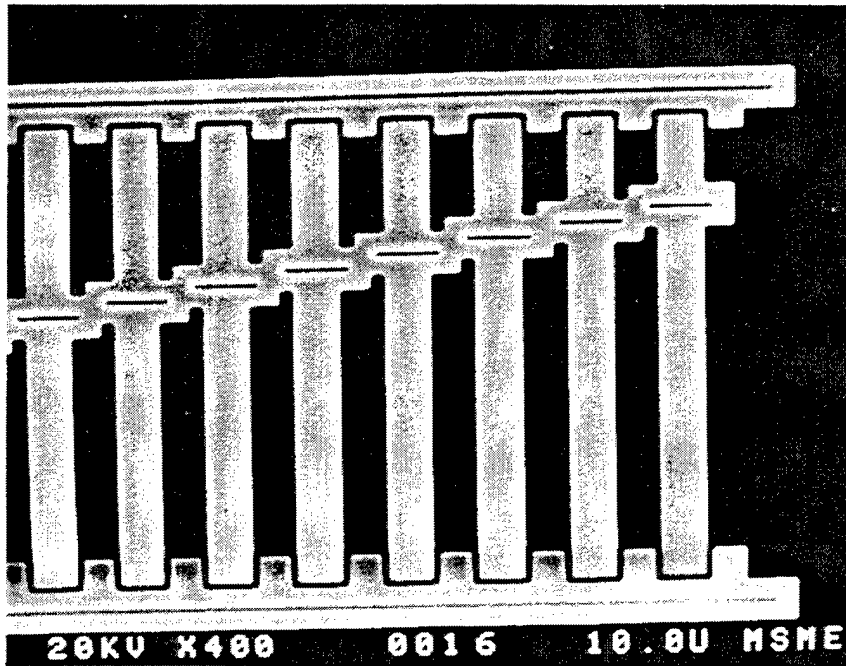


Figure 4- SEM of cantilever "beams" used for determining Young's modulus (Reference [1]).

Plots of end displacement versus beam length, for three different applied forces, are shown in Figure 5. These plots show that the displacement obeys Equation (1) if Young's modulus is set equal to  $173 \pm 20$  GPa, where the uncertainty is a single standard deviation of the measured values.

Using these values of the modulus, and assuming that the modulus measured is equal to the in-plane modulus, the average tensile strength becomes 2.1GPa and 2.6GPa for the MUMPS and Berkeley films, respectively. However, this also assumes that the material remains linear elastic up to the maximum strain. This point was brought up by Arthur H. Heuer (of CWRU) after the authors presented this work at the MRS Spring 1998 meeting. There is no evidence that the material is linear elastic at the strain levels measured in the experiments described above. Silicon whiskers in bending do remain elastic at room temperature up to failure strains approximately equal to 1%, as shown in Figure 6 (*G.L. Pearson, W.T. Read, Jr. And W.L. Feldmann, "Deformation and fracture of small silicon crystals," Acta Metallurgica, Vol. 5, pp. 181-191, 1957*).

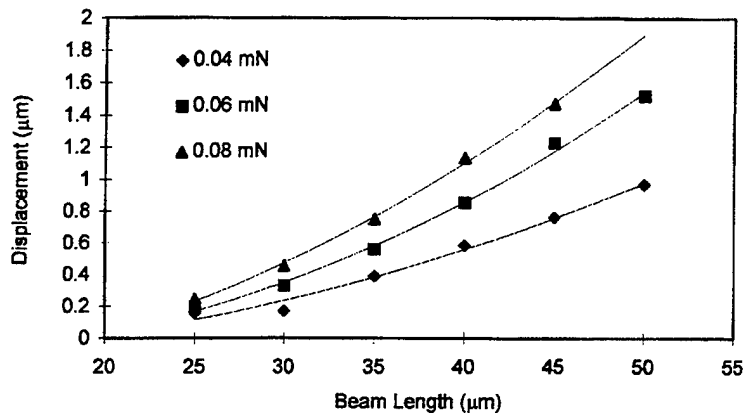


Figure 5- Plot of displacement vs. beam length for three different force settings using the Young's modulus test device (Reference [1]).

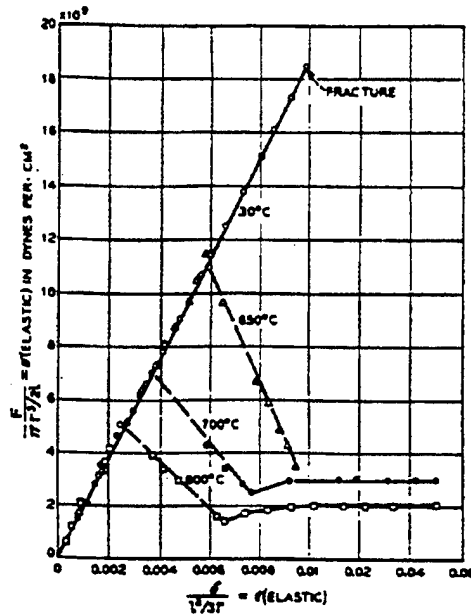


FIG. 4. Load-deflection curves for silicon whiskers at several temperatures.

Figure 6- Load-deflection curves for silicon whiskers at several temperatures (Reference provided in text).

## 6. CRITIQUE

The testing environment described in this chapter relies on relatively simple (in-plane flexural) loading and optical observation systems to measure (in a very reproducible way) the fracture strain of thin poly-Si films. For measuring fracture strain, the system appears to be sufficiently robust. However, the beam bending system used to determine the Young's modulus suffers from the fact that the bending is out of the plane of the film, and thus measures a modulus which may not be equal to the one associated with the in-plane bending specimens.

## CHAPTER 6

### EXPONENT ANALYSIS

#### 1. INTRODUCTON

This chapter summarizes the experimental research performed by S.B. Brown, W. Van Arsdell and C.L. Muhlstein at Exponent (formerly Failure Analysis Associates) on environmentally assisted fatigue crack growth in poly-Si. Their work will appear as

[1] *S.B. Brown, W. Van Arsdell and C.L. Muhlstein, "Materials reliability in MEMS devices," Transducers 1997, 1997 International Conference on Solid-State Sensors and Actuators, Chicago, Illinois, June 16-19, 1997.*

This group has demonstrated that poly-Si (from the MCNC MUMPs13 run) is associated with stress corrosion cracking in the presence of moisture. This is an important result that has direct implications on the long term reliability of MEMS devices.

#### 2. DESCRIPTION OF EXPERIMENTAL PROCEDURE

This group developed the in-plane resonant fatigue device shown in Figure 1 to study slow crack growth in poly-Si. The notched cantilever specimen is attached to a wedge shaped plate that serves as the resonant mass. Two sets of comb drive structures are formed along the two long straight sides of this mass. One provides electrostatic actuation, the other capacitance sensing of motion. A close-up view of the notched cantilever specimen is shown in Figure 2.

The dimensions of the device are not provided in the above referenced paper, because the paper focuses on the demonstration that poly-Si is associated with stress corrosion cracking. Quantitative measurements of stress or strain levels during the experiments are not reported. From the micrographs it is observed that the device and specimen are, respectively, on the order of hundreds and tens of microns.

The authors do state that the geometry of the notch was selected to ensure that at resonance the specimen fractures immediately (a very short amount of time is obviously needed to reach resonance). Subsequent plots of the data are normalized with respect to the excitation voltage required to break the specimen immediately.

Evidence of crack growth is searched for by measuring variations in time of the natural frequency of the device. (The frequency depends on the stiffness of the structure; as the crack grows the stiffness decreases). S. Brown has used this strategy (with different devices) to demonstrate environmentally assisted fatigue crack growth in single crystal silicon and nickel (*J.A. Connally and S.B. Brown, "Slow crack growth in single-crystal silicon," Science, Vol. 256, pp. 1537-1539, 12 June, 1992; J.A. Connally and S.B. Brown, "Micromechanical fatigue testing," Experimental Mechanics, pp. 81-90, June 1993; S.B. Brown, G. Povirk and J. Connally, "Measurement of slow crack growth in silicon and nickel micromechanical devices," Proceedings, MEMS-93, Fort Lauderdale, Florida, pp. 99-104, February 7-10, 1994*). The base line (first mode)

frequency is found by sweeping a range of frequencies around the expected response, and observing the displacement amplitude. A second order polynomial is used to fit the peak, and in turn the maximum amplitude is calculated. Changes in resonant frequency are measured as follows. For a period of time, a defined voltage is used to excite the specimen at the peak frequency. Re-evaluation of the frequency response by sweeping at the excitation frequency permits measuring of the changes.

### 3. RESULTS

The experiments were conducted at 75% relative humidity and 27°C. The results are presented in Figure 3. This plot is a slight modification of the traditional way of presenting fatigue data. The vertical axis typically presents the applied stress. To eliminate the effects of uncertainties in the displacement measurements, the modulus required to relate displacement to stress, and other parameters, the vertical axis was chosen as the excitation, normalized with respect to the immediate fracture excitation.

The data clearly shows that slow crack growth occurs. The only question that arises is whether the growth is due to stress, or to humidity. The authors claim that they obtained preliminary results (not presented in Reference [1]) that showed crack growth

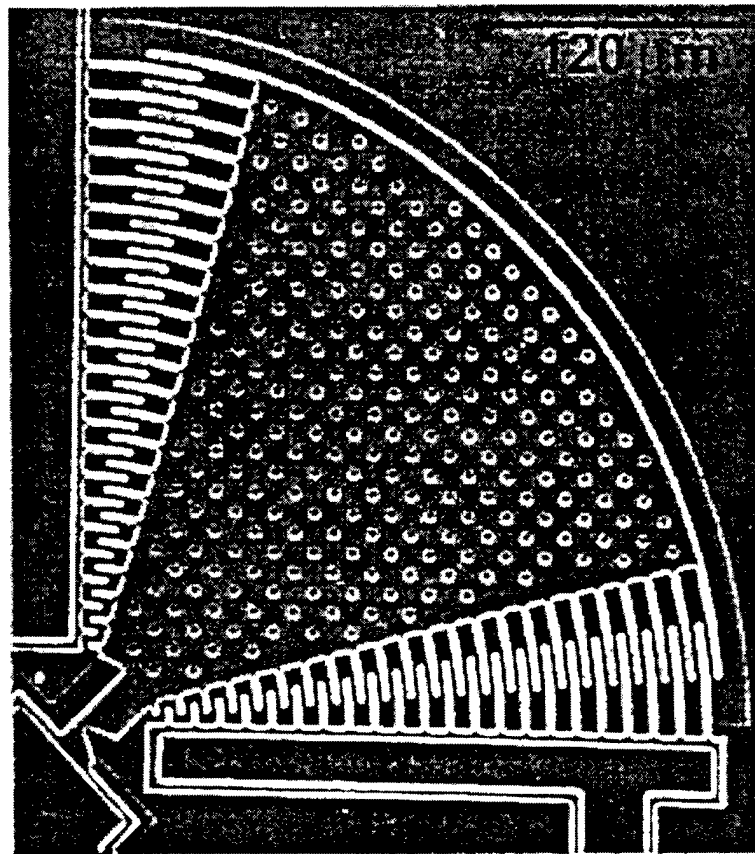


Figure 1- In-plane resonant fatigue device (Reference [1]).



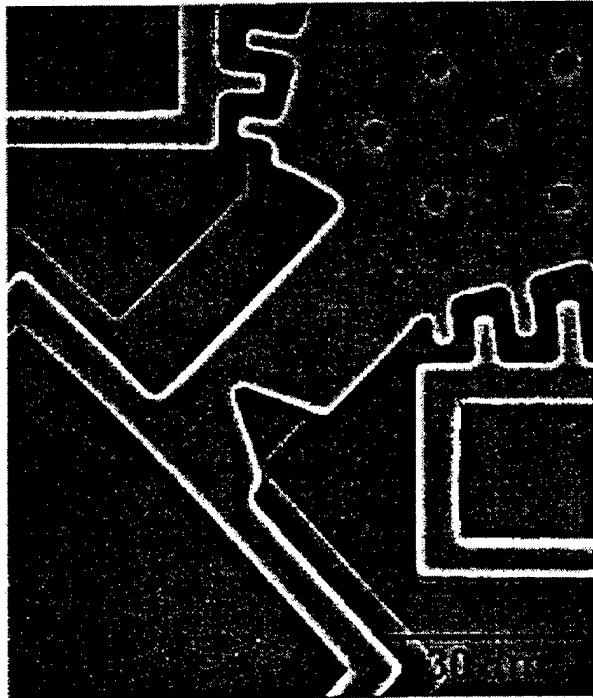


Figure 2- Close-up view of notched cantilever specimen (Reference [1]).

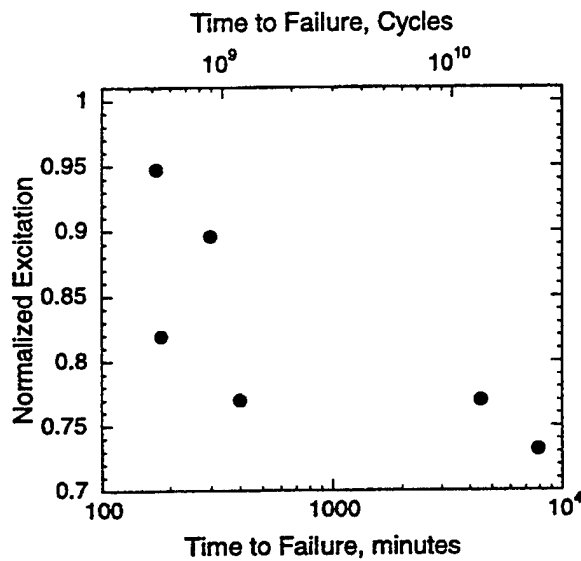


Figure 3- Time to failure versus normalized excitation (Reference [1]).

requires moisture. Furthermore, they attribute the phenomena to stress corrosion of the native oxide on the surface of the specimen.

As will be discussed in the next chapter (which summarizes the work performed by the scientist and coworkers at Case Western Reserve University), there is some evidence that suggests cyclic loads could reduce the strength of poly-Si in the absence of moisture.

#### **4. CRITIQUE**

The experiments described above are very important; they've shown that poly-Si is susceptible to environmentally assisted subcritical crack growth. This has significant implications for long term durability of MEMS devices.

## CHAPTER 7

### CASE WESTERN RESERVE UNIVERSITY

#### 1. INTRODUCTION

This chapter summarizes the development, by the author and his coworkers at Case Western Reserve University, of two specimens for measuring the toughness of poly-Si films. This group's ultimate goal is to design and fabricate a robust electrostatically loaded test specimens that will allow on-chip testing of various mechanical properties of MEMS devices. The first design involved electrostatically loaded deeply cracked double cantilever beam specimens that failed to produce a force sufficient for fracture. This design is not being used anymore. However, in order to generate preliminary toughness data that could be used in the second design, these specimens were wedge-loaded to fracture by an external probe. The results, which will be summarized in the next section, appear in

[1] *R. Ballarini, R.L. Mullen, Y. Yin, H. Kahn, S. Stemmer and A.H. Heuer, "The fracture toughness of polycrystalline silicon microdevices: a first report," Journal of Materials Research, Vol. 12, No. 4, pp. 915-922, 1997.*

The second electrostatic actuator design was much more successful. It produced enough force to fracture films associated with a residual compressive stress, and produced enough displacement under resonance conditions to fracture those under a residual tensile stress. This work has been submitted for publication as

[2] *H. Kahn, R. Ballarini, R.L. Mullen and A.H. Heuer, "Electrostatically actuated failure of microfabricated polysilicon fracture mechanics specimens," submitted to Proceedings of the Royal Society of London, 1998.*

The geometry of this second device is currently being fine tuned to increase the force transmitted from the actuator to the fracture specimen, and to mitigate certain out-of-plane displacements that result from residual stresses.

Before proceeding with a summary of the above referenced papers, it is important to note that the polycrystalline silicon films tested in Reference [1] are not the same as those tested in Reference [2]. In Reference [1] the deposition temperature of the undoped films was higher, and resulted in a larger average grain size. Furthermore, in Reference [1] the doping was performed during the crystal growth, while in Reference [2] it was done afterwards.

#### 1. REFERENCE [1]

##### Summary

In this work the authors studied the fracture characteristics of relatively thick (up to 7.5  $\mu\text{m}$ ) poly-Si films fabricated using procedures identical to those used for current

MEMS devices. They developed a fracture specimen whose characteristic dimensions, notch tip radius, and uncracked ligament length are comparable to the grain size of the polysilicon, and present data on the critical value of the nominal  $J$ -integral for fracture initiation,  $J_c$ . Notwithstanding the inherent difficulties of microfracture mechanics experimentation, the values determined for  $J_c$  appear to be four times higher than those obtained using macro specimens of single crystal silicon.

### **Fabrication and characterization of microfracture specimens**

A typical microfracture specimen is shown in Figure 1a. The specimen is essentially a deeply cracked, double cantilever beam, suspended from an anchor through two thin beams. The authors' initial goal was to load the specimen electrostatically through the comb actuators. In fact, the generated force for this design was not sufficient to initiate crack propagation, and the fabricated specimens were loaded mechanically through a 10  $\mu\text{m}$  diameter probe inserted along the crack surfaces, as will be explained subsequently.

The fracture devices were fabricated by standard surface micromachining techniques, using a single-mask process. First, wafers underwent wet oxidation at 1100°C for 14 h, to grow a 2.5  $\mu\text{m}$  thick  $\text{SiO}_2$  release layer, which is visible in (the bottom of) Figures 1b and 1c. This was followed by the formation of the polysilicon films by CVD. The undoped films were grown at 610°C at a total pressure of 244 mTorr, using  $\text{SiH}_4$  gas; in all cases, a 2.5 or 5  $\mu\text{m}$  thick film was formed in one run, and for thicker films, a second deposition was performed after exposure to the laboratory ambient. The B-doped films were grown at 1100°C, using a combination of  $\text{SiCl}_3\text{H}$  and  $\text{B}_2\text{H}_6$  gases, following a brief nucleation step at 775°C in  $\text{SiH}_4$ ; the several thicknesses studied were each grown in a single deposition run, of course using different deposition times for the varying thicknesses. Because the surfaces of the as-deposited poly-Si films were very rough, some of the films were subjected to a chemo-mechanical polishing with a colloidal silica slurry (Syton), which converted the rough surface of the polysilicon films to a mirror finish. The polysilicon films were then oxidized to form a masking layer for a later polysilicon etch. This wet oxidation was carried out at 1000°C, for 100 to 300 min, depending on the desired final-masked oxide thickness.

The micromechanical structures were patterned using standard optical lithography techniques. The masking oxide layer was dry etched in  $\text{CHF}_3$ ,  $\text{C}_2\text{F}_6$ , and He, flowing at 20, 8, and 45 sccm, respectively, at 2.4 Torr and 350 W rf, and an etch rate of 300 nm/min. The polysilicon etch recipe contains an initial native oxide removal step, to remove any  $\text{SiO}_2$  on the surface. This etching was done for 40 s at 400 mTorr and 200W, with  $\text{SF}_6$ ,  $\text{Cl}_2$ , and He flow rates of 50, 80, and 120 sccm, respectively. The main portion of the etch was performed at 400 mTorr and 200 W, with  $\text{Cl}_2$  and He flow rates of 80 and 120 sccm, respectively, using an optical endpoint detector. The etch rate was 400 nm/min, and a 1 min overetch was included. Both etch steps were done at an anode-to-wafer gap spacing of 6 mm. The selectivity was 24:1 with respect to  $\text{SiO}_2$ . This etching sequence is quite successful in achieving smooth, nearly vertical sidewalls in the thick polysilicon films.

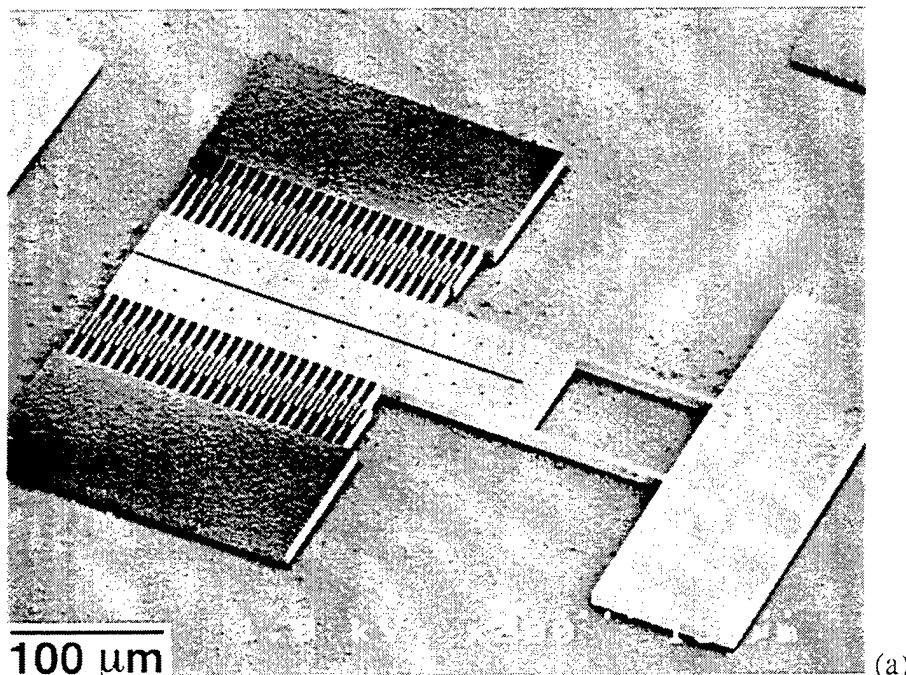
The final step was to release the structures in hydrofluoric acid, which removed the release oxide, as well as any remnant masking oxide. This etching step was done for 10

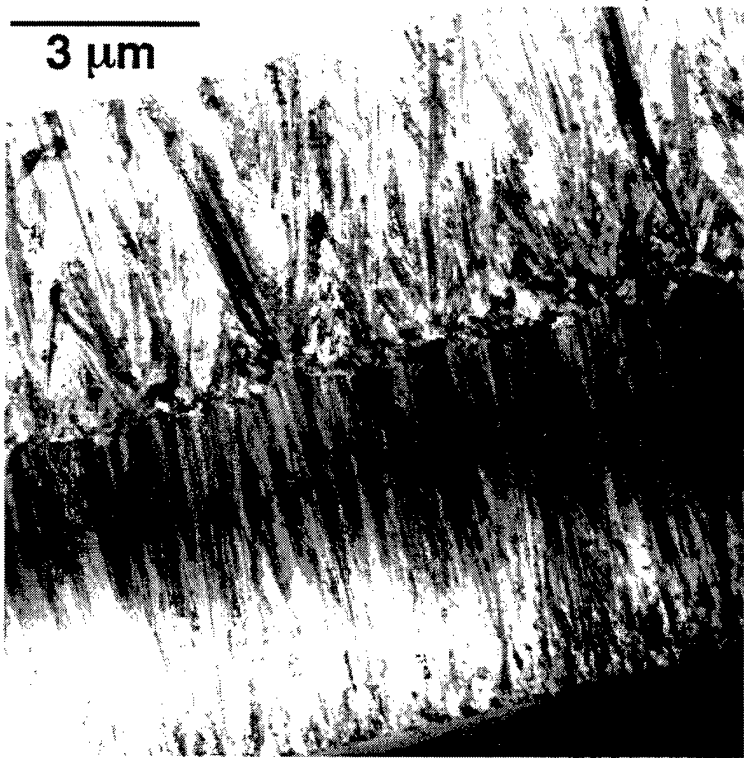
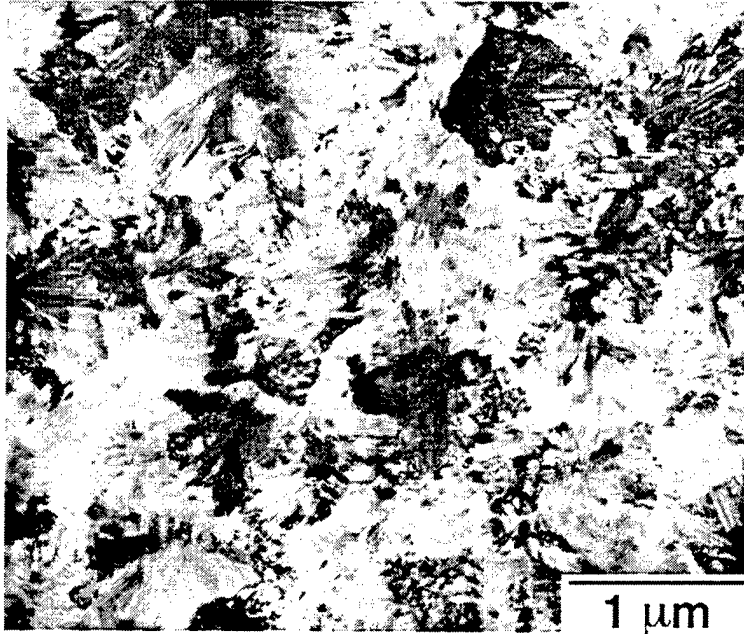
min, so that some oxide remains beneath the large features of the structures, leaving them anchored to the substrate, while the smaller features are fully released and free to move.

In both doped and undoped films, the individual grains have an average diameter of about  $0.5\ \mu\text{m}$  (Reference [1] reports  $1.0\ \mu\text{m}$ ), as seen in the cross-sectional TEM images and the planar view micrographs shown in Figures 1b and 1c; it is clear that the microstructure of the fabricated devices is nearly columnar.

Figure 1b shows the microstructure of a two-run film which exhibits a second nucleation layer of randomly oriented grains which formed at the beginning of the second run, most likely due to a thin native oxide on the surface of the first layer. The most striking feature of the microstructure is the density of vertically oriented  $\{111\}$  twin boundaries, which are known to be the major intragranular defect in CVD-grown polysilicon (*T.I. Kamins and T.R. Cass, Thin Solid Films, Vol. 16, pp. 147, 1973*). The columnar grains form by "evolutionary selection" (*A. van der Drift, Philips Res. Repts., Vol. 22, pp. 267, 1967*) and result in an overall  $\langle 110 \rangle$  texture, which was confirmed by x-ray pole figures. The boron-doped films (Figure 1c) were deposited at a higher temperature and exhibit a lower twin boundary density, but approximately the same average grain size as the undoped films (cf. Figures 1b and 1c). The lower twin boundary density in the doped films is thought to be due to the higher growth temperature.

Dislocations were also present in both the doped and undoped films, but the high density of twin boundaries prevented their systematic study. These dislocations may be associated with the residual compressive stresses present in as-deposited and oxidized films, which can be as high as 200 MPa (*H. Kahn, S. Stemmer, K. Nandakumar, A.H. Heuer, R.L. Mullen, R. Ballarini and M.A. Huff, "Mechanical properties of relatively thick, surface micromachined polysilicon films," 1996 Proceedings of the 9<sup>th</sup> IEEE International Workshop on Micro Electro Mechanical Systems, MEMS 96, pp. 343, San Diego, CA, 11-15 February 1996, New York: IEEE*).





(b)

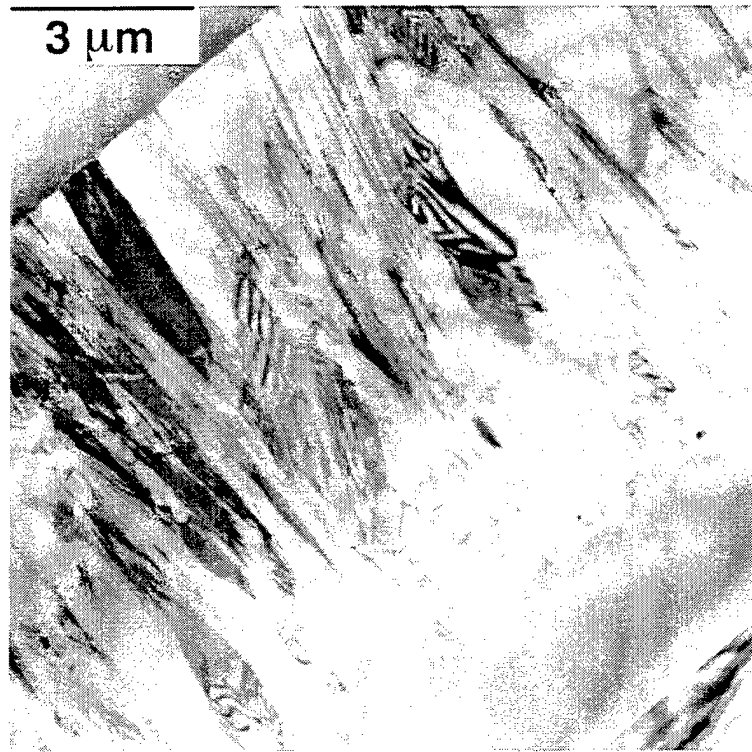
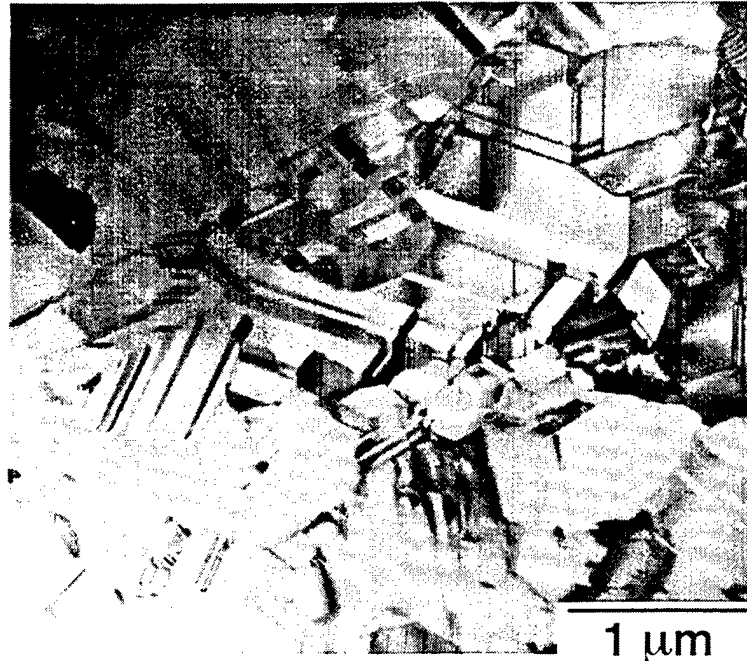
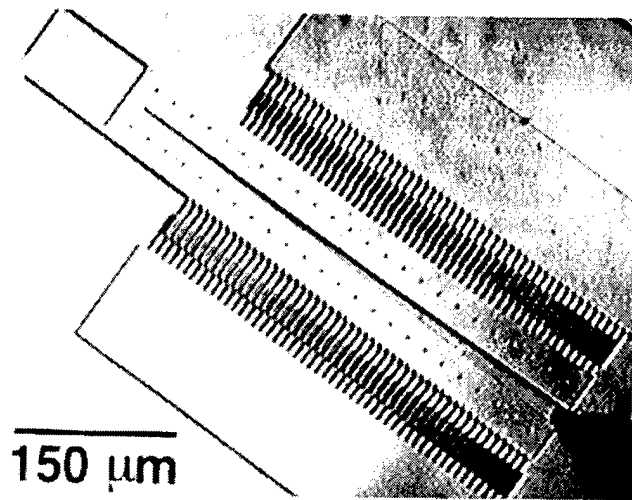
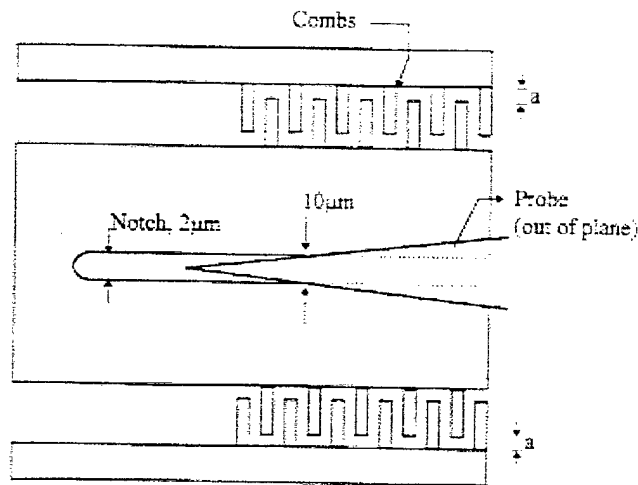


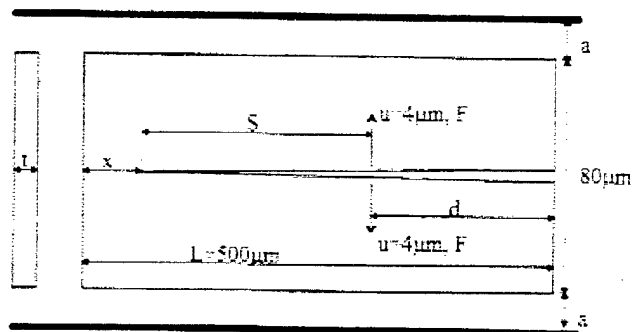
**Figure 1- Microstructure of polysilicon microfracture specimens: (a) shows a typical specimen; (b) shows, for an undoped CVD film, a planar view (top picture) micrograph of the grain and twin boundaries, and a cross-sectional TEM (bottom picture); (c) shows, for a boron doped CVD film, a planar view (top picture) micrograph of the grain structure, and a cross-sectional TEM (bottom picture) (Reference [1]).**



(a)



(b)



(c)

**Figure 2-** (a) Micrograph of wedge loaded microfracture specimen; (b) schematic drawing of microfracture specimen; (c) variables and nominal dimensions used in the mathematical model (Reference [1]).



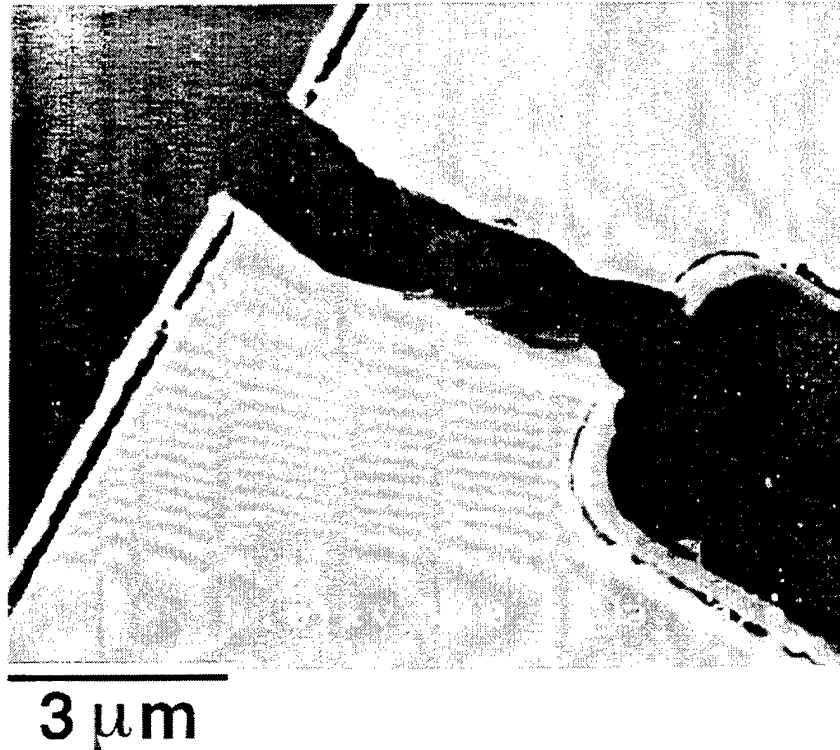


**Figure 3- SEM micrograph of a fractured 6  $\mu\text{m}$  ligament B-doped specimen. The crack path is almost entirely transgranular (Reference [1]).**

### **Test procedure**

A schematic drawing of the loaded fracture specimen is shown in Figure 2b, while the nominal dimensions are shown in Figure 2c. The thickness  $t$  of the specimen and the length  $x$  of the uncracked ligament were either 2.5, 5, 7.2 and 7.5  $\mu\text{m}$ , and 6, 10, and 20  $\mu\text{m}$ , respectively. The comb free-travel distance  $a$  was either 8 or 18  $\mu\text{m}$ . To cause failure of these microdevices, a rigid probe was used to wedge open the 2  $\mu\text{m}$  wide notch, as shown in Figure 2a. The shaft of the tungsten carbide probe is 0.020" in diameter and tapers to a conical point, with an inclusive angle of 15°, to a tip radius of 5  $\mu\text{m}$ . As the probe was moved toward the crack tip, its position at crack initiation was observed and recorded on video. This information in turn was used together with a finite element method analysis to determine  $J_c$ , a fracture parameter appropriate for these specimens because the radius of the notch ( $\sim 1 \mu\text{m}$ ) is comparable to the average diameter of the grains and other characteristic dimensions. A fractured sample is shown in Figure 3, and demonstrates that fracture is largely transgranular (this was typical of all specimens). The finite element calculation procedure for the J-integral, which assumed a Young's modulus equal to 160 GPa and a Poisson's ration equal to 0.22, is not presented here for brevity. The details can be recovered in Reference [1].

### **Results**

As shown in Table 1, the authors present the critical J-integral as a measure of the fracture resistance. They stated that the tests on the 2.5  $\mu\text{m}$  thick specimens were associated with significant out-of-plane deflections. Therefore the resulting unphysically high critical energy release rate values were discarded. The remaining values range from 16 to 62 N/m, exhibit a large scatter, and are approximately four times higher than those of single crystal silicon.

TABLE I. Critical energy release rate ( $\bar{J}_c$ ) data.

Thickness ( $\mu\text{m}$ )	Polysilicon			$\bar{J}_c$ (N/m)		
	Doped	Syton polished	Uncracked ligament length ( $\mu\text{m}$ )	Average	Standard deviation	Number of tests
2.5	Yes	Yes	6	134	48	5
2.5	Yes	Yes	10	126	27	6
2.5	Yes	Yes	20	747	412	6
5.0	Yes	Yes	6	53	22	7
5.0	Yes	Yes	10	62	20	8
5.0	Yes	Yes	20	58	8	6
7.5	Yes	Yes	6	38	16	5
7.5	Yes	Yes	10	19	4	6
7.5	Yes	Yes	20	16	8	5
5.0	No	No	6	26	4	4
5.0	No	No	10	24	8	4
5.0	No	No	20	28	14	6
7.2	No	Yes	6	25	11	3
7.2	No	Yes	10	24	4	3
7.2	No	Yes	20	26	6	4

Table 1- Critical energy release rate data (Reference [1]).

## 2. REFERENCE [2]

### Summary

The specimens described in this paper are fully integrated with simultaneously fabricated electrostatic actuators which are capable of providing sufficient force to ensure catastrophic crack propagation from notches produced using micromachining. Thus, the entire fracture experiment takes place on-chip, without the need of an external loading device. This is what makes this work unique from the others reviewed in this report. Fracture has been initiated using both monotonic and cyclic resonance loading. A reduction in the nominal toughness under cyclic loading is attributed to subcritical growth of a sharp crack from the micromachined notches. Fatigue fracture has also been observed in specimens subjected to as many as  $10^9$  cycles. Preliminary results suggest that subcritical crack growth can result from the applied loading (without the environment attacking the crack front).

The critical displacement of the electrostatic actuator at the instant of fracture is recorded, and subsequent finite element modeling is used to determine the stress intensity at the notch tip. Since the notch tip is quite blunt (the tip radius is 1  $\mu\text{m}$ ), the maximum principal stress and the critical value of the nominal J-integral for fracture initiation,  $J_c$ , are reported.

The actuation mechanism exploited to create the necessary far field force for fracture was electrostatic attraction in interdigitated comb structures. This mechanism is quite robust and is the basis of the widely-used accelerometers that comprise most current automotive air bag sensors. As illustrated in Figure 4a, when a voltage is applied between two sets of fingers, the capacitance,  $C$ , of the structure will increase as the movable fingers move a distance  $x$  and increase the finger-finger overlap. The force,  $F$ , generated by such electrostatic actuation is given by

$$F = \frac{1}{2} \frac{\partial C}{\partial x} V^2 = n\epsilon \frac{h}{g} V^2$$

(1)

where  $n$  is the number of fingers,  $\epsilon$  is the permittivity of the fluid between the fingers,  $h$  is the height of the fingers,  $g$  is the gap spacing between the fingers, and  $V$  is the applied voltage (W.C. Tang, T.-C.H. Nguyen and R.T. Howe, "Laterally driven polysilicon resonant microstructures," *Sensors and Actuators*, Vol. 20, pp. 25-32, 1989). Such electrostatic actuation usually involves only modest numbers of interdigitated combs. However, 400  $\mu$ N of actuation force has been realized in bulk micromachined single crystal silicon devices which contained 2000 pairs of interdigitated comb fingers (M.T.A. Saif and N.C. MacDonald, "A millinewton microloading device," *Sensors and Actuators*, A 52, pp. 65-75, 1996). The authors have now generated similarly large electrostatic forces in surface micromachined polysilicon devices.

## Experiment

### Device

The device used in this investigation is shown schematically in Figure 4b. The outer frame of the actuator is fully released from the substrate in the final stage of MEMS processing and is free to move when subjected to the electrostatic attraction of the comb drives. The frame is anchored to the substrate at the ends of eight long thin beams, which constrain movement in the vertical direction, but allow side-to-side movement. Two different devices were fabricated, containing either 1456 or 2040 pairs of comb fingers (rather than the 18 shown in Figure 4b), which pull the actuator to the left (in the orientation of Figure 4b) when a voltage is applied. This in turn pulls on the connecting beam and the top of the fracture mechanics microdevice, which is anchored to the substrate on the opposite side. This creates a stress concentration at the notch of the specimen, which

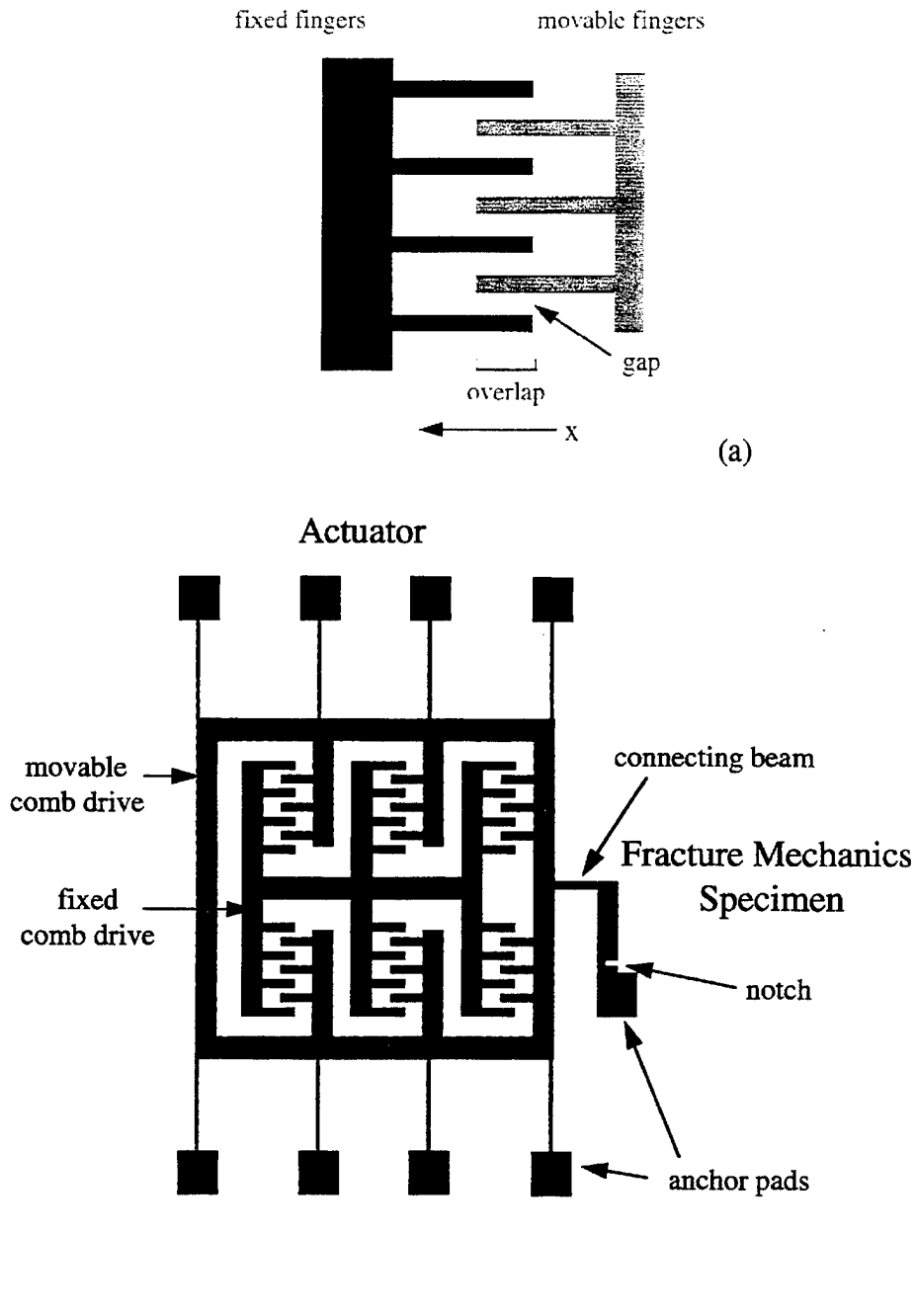


**Figure 4- (a) Sketch of two sets of interdigitated comb fingers; when a voltage is applied across this comb drive, the movable fingers will move to the left; (b) schematic drawing of the fracture device which consists of an actuator (in this sketch, the actuator has 18 pairs of comb fingers acting in parallel) and a fracture mechanics specimen (Reference [2]).**

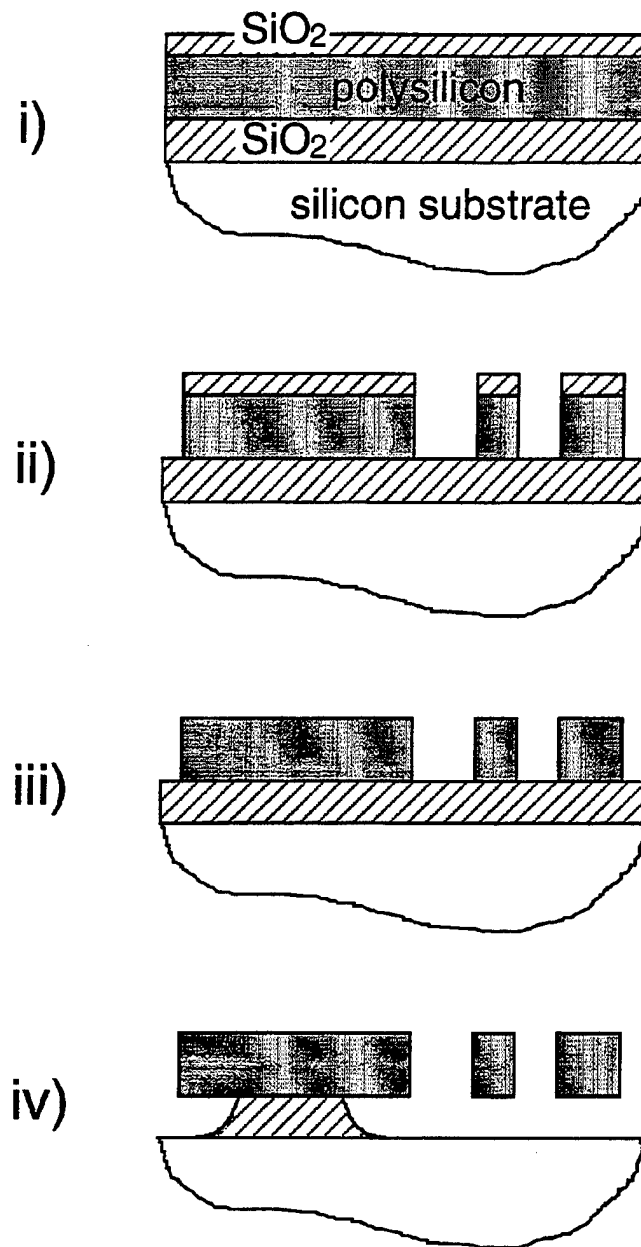


**Figure 5- Cross-sectional drawings depicting the device fabrication sequence: i) a thick  $\text{SiO}_2$  film is grown on a silicon substrate, followed by LPCVD deposition of a polysilicon film and a  $\text{SiO}_2$  film; ii) using photolithography, the device is patterned, and the top  $\text{SiO}_2$  and polysilicon films are sequentially etched; iii) the top  $\text{SiO}_2$  film is completely removed, and the polysilicon film is boron-doped; iv) the device is time-released in hydrofluoric acid, such that some  $\text{SiO}_2$  remains beneath the large anchor pads, while the smaller features are fully released and free to move (Reference [2]).**

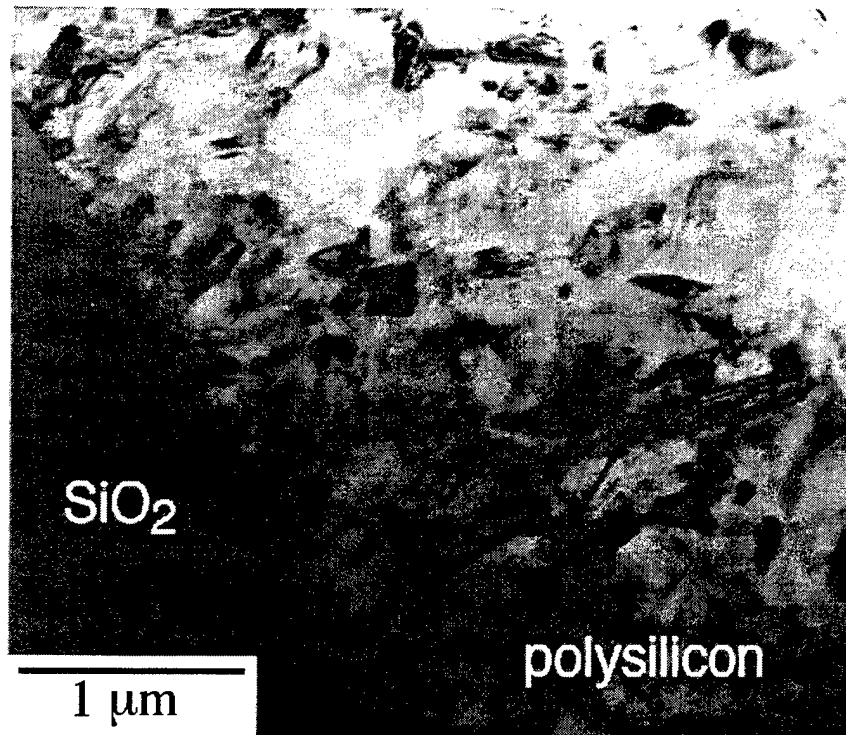


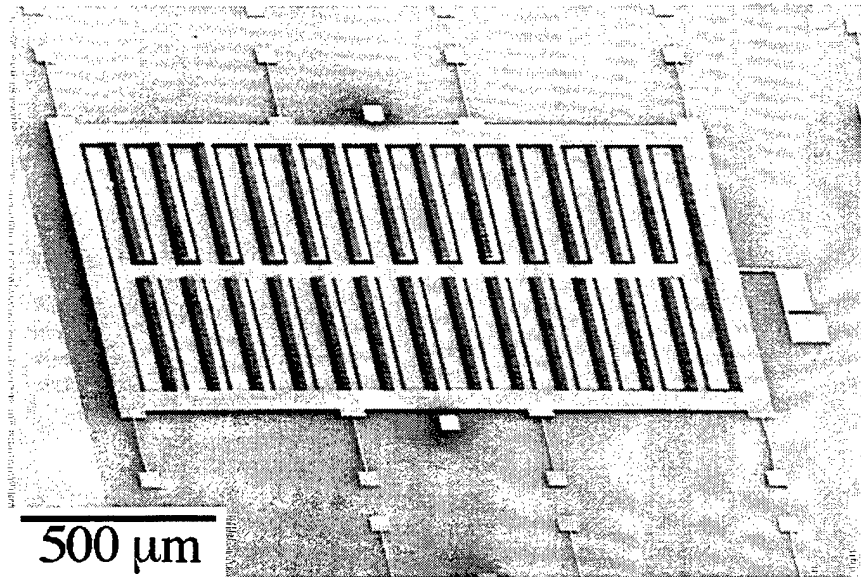
**Figure 6- Transmission electron micrograph showing the microstructure of the polysilicon (Reference [2]).**

mimics a conventional single edge-notch fracture mechanics specimen. When the displacement reaches a critical value, the mechanical forces become sufficiently high to initiate fracture.

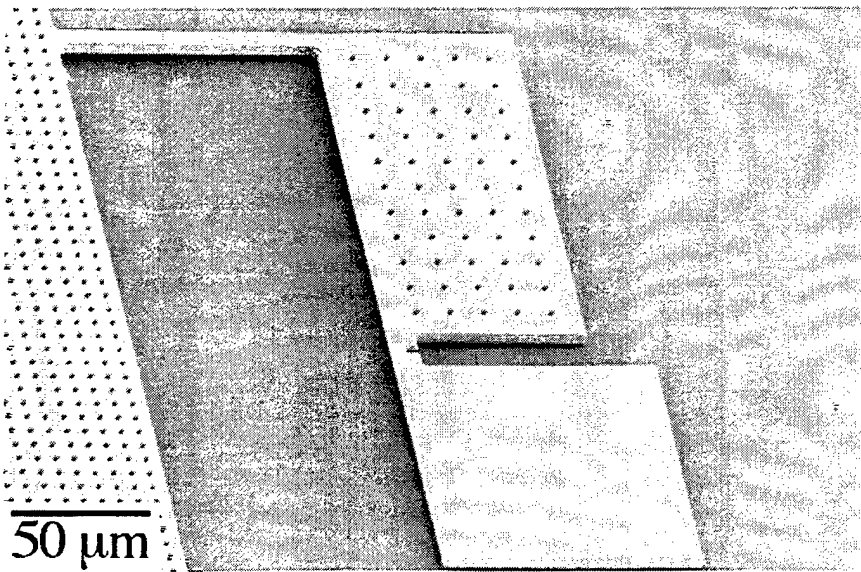
### ***Fabrication***

The test specimens were fabricated using standard surface micromachining techniques and a one-mask process, illustrated in Figure 5 and summarized as follows. (100) silicon wafer substrates are oxidized to a thickness of 2.5 μm, the oxide serving as a release layer. A 5.2 μm thick film of polysilicon is deposited by low pressure chemical vapor deposition (LPCVD) at 580°C using SiH<sub>4</sub> gas. The as-deposited film is at least partially amorphous (*G. Harbeke, L. Krausbauer, E.F. Steigmeier, A.E. Widmer, H.F. Kappert and G. Neugebauer, J. Electrochem Soc., Vol. 131, pp. 675, 1984*), and is annealed at 1100°C, during which crystallization to a fine-grained polycrystalline microstructure occurs; the microstructure is shown in the transmission electron micrograph in Figure 6. A 0.5 μm film of SiO<sub>2</sub> is then deposited by LPCVD at 450°C using SiH<sub>4</sub> and O<sub>2</sub> gases for use as a masking oxide. Standard photolithography is then used to pattern the devices in photoresist. Subsequently, the masking oxide is dry etched in a CHF<sub>3</sub>/C<sub>2</sub>F<sub>6</sub> plasma, followed by dry etching of the polysilicon in a Cl<sub>2</sub> plasma. The remaining masking oxide is chemically removed using HF, and the polysilicon is boron-doped in a diffusion furnace at 1000°C. (Such boron-doped polysilicon specimens have a resistivity of 3x10<sup>-3</sup> ohm-cm.) The devices are then released by immersion in aqueous

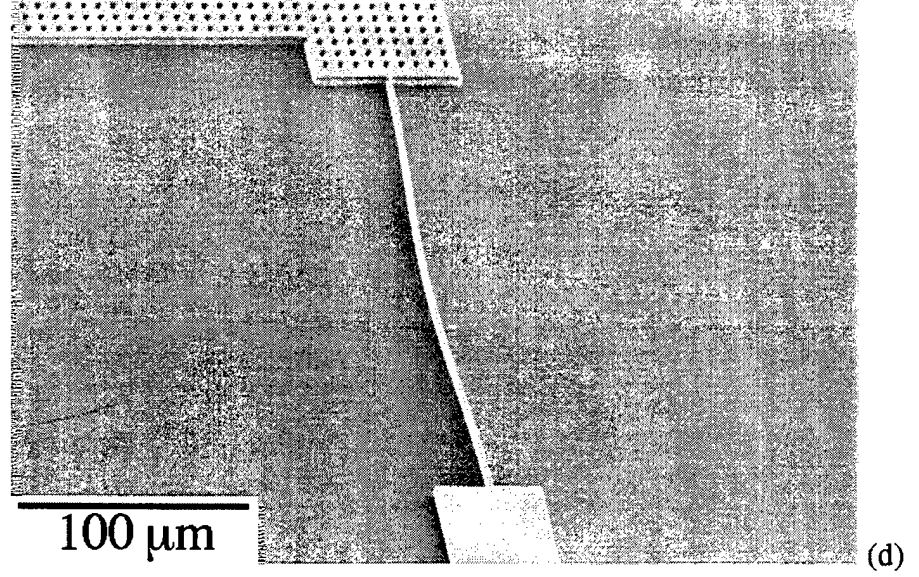
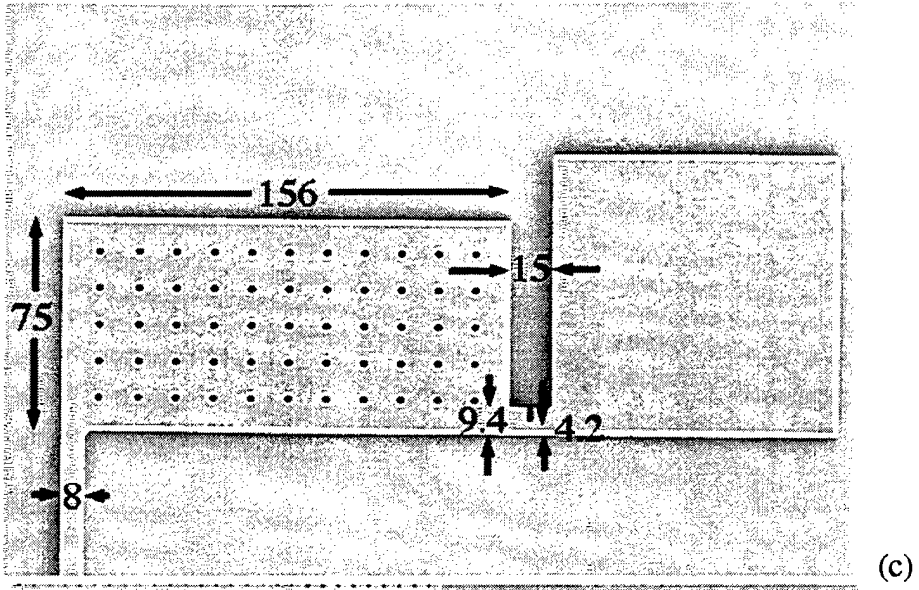
hydrofluoric acid (HF) to dissolve some of the SiO<sub>2</sub> for a specific time, such that some oxide remains beneath the anchor pads leaving them attached to the substrate, while the movable portions of the device are fully released. Following HF release, the devices are placed in a 25% NH<sub>4</sub>F solution before rinsing, to help prevent stiction of the moving parts to the substrate. Stiction refers to the immobilization of a micromachined specimen during release. The NH<sub>4</sub>F treatment was suggested by Houston *et al.* (*M.R. Houston, R. Maboudian and R.T. Howe, Proceedings of the 8<sup>th</sup> IEEE International Conference on Solid-State Sensors and Actuators and Eurosensors IX, Transducers 95, pp. 210, Stockholm, 25-29 June 1995, New York: IEEE, also appears in J. Appl. Phys., Vol. 81, No. 8, pp. 3474-3483, 1997*).



(a)



(b)





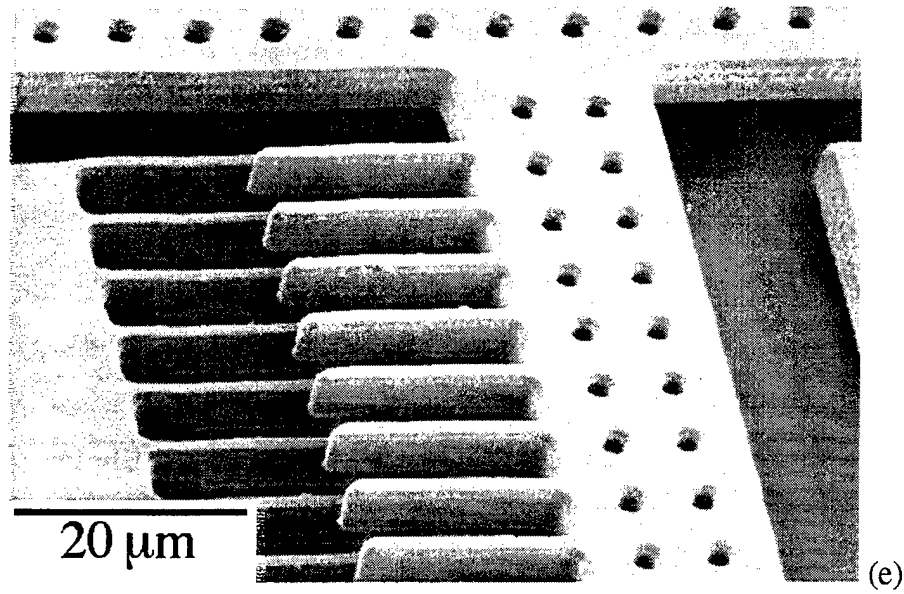


**Figure 7- (a) SEM image of the entire fracture device (viewed at a 45° angle); (b) a close-up of the fracture mechanics specimen; (c) a top view of the fracture mechanics specimen (rotated 90°) showing the dimensions (in μm); (d) one of the device's long support beams, buckled as-fabricated due to compressive residual stresses; (e) a high-magnification image showing several of the comb fingers; the fixed and movable combs are not co-planar (Reference [2]).**

A scanning electron micrograph (SEM) of a fabricated device, along with magnified views of the fracture mechanics specimen are shown in Figures 7a-c. (The dimensions of the particular fracture mechanics specimen shown in Figure 7c are also listed in Table 2 as fracture mechanics specimen A.) The 1456 pairs of comb fingers, situated in 14 rows, are 2 μm wide, 20 μm long, and are too small to be distinguished in the SEM image. The "release holes" visible in the upper portion of the fracture specimen and the outer frame of the actuator allow the HF etchant to flow beneath these areas during release. The boron-doped polysilicon contains a residual compressive stress of  $32 \pm 5$  MPa. When the device is released, these residual stresses cause the anchored support beams to buckle slightly, as seen in Figure 7d. In addition, the movable portion of the actuators are deflected out-of-plane by these residual stresses, as seen in Figure 7e. Both of these geometric changes in the device structure disappear during testing, as described below. The residual stresses were measured using passive micro-strain gauges which were simultaneously fabricated on the same wafers (*Kahn, H., Stemmer, S., Nandakumar, K., Heuer, A.H., Mullen, R.L., Ballarini, R. & Huff, M.A. 1996 Mechanical properties of thick, surface micromachined polysilicon films. In Proc. IEEE Int. Workshop on Micro Electro Mechanical Systems, MEMS 96, 11-15 Feb 1996, San Diego, CA, pp. 343-348. New York: IEEE.*)

**Table 2- Fracture mechanics specimen dimensions. Specimen A is shown in Figure 7c. All dimensions are in microns (Reference [2]).**

fracture mechanics specimen	doped	notch width	tip radius	uncracked ligament length	reduced beam		release end	
					width	length	width	length
A	yes	2	1	4.2	9.4	15	75	156
B	no	2	1	4.5	10	15	75	156
C	no	2	1	3	7	15	40	100

### ***Experimental procedure***

The fracture test is conducted by applying a dc voltage between the fixed and movable sets of comb fingers. This was done on a probe station, with one probe in contact with the central fixed portion of the device, and a second probe in contact with one of the outer anchor pads. A third probe was positioned in contact with the silicon substrate. This last probe was shorted to the probe on the anchor pad, and both were grounded. At the start of each test, the applied voltage had to be increased to a certain level (~ 40 V) before the movable portion of the actuator would be pulled flat (to counteract the processing-induced residual stresses), so that the movable fingers were nearly in-plane with the fixed fingers (to within approximately 1  $\mu\text{m}$ , the resolution of the focusing stage of the optical microscope attached to the probe station). After that point, as the voltage was increased, the actuator (and thus the released side of the fracture specimen) moved by increasing amounts until a crack emanated from the micromachined notch and fracture ensued. At this time, the fingers immediately moved into contact with each other, shorting the device and causing some melting of the polysilicon. During the test, the displacement of the actuator was recorded visually, with an accuracy of  $\pm 0.3 \mu\text{m}$ .

Devices were also fabricated from poly-Si films which were not boron-doped, but were otherwise processed identically. For these devices, the geometry of the fracture specimens (fracture mechanics specimen B in Table 2) was essentially identical to the doped devices, except that the reduced beam width was 10  $\mu\text{m}$  and the uncracked ligament length was 4.5  $\mu\text{m}$ . To achieve sufficient conductivity to allow electrostatic actuation, these devices were sputter-coated with ~10 nm of palladium following release. The residual stresses in these devices were smaller,  $19 \pm 5 \text{ MPa}$ , and tensile. This increased the stiffness of the actuator support beams to such an extent that sufficient displacement of the actuator to cause fracture could not be attained. (The force limitation in these specimens arose from the actuation voltage causing the outer frame of the actuator to bend, moving the comb fingers sideways, and shorting the device.) However, because of the tensile residual stress, the support beams were not buckled, and the application of an ac signal, at the proper frequency (~20 kHz), caused the device to resonate. While in resonance, a sufficiently high amplitude displacement could be achieved with a relatively low voltage to cause catastrophic crack propagation and fracture of the specimen. To investigate the effects of the laboratory ambient, in particular the relative humidity, on fatigue behavior, some resonance tests were performed in a vacuum chamber which was evacuated to a pressure of 8 Pa.

Though these devices could not be fractured with a dc signal, monotonic fracture could still be accomplished by mechanically pushing the actuator with a probe, as in Reference [1]. The probe was carefully manipulated to ensure strictly lateral stresses; though for this experiment, the possibility of perpendicular and out-of-plane stresses could not be eliminated. For completeness, boron-doped devices were also tested with the mechanical probe technique, and the results included here.

## Modeling

After determining the displacement at which fracture occurred, the device behavior under electrostatic loading was thoroughly modeled using finite element analysis (FEA) in order to determine the relationship between the observed displacement at fracture and the maximum tensile stresses,  $\sigma_{\max}$ , as well as the critical energy release rates,  $J_c$ . The finite element model included both the fracture mechanics specimen and the actuator. The geometry of the fracture specimen was determined from measured values while the dimensions of the actuator were taken from nominal design values. The model was constructed from approximately 16,000 eight-node plane stress quadrilateral elements. The mesh density was determined by a study of the convergence of the strain energy with number of elements. For all analyses, Young's modulus and Poisson's ratio of polysilicon were assumed to be 168 GPa and 0.22, respectively, and a large strain formulation was used. Experimentally measured residual stresses were included. Figures 8 and 9 present typical results of the finite element calculations. Figure 8 shows the magnified displacements of both the actuator and specimen for a 600  $\mu\text{N}$  load on a boron-doped device. The effect of residual stress on the upper right support beam can be seen in the displaced shape. In addition, the moment generated in the fracture specimen results in a small rotation of the actuator. Figure 9a shows the discretization of the specimen geometry and the contours of displacement magnitude. Contours of maximum tensile stress in the region surrounding the notch tip are shown in Figure 9b. The residual stress (the stiffness of the support beams) has a significant impact on the actuator behavior; however,  $\sigma_{\max}$  in the fracture specimens was independent of residual stress for actuator displacements resulting in fracture. For example, at a 7  $\mu\text{m}$  displacement of the end of the fracture specimen,  $\sigma_{\max}$  was calculated to be 4.07 MPa in a linear analysis without residual stress and 4.09 MPa using large strain and residual stresses. Reported stress and energy release values presented are calculated from nonlinear finite element results. Linear calibrations can be used with less than a 5 percent difference from the non-linear calculation. For the boron-doped devices, the linear calibrations indicated that  $J_c=1.27 \delta^2$  and  $\sigma_{\max}=0.58 \delta$ , where  $\delta$  is the displacement of the end of the fracture mechanics specimen in  $\mu\text{m}$ ,  $J_c$  is in N/m, and  $\sigma_{\max}$  is in GPa. For the undoped devices,  $J_c=1.38 \delta^2$  and  $\sigma_{\max}=0.61 \delta$ . Since displacement was experimentally measured at a specific point on the actuator, FEA modeling was also used to correlate that measurement to the displacement of the specimen.

The FEA modeling also determined that the electrostatic actuator generated 90 percent of its theoretical force, as calculated by equation (1). Most likely, the modest loss in force is due to the fixed and movable fingers not being exactly co-planar during the experiment and to the slight rotation of the actuator.

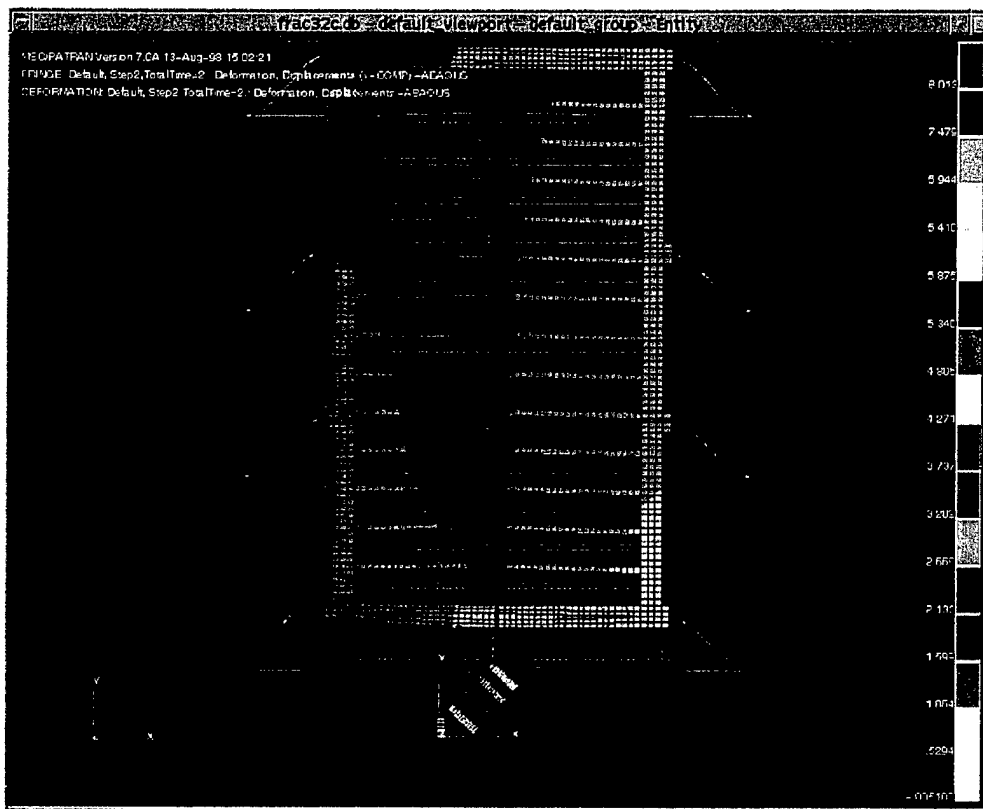


**Figure 8- Finite element calculations showing displacements of a boron-doped device under a 600  $\mu\text{N}$  electrostatic load. The sketch greatly exaggerates the displacements; the original position of the device is outlined in blue (Reference [2]).**

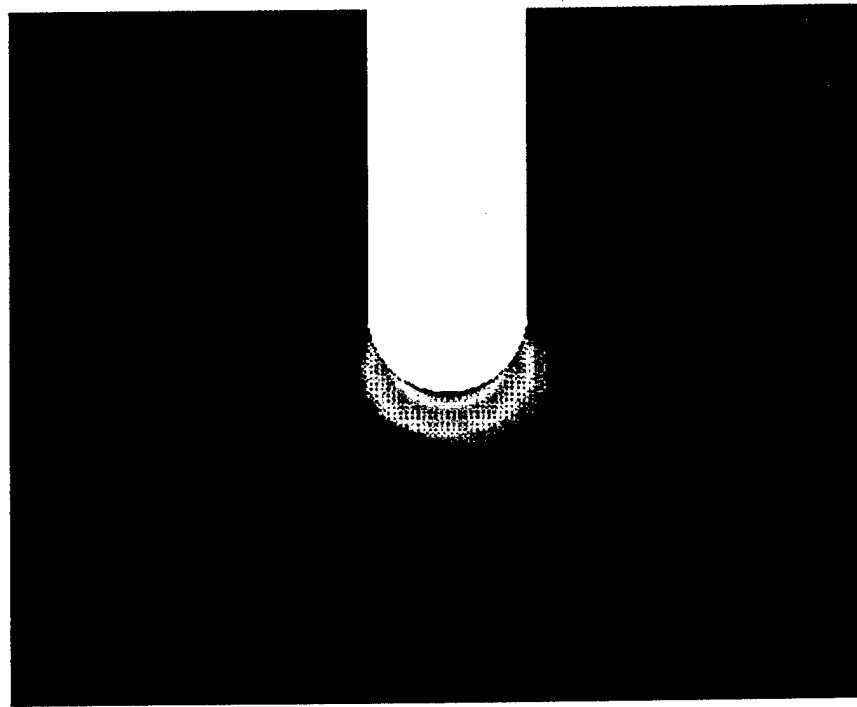
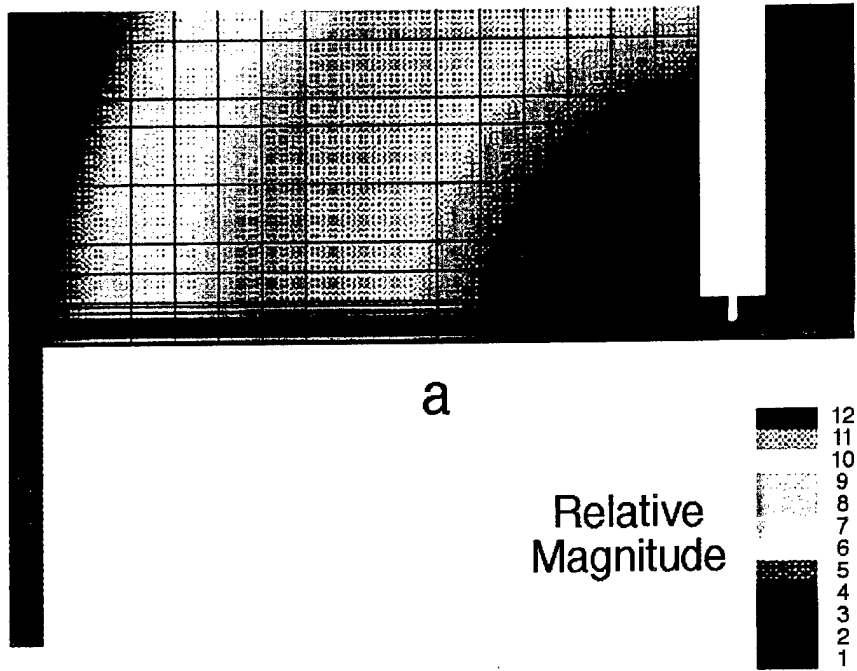


**Figure 9- Finite element calculations showing (a) the discretization of the specimen geometry and the contours of displacement magnitude and (b) the contours of maximum tensile stress in the region surrounding the notch tip (Reference [2]).**

## Experimental results and discussion

### Monotonic and cyclic fracture

The deflection of a typical sample during monotonic dc loading is shown in Figure 10. The specimen fractured at a displacement of  $8.3 \mu\text{m}$ . The movement of the actuator increased linearly with the square of the applied voltage, as expected from the electrostatic force equation (1).

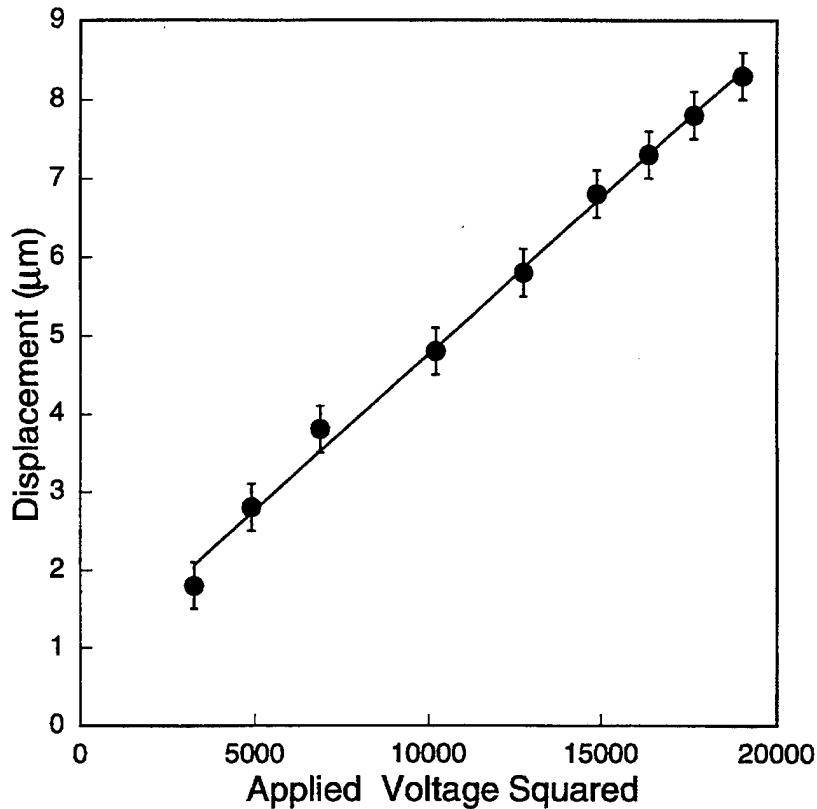


**Figure 10-** The displacement of the fracture device versus the square of the applied voltage; the device fractured at  $8.3 \mu\text{m}$  (Reference [2]).

The displacements at the point of fracture, along with the calculated  $J_c$  and  $\sigma_{\text{max}}$  values, for the five sets of experiments are shown in Table 3. The results for the two different techniques of monotonically loading the boron-doped samples (dc electrostatic actuation and pushing with a probe) are very consistent. This suggests that the two techniques are equivalent.

**Table 3- Experimental polysilicon fracture data (Reference [2]).**

	displacement at fracture ( $\mu\text{m}$ )	$J_c$ (N/m)	$\sigma_{\text{max}}$ (GPa)
B-doped polysilicon  monotonically (dc electrostatically) loaded (specimen A)	5.0*	31	2.9
	6.3	50	3.6
	7.1	64	4.1
	7.3*	67	4.2
	7.8	77	4.5
	8.3	87	4.8
	<b>average</b>	<b>7.0</b>	<b>63</b>
<b>standard deviation</b>	<b>1.2</b>	<b>20</b>	<b>0.7</b>
B-doped polysilicon  monotonically (pushed with probe) loaded  (specimen A)	5.5*	38	3.2
	6.0*	46	3.5
	6.8*	58	3.9
	6.8*	58	3.9
	6.8*	58	3.9
	7.2*	67	4.2
	7.3	67	4.2
	7.3	67	4.2
	7.3	67	4.2
	7.4*	70	4.3
	7.9*	79	4.6
	8.0	81	4.6
	8.5	92	4.9
	<b>average</b>	<b>7.1</b>	<b>65</b>
<b>standard deviation</b>	<b>0.8</b>	<b>14</b>	<b>0.5</b>
undoped polysilicon  monotonically (pushed with probe) loaded  (specimen B)	7.4*	76	4.5
	7.4	76	4.5
	7.6	80	4.6
	7.9	87	4.8
	7.9	87	4.8
	8.2*	94	5.0
	9.0	111	5.5
	9.0	111	5.5
<b>average</b>	<b>8.1</b>	<b>90</b>	<b>4.9</b>
<b>standard deviation</b>	<b>0.6</b>	<b>14</b>	<b>0.4</b>
undoped polysilicon  cyclically loaded (at atmospheric pressure)	4.6	29	2.8
	4.6	29	2.8
	4.9	33	3.0
	5.0	35	3.1
	5.3	39	3.2
	5.3	39	3.2

(specimen B)	6.0	50	3.7
	6.6	60	4.0
<b>average</b>	<b>5.3</b>	<b>39</b>	<b>3.2</b>
<b>standard deviation</b>	<b>0.7</b>	<b>11</b>	<b>0.4</b>
undoped polysilicon	4.4	26	2.7
	5.3*	39	3.2
cyclically loaded	5.3*	39	3.2
	6.5*	58	4.0
(at low pressure)	7.2	72	4.4
(specimen B)	8.7	105	5.3
<b>average</b>	<b>6.2</b>	<b>63</b>	<b>4.0</b>
<b>standard deviation</b>	<b>1.6</b>	<b>27</b>	<b>0.9</b>

\*These devices contained actuators with 2040 comb fingers; all other devices had actuators with 1456 comb fingers.

The  $J_c$  values obtained for the monotonically loaded boron-doped and undoped poly-Si devices are comparable to, and consistent with previously reported values for specimens with similar blunt notches (Reference [1]). The small differences between the boron-doped and undoped samples are within the scatter of the data; therefore, any doping effects on toughness must be small or nonexistent. The doping procedure also induces some changes in the surface morphology of the poly-Si devices. Because a small amount of oxidation occurs, followed by the removal of this oxide during the release process, any sharp features will be somewhat rounded. In addition, during the doping, thermal grooving occurs where the grain boundaries intersect the free surface. Both of these features can be seen in the micrographs presented in Figure 12.

For the undoped devices, the  $J_c$  values derived under cyclic stress are lower than under monotonic loading. This suggests that during resonance a sharp fatigue crack grows subcritically to a critical dimension. (During the resonance experiment, the specimens were subjected to the critical displacement amplitudes for approximately 0.1 to 5 seconds before fracture, corresponding to 2000 to 100000 cycles. This is referred to as "fast fracture.") Additional specimens were set into resonance at displacements which were too low to initiate fast fracture. The specimens were allowed to continue resonating until fracture occurred. The results, including those from the fast fracture and monotonic experiments, are plotted in Figure 11 as the maximum tensile stress generated at the notch,  $\sigma_{max}$ , versus the number of cycles required for fracture; in essence, this is a traditional S-N (stress to failure versus number of cycles to failure) fatigue curve. All of these tests were carried out in a laboratory ambient - approximately 23°C and 40 percent relative humidity. The results represented by circles were obtained using the fracture mechanics specimen described above. The results represented by triangles were obtained using a fracture mechanics specimen with the same shape but different dimensions - these specimens are listed as geometry C in Table 2. The notch width and tip radius were identical in both specimens. Both specimens were modeled using FEA to determine  $\sigma_{max}$  as a function of displacement, and therefore all the results are included in the same plot.



Figure 11 illustrates that a large scatter exists in the data, possibly due to differences in the roughness of the inside notch surface caused by dry etching, and that fatigue fracture can be achieved at sub-critical stresses after as many as  $10^9$  cycles.

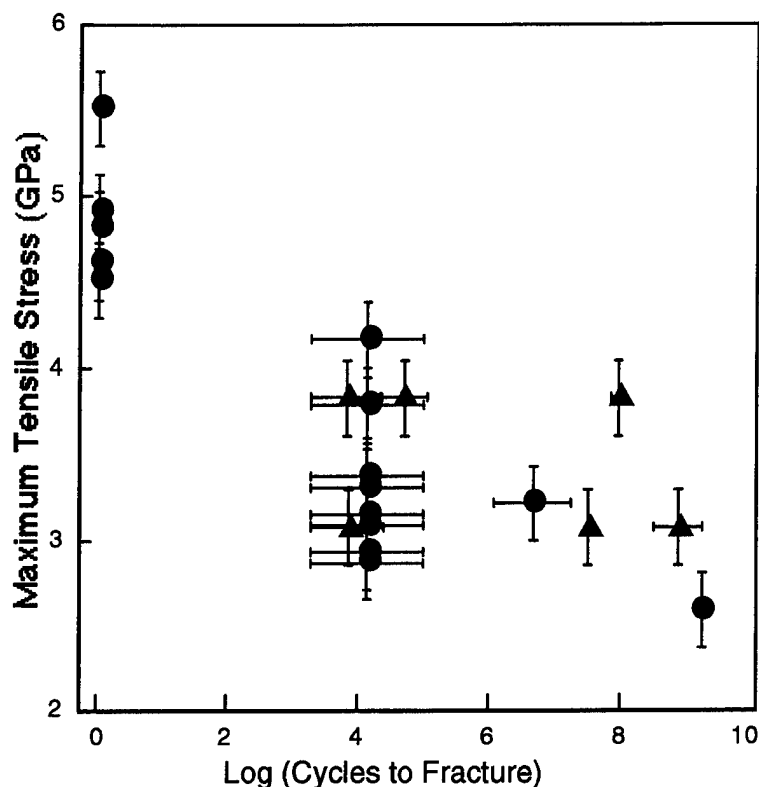


Figure 11- S-N (stress to failure versus number of cycles to failure) curve for fatigue fracture. See text for further details (Reference [2]).

For cyclic loading at low pressures, the  $J_c$  values obtained are higher than for cyclic loading in air, but are lower than for monotonic loading. This suggests that fatigue crack initiation and growth occurs during cyclic loading in both environments, but the process is faster in air, presumably due to stress corrosion in the presence of humidity. In the low pressure ambient, stress corrosion at crack tips will be less severe, but mechanical damage can still occur during the tensile-compression fatigue cycles. This phenomenon was reported by Suresh (*S. Suresh, Fatigue of Materials, Cambridge University Press, New York, 1991*) for zero stress-compression fatigue cycles.

### Fractography

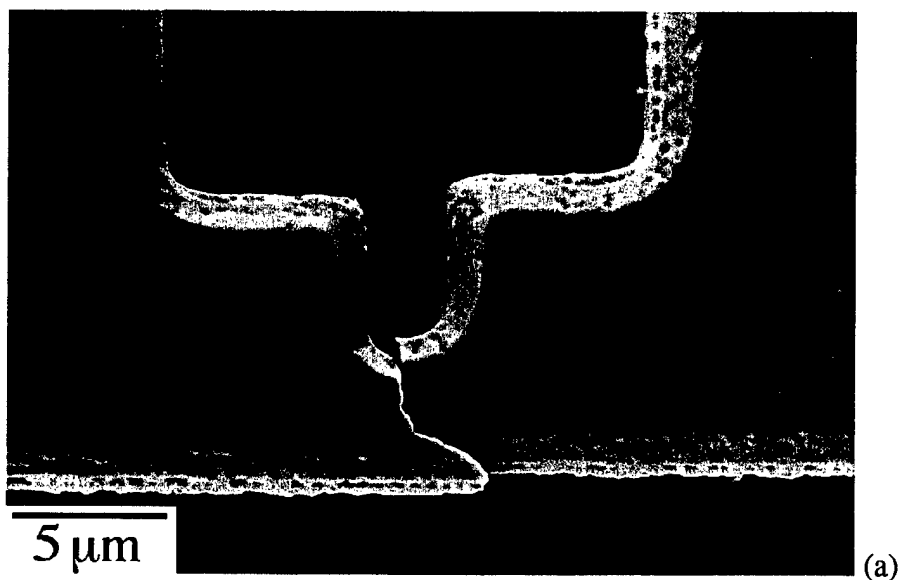
Figure 12a shows the top view of a fractured specimen. The crack path is significantly deflected; this was observed in most specimens. The fracture surface from a B-doped specimen, which fractured under monotonic loading at a deflection of  $7.9 \mu\text{m}$ , is shown in Figures 12b and 12c, and from an undoped specimen, which fractured under cyclic loading at a deflection of  $5.3 \mu\text{m}$ , in Figures 12d and 12e. (These were the two best examples of "classical" fracture features which were observed.) In both samples, a semi-

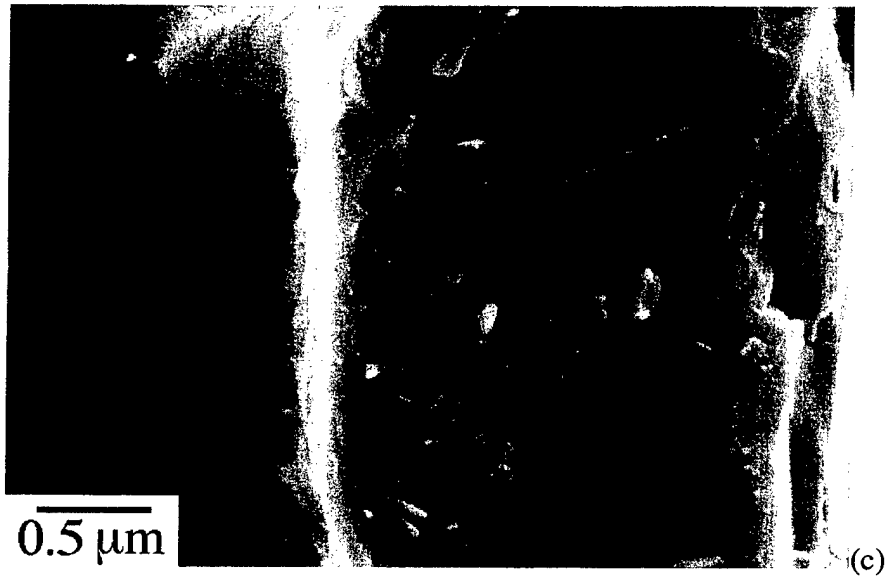
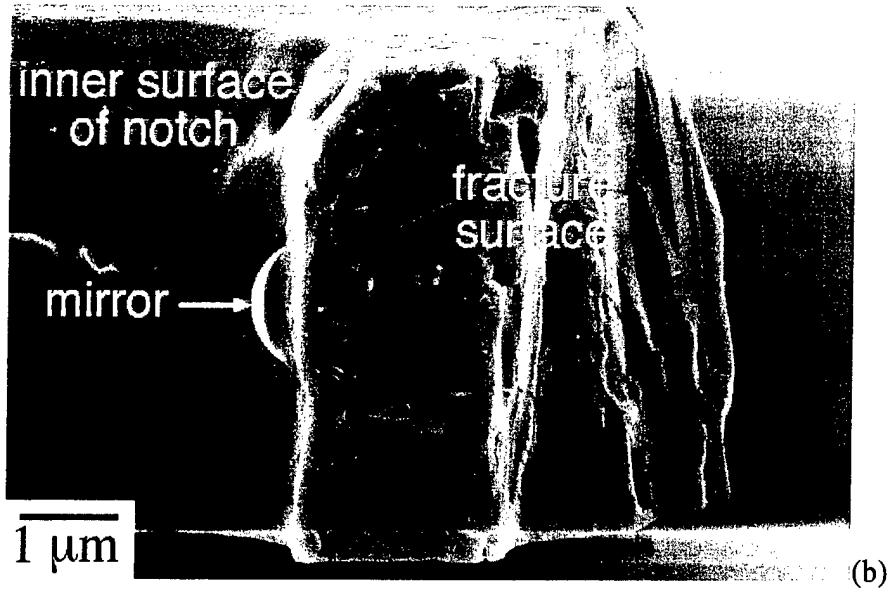
circular “mirror” is present, characteristic of brittle fracture, and surrounds the crack-initiating flaw. Beyond the relatively smooth mirror zone, branching cracks can be seen radiating from the crack initiation site. In brittle ceramics, the radius of the mirror is known to be 6 to 10 times the radius of the original flaw (*J.J. Mecholsky, Quantitative fractographic analysis of fracture origins in glass, in Fractography of Glass (ed. R.C. Bradt & R.E. Tressler), pp. 37-73. New York: Plenum Press, 1994*). For a semi-circular flaw, the stress intensity factor is given by

$$K = 1.25S\sqrt{a} \quad (2)$$

where  $S$  is the nominal stress, and  $a$  is the flaw radius (*Mecholsky, 1994*). Using the values of  $\sigma_{\max}$  from Table 2 for  $S$ , this corresponds to a fracture toughness,  $K_{Ic}$ , of 2.1 to 2.7  $\text{MPa}\cdot\text{m}^{1/2}$  for boron-doped polysilicon and 1.1 to 1.4  $\text{MPa}\cdot\text{m}^{1/2}$  for undoped polysilicon, using  $a$  values of 0.13 to 0.22  $\mu\text{m}$  and 0.07 to 0.12  $\mu\text{m}$ , respectively. It should be emphasized that this analysis is valid only for perfectly semi-circular flaws which lie perpendicular to the stress axis - a fact that could not be determined in this experiment. Therefore the differences seen between the doped and undoped polysilicon  $K_{Ic}$  values may not be significant.

These values are still higher than values previously reported for single crystal silicon ( $\sim 0.9 \text{MPa}\cdot\text{m}^{1/2}$ ). The higher fracture toughness of polysilicon compared to single crystal silicon suggests the existence of a “microstructural” toughening in our fine-grained polycrystalline samples. Current research is now being devoted to producing microfabricated fracture mechanics specimens containing atomically sharp cracks to study this phenomenon and other aspects of the fatigue of polysilicon (effects of humidity, temperature, etc.).





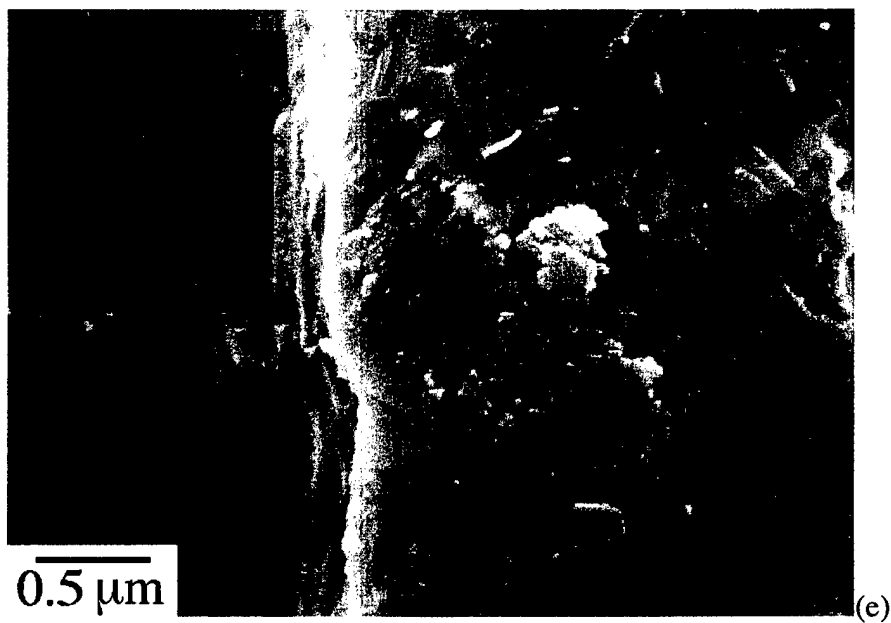
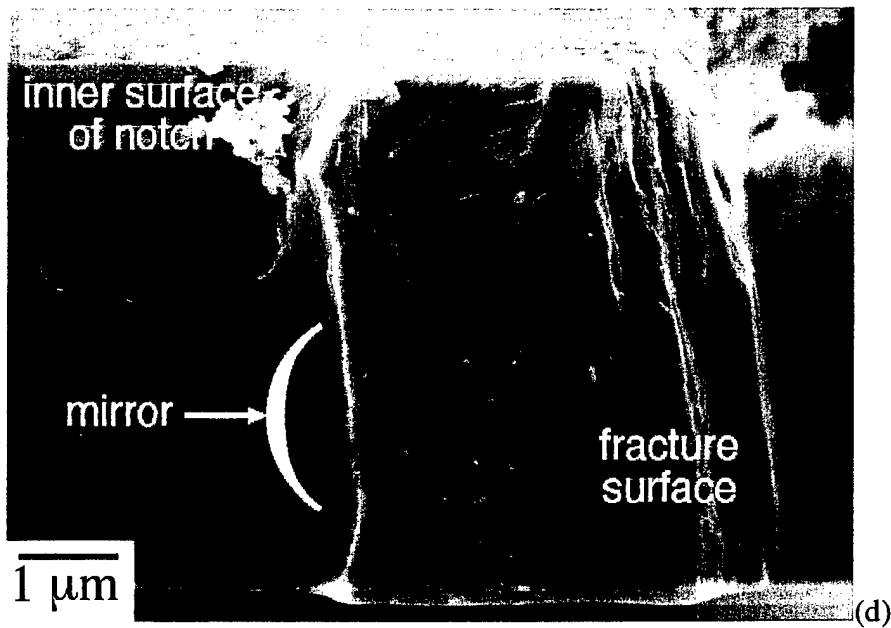


**Figure 12- a) SEM image of a fractured specimen, top view; b) the fracture surface of a doped specimen; c) higher magnification image of the area surrounding the crack initiation site; d) the fracture surface of an undoped specimen; e) higher magnification (Reference [2]).**

### **3. CRITIQUE**

The electrostatically actuated fracture specimen described in this chapter is the only system available for loading a thin poly-Si to fracture without an external loading device. Thus represents a step towards the development of on-chip test structures for measuring the in-situ mechanical properties of MEMS.

## CHAPTER 8

### CORNELL UNIVERSITY AND UNIVERSITY OF ILLINOIS AT URBANA- CHAMPAIGN

This chapter presents a very brief review of a recent paper by M.T.A. Saif and N.C. MacDonald that describes their development of a load calibration device, and its use as part of an on-chip strength measurement device that integrates the (electrostatic) actuator, the material sample, and the calibration mechanism. Their system relies on the knowledge of the elastic modulus of the calibration beam described next; thus it was used to measure the strength of single crystal silicon. While it cannot be directly applied to poly-Si, it is included in this report because it (1) reinforces the scientist's philosophy of on-chip test structures, and (2) illustrates the clever procedures that are continuously being developed by the MEMS community. The paper appeared as

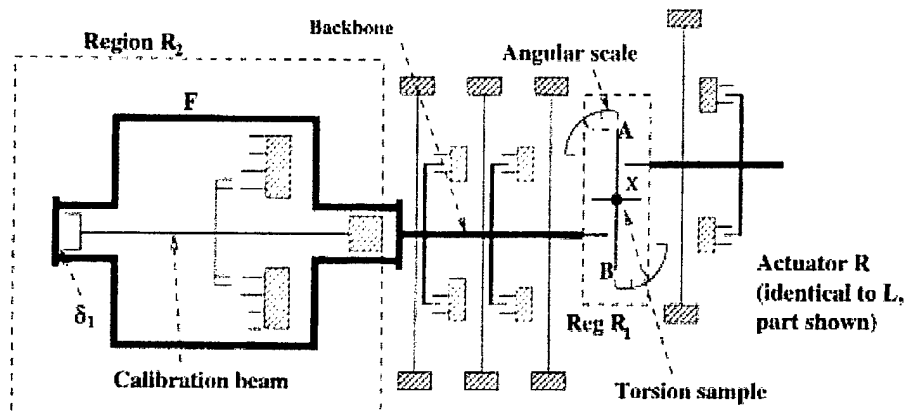
[1] *M.T.A. Saif and N.C. MacDonald, "Measurement of forces and spring constants of microinstruments," Review of Scientific Instruments, Vol. 69, No. 3, pp. 1410-1422, March 1998.*

A schematic and an SEM micrograph of the left side and part of the right side of the integrated microinstrument are shown in Figure 1. The torsion sample is a single crystal silicon pillar (in the direction out of the plane of the figure); as shown in the schematic, the torque is achieved through the forces provided to the lever arms by the right and left 2000 comb capacitor actuators. The measured buckled shape of the 500  $\mu\text{m}$  long and 1  $\mu\text{m}$  wide calibration beam is used in conjunction with an elaborate structural analysis of the instrument is performed to determine the forces. The purpose of this short review is to describe the authors' concept. Therefore details of the fabrication procedure and mechanical analysis (which makes up much of the above referenced paper) are not repeated here. In fact, the authors emphasize in their paper that the fracture experiments are intended to demonstrate the application of microinstruments for material characterization, and therefore the strength data should not be considered as conclusive.

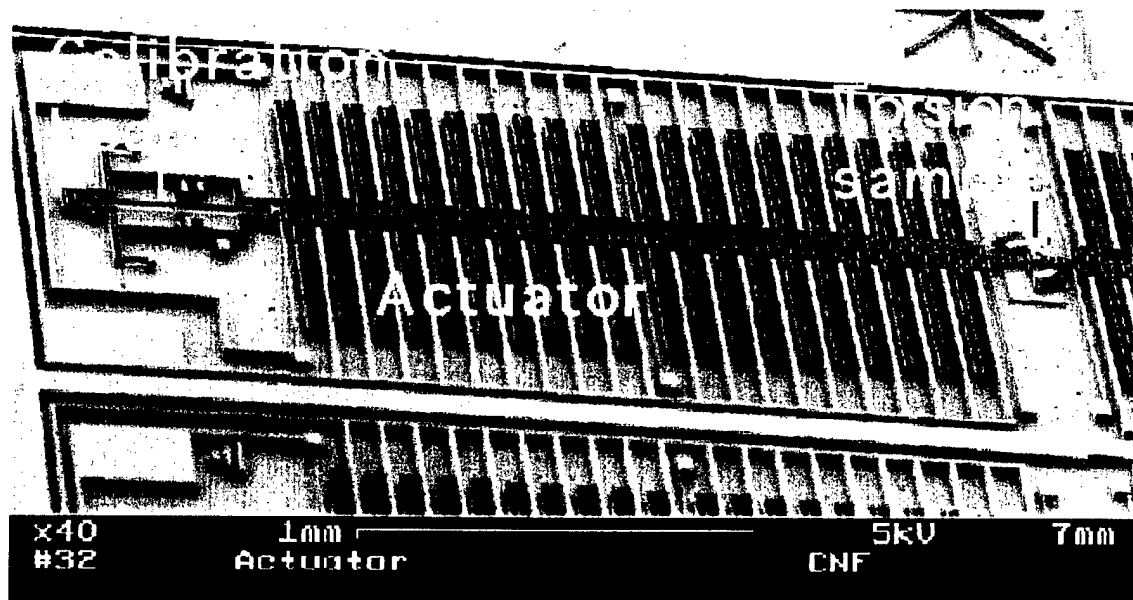
Close-ups of the calibration beam (and the Vernier scale used to determine the maximum displacement of the beam) and the torsion sample are shown in Figures 2 and 3, respectively. The dimensions of the two pillars tested were measured, using an SEM, as approximately 1  $\mu\text{m}$  x 1  $\mu\text{m}$  and 1.5  $\mu\text{m}$  x 1.6  $\mu\text{m}$ .

The experiment and calibration are conducted under an optical microscope using a probe station. As the voltage is increased on each instrument, its actuator approaches the calibrating beam. In turn, the gap  $\delta_1$  decreases, and the actuator touches the lever arm of the torsion sample. At this point the voltage is increased until the calibration beam just buckles. The voltage on both actuators is then increased equally. As the transverse deflection of the beam rapidly increases and is recorded (Figure 4), the actuators slowly advance along the axial direction and twist the sample (Figure 5). At a critical applied voltage the sample fractures.

The authors present a very detailed and informative discussion of the major assumptions of the calibration method, its limitations, and the design considerations of the calibration beam. They also suggest that the calibration procedure is currently being verified using a direct force sensor.



(a)



(b)

Figure 1- (a) Schematic (not to scale) of microinstrument and torsion sample. (b) SEM micrograph (Reference [1]).

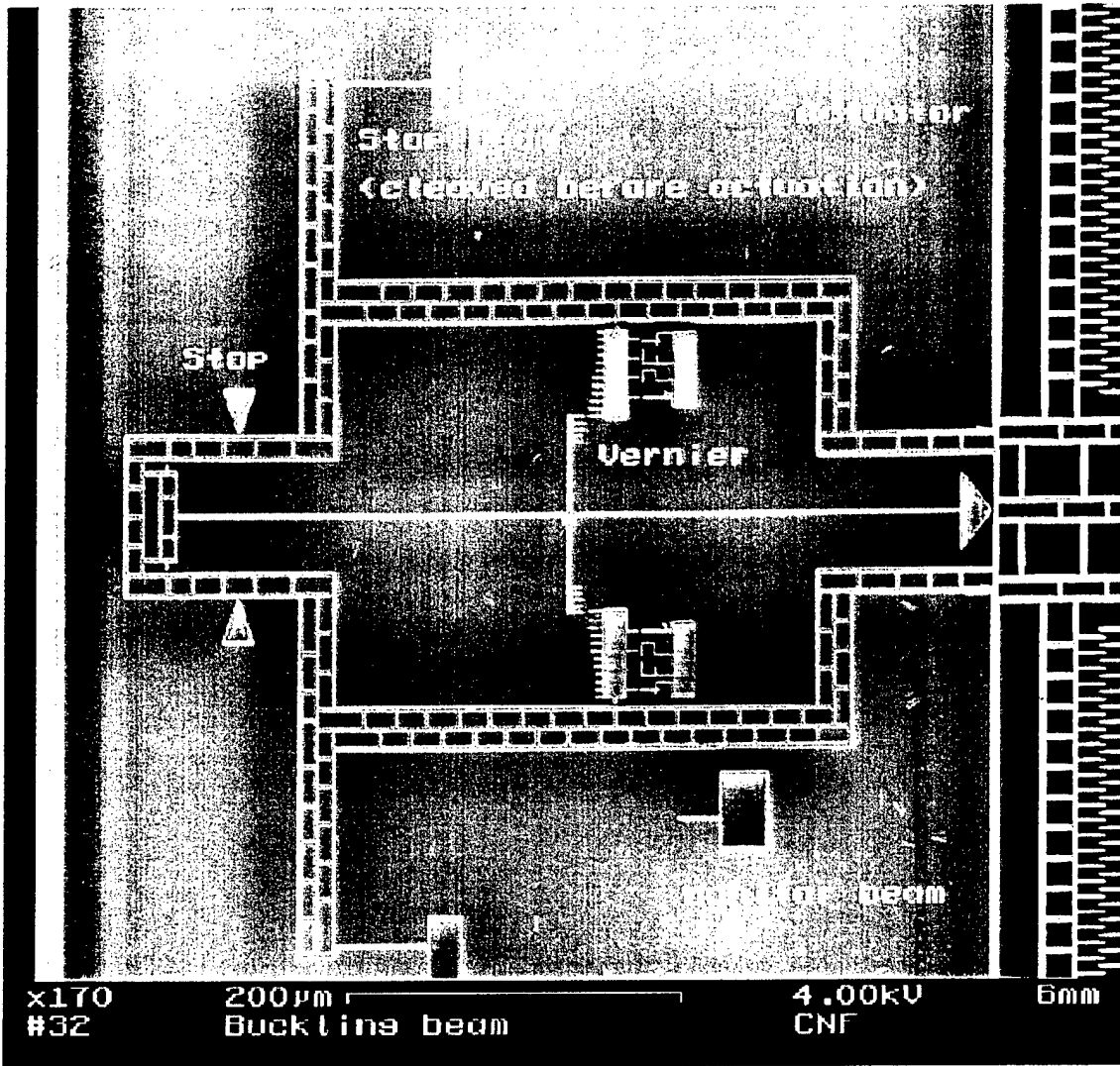


Figure 2- A calibrating beam and part of the actuator that it calibrates (Reference [1]).

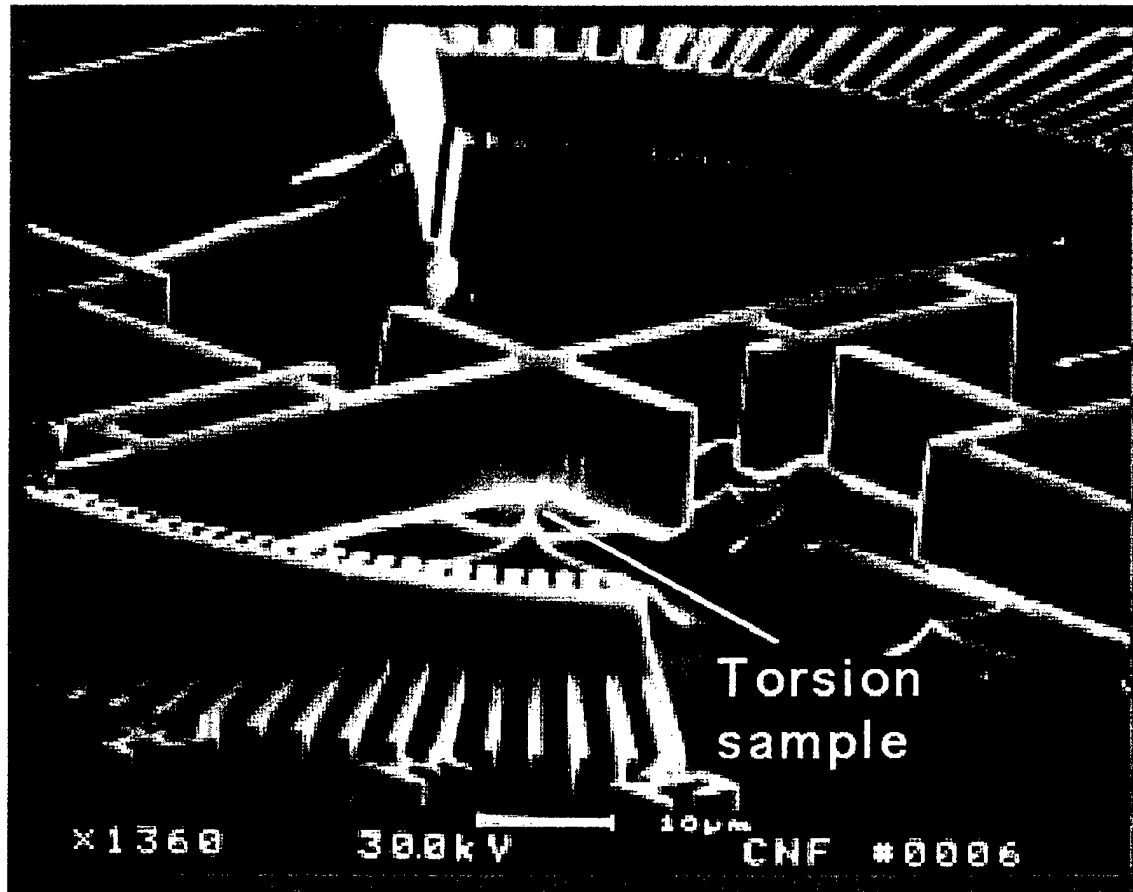


Figure 3- Close-up of torsion pillar (Reference [1]).



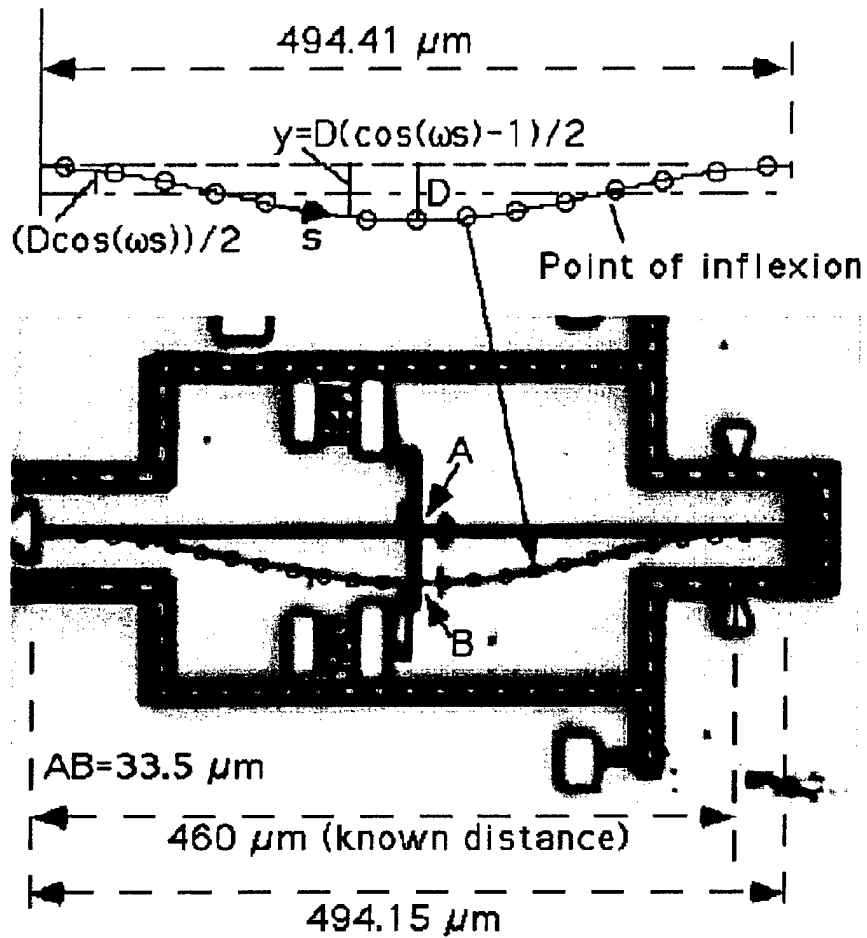
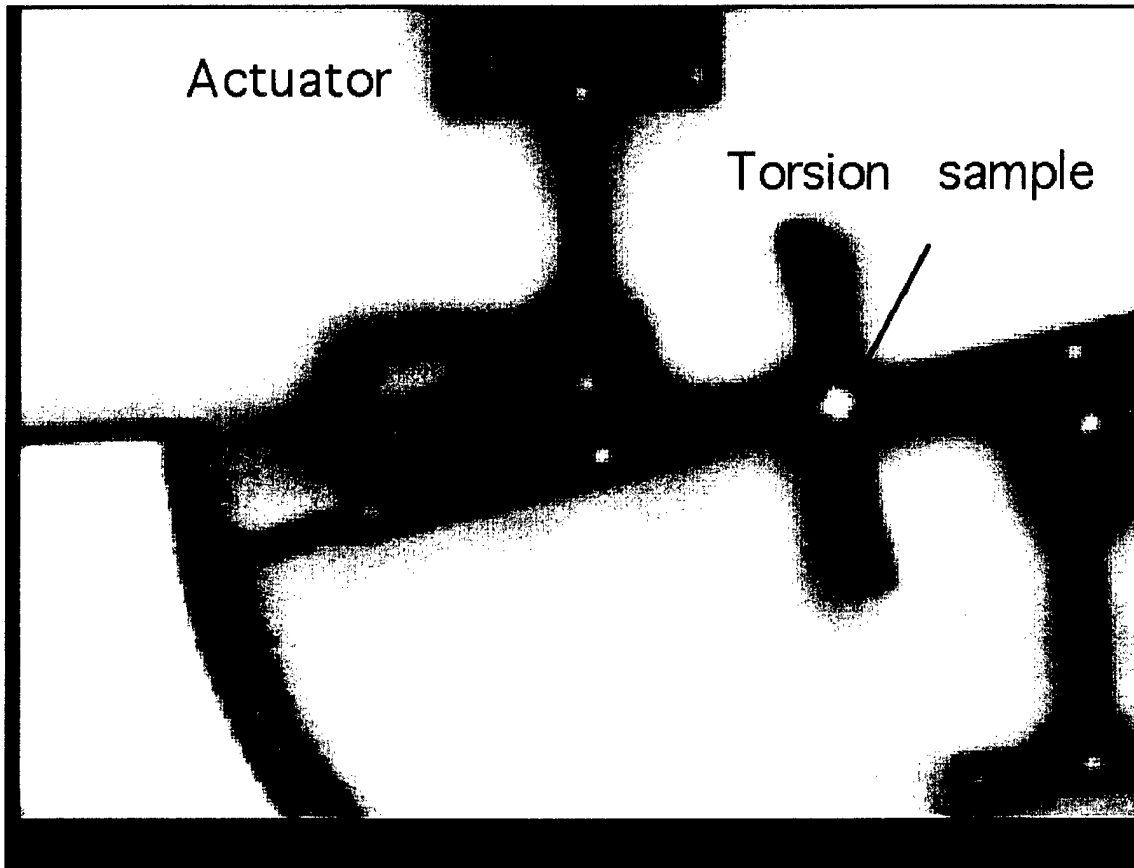


Figure 4- Optical microscope close-up of buckling beam. The circles denote the deflection predicted by theory (Reference [1]).



**Figure 5- Twisting of a torsion sample recorded under an optical microscope  
(Reference [1]).**

## **PART II**

### **REVIEW OF THEORETICAL WORK**

**CHAPTER 9            STATISTICAL METHODS FOR PREDICTING ELASTIC  
CONSTANTS OF POLYCRYSTALLINE FILMS**

**CHAPTER 10         THE EFFECTS OF HETEROGENEITY AND ANISOTROPY  
ON        CRACK-TIP   PARAMETERS   IN   CRACKED  
POLYCRYSTALLINE FILMS**

## CHAPTER 9

### STATISTICAL METHODS FOR PREDICTING ELASTIC CONSTANTS OF POLYCRYSTALLINE FILMS

#### 1. INTRODUCTION

Typical stress analyses of engineered structures rely on the assumption that the constituent materials are homogeneous, and in most cases, isotropic. These approximations have proved to be appropriate for structures whose characteristic dimensions are much larger than those of the material microstructure (steel and concrete buildings, for example). However, they *may* be inappropriate for MEMS devices, whose characteristic dimensions are of the same order as those of the constituent material's microstructure. Poly-Si is comprised of anisotropic single crystals possessing "cubic" symmetry. As shown schematically in Figure 1, the {100} and {110} are the most common textures that result from MEMS processing techniques. The random direction of the principal material axis within each grain, represented in this figure by the angle  $\psi$ , results in an inhomogeneous polycrystalline *structure*. Predicting the scatter in the nominal elastic constants of structures comprised of polycrystalline silicon motivated the development of the two models presented in this chapter, which can be easily modified to analyze general anisotropy. All calculations and results presented in this chapter correspond to the {100} texture. It is again noted that the films produced at CWRU and MCNC are {110}. Thus the numerical results cannot be directly compared to the experimental data.

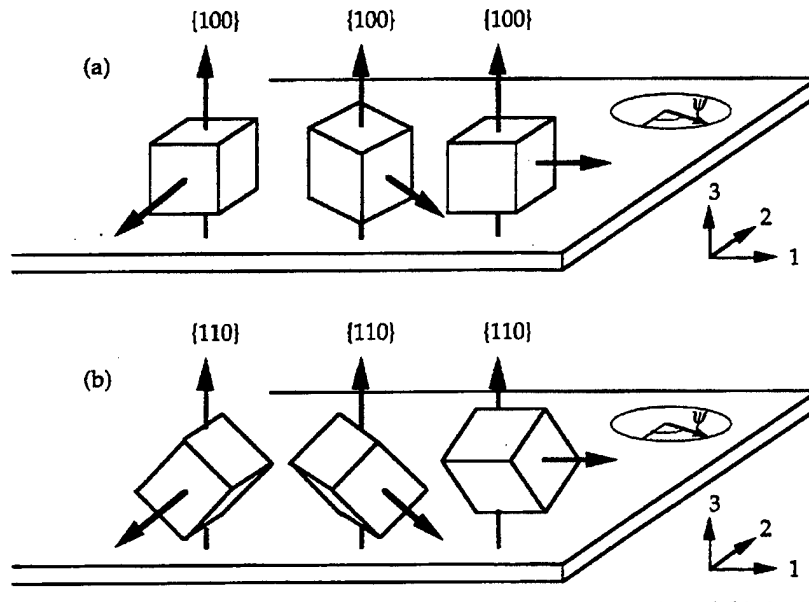


Figure 1- Schematic diagram of crystal orientations in (a) {100}, and (b) {110} thin film textures, showing in-plane rotations,  $\psi$  (From Reference [3] below).

Both models can be used to predict the average values and scatter of the nominal elastic constants of a film aggregate of anisotropic crystals. The first, proposed by the author and his coworkers, is a finite element based Monte Carlo method model described in the following references.

[1] *R.L. Mullen, R. Ballarini, Y. Yin and A.H. Heuer, "Monte Carlo simulation of effective elastic constants of polycrystalline thin films," Acta mater., Vol. 45, No. 6, pp. 2247-2255, 1997.*

[2] *Y. Yin, "Monte Carlo simulation of effective elastic constants of polycrystalline thin films," M.S. thesis, Department of Civil Engineering, Case Western Reserve University, Cleveland, Ohio, 1996.*

In the above referenced work, the microstructure is approximated as a Poisson-Voronoi tessellation and modeled explicitly using a finite element discretization of all the grains. Universal results for the average and variation of nominal plane strain Young's modulus and Poisson's ratio are presented as functions of the number of grains within a unit volume, and two parameters that quantify the level of the crystalline anisotropy. The predictions are compared with formulae that are derived for plane strain Voigt and Reuss bounds. For polycrystalline silicon films comprised of a large number of grains the model predicts an average *plane strain* Young's modulus equal to 168GPa, and an average Poisson's ratio of 0.22; these values cannot be compared directly with experimentally observed values of 178GPa and 0.22 (*W.N. Sharpe, Jr., B. Yuan, R.L. Edwards and R. Vaidyanathan, "Measurements of Young's modulus, Poisson's ratio, and tensile strength of polysilicon," Proceedings of the Tenth IEEE International Workshop on Microelectromechanical Systems, Nagoya, Japan, pp. 424-429, 1997*). The scientist and coworkers are currently calculating the results for the {110} texture.

This model can be improved by using a more realistic geometric modeling of the microstructure. There are several ways of doing this, depending on the objective. If one wanted to model a specific experimental specimen, electron backscattered diffraction micrographs of the specimen can be used to determine the geometry and crystallographic directions of the grains. This data in turn can be translated into a finite element mesh. If the objective is to improve on the statistical description of the microstructure that results from a specific processing procedure, an ensemble of micrographs of actual films can be used to calibrate the Voronoi model.

The model suffers from a relatively serious drawback. Being a Monte Carlo based technique, it is computationally intensive, and the results are dependent on load and displacement boundary conditions, grain sizes, and structural geometry. Moreover, while it provides average values and standard deviations of desired parameters, it does not provide autocorrelation functions.

The second method was developed to (1) eliminate the computational inefficiencies associated with the Monte Carlo method, and (2) provide an autocorrelation function for the process, so that it can be flexibly used in stochastic finite element codes. It is summarized in the following reference.

[3] *D. Mirfendereski, A. Der Kiureghian, M. Ferrari and G. Johnson, "Probabilistic characterization and response prediction of micro-electro-mechanical systems," Report (University of California, Berkeley: Structural Engineering, Mechanics and Materials), UCB/SEMM-96/04, 1996.*

This procedure employs an equivalent continuous-parameter random field characterization of the crystalline microstructure, in which the auto-correlation function for equivalent elastic properties of the field are generated by a moving window approach in fields of simulated crystals. As in the first model, observed geometries can be used if available.

Determining the average elastic and plastic properties of polycrystalline materials has been the focus of much research during the past fifty years. Before the advent of the computer, analytical models relied on simplifying assumptions regarding the interactions of individual crystals as well as their shape. As far as the scientist knows, the first analytical model for an aggregate of cubic crystals was proposed by Hershey (*A.V. Hershey, "The elasticity of an isotropic aggregate of anisotropic cubic crystals," ASME Journal of Applied mechanics, Vol. 21, pp. 236-240, (1954)*). Christensen (*R.M. Christensen, "A critical evaluation for a class of micro-mechanics models," Journal of the Mechanics and Physics of Solids, Vol. 38, pp. 379-404, (1990)*) provides an excellent critique of different classes of analytical models for predicting the elastic and inelastic response of composite materials. A practical limitation of these models is that they do not provide estimates for the *scatter* of the properties from their mean value, as functions of the number of grains within a unit volume. This information may be very important in certain applications. For example, specifications for disposable blood pressure sensors require *one percent* accuracy in pressure readings (*J. Bryzek, R. Mayer and P. Barth, "Disposable Blood Pressure Sensors with Digital On-Chip Laser Trimming," IEEE Solid-State Sensor and Actuator Workshop, Hilton Head Island, South Carolina, June 6-9, pp. 121-122, (1988)*), which translates into at most one percent accuracy in predicted deflections, and hence elastic moduli. Currently this performance is achieved by using bulk micromachined *single crystal* silicon. Surface micromachining provides more flexibility in geometric design, but uses polycrystalline silicon. If this material is to be used in applications which require precise predictions of mechanical response, then a quantitative understanding of the scatter in its elastic moduli that results from the inhomogeneity of the microstructure is paramount. To estimate the dispersion in elastic constants accurately, one needs to perform analyses that model the microstructure explicitly, as is done in the above referenced papers.

## 2. REFERENCES [1] AND [2]

These papers present a Monte Carlo simulation that predicts the nominal elastic constants and their coefficient of variation of *films* comprised of a finite assembly of cubic crystals. Poly-Si is such a structures. As discussed previously, the microstructure is typically (nearly) columnar. This supports the two dimensional finite element analysis which is presented in the next section. The analysis relies on a Voronoi tessellation of the microstructure, and follows the approach taken by Kumar (*S. Kumar, "Computer*

*Simulation of 3D Material Microstructure and Its Application in the Determination of Mechanical Behavior of Crystalline Materials and Engineering Structures*, Ph.D. Thesis, Department of Engineering Science and Mechanics, The Pennsylvania State University, (1992)), who focused on comparing, for a large number of grains, the predictions from this model with those derived from available analytical models.

### Description of numerical model

With respect to the global coordinate system  $x$ - $y$ - $z$  shown in Figure 2, the thin film is analyzed under plane strain conditions,  $u_z = \frac{\partial(\ )}{\partial z} = 0$ , where  $u_z$  is the displacement in the  $z$  direction, and  $(\ )$  denotes any physical quantity. For a given number of grains  $n$ , the topology of the microstructure within the *unit* volume shown in Figure 2 is approximated, for *each* of  $m$  simulations, as a Voronoi tessellation. The tessellation is constructed by first generating, using a Poisson process, a set of random nucleus points  $\vec{r}_i$  ( $i=1, n$ ). The set of all points which are closer to  $\vec{r}_i$  than to any other nucleus  $\vec{r}_j$  ( $i \neq j$ ) comprise the  $i$ th Voronoi cell. The assembly of the  $n$  convex, planar edged cells, defines the tessellation. Each grain is discretized with a sufficient number of quadratic displacement finite elements. The details of the algorithm used to construct the tessellation and the finite element method solution procedure can be found in Reference [2].

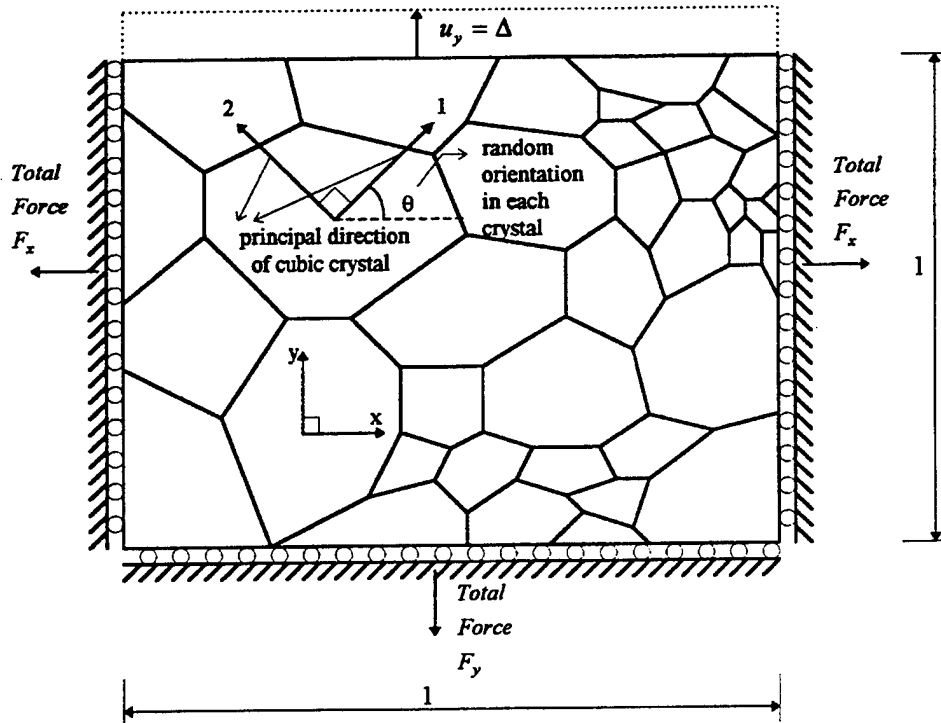


Figure 2-Poisson-Voronoi tessellation of microstructure for  $n$ -grains ( $n=5$ -1000) (Reference [1]).

Each grain is assumed to possess cubic symmetry. With respect to the local coordinate axes  $1-2$  shown in Figure 2, which represent the principal material directions of a typical grain, the stress-strain relations are given, in matrix and component form, by Hooke's law for a cubic material in plane strain

$$\{\sigma\} \equiv \begin{Bmatrix} \sigma_{11} \\ \sigma_{22} \\ \sigma_{12} \end{Bmatrix} = [C]\{\varepsilon\} \equiv \begin{bmatrix} c_{11} & c_{12} & 0 \\ c_{12} & c_{11} & 0 \\ 0 & 0 & 2c_{44} \end{bmatrix} \begin{Bmatrix} \varepsilon_{11} \\ \varepsilon_{22} \\ \varepsilon_{12} \end{Bmatrix} \quad (1)$$

where  $\sigma_{ij}$  and  $\varepsilon_{ij}$  ( $i, j = 1, 2$ ) are, respectively, components of the symmetric stress and strain tensors. System  $1-2$  is rotated through angle  $\theta$  from the global  $x$ -axis. The requirement that the strain energy be positive definite places the following restrictions on the elastic constants

$$c_{11} > 0 \quad c_{11}^2 - c_{12}^2 > 0 \quad c_{44} > 0 \quad (2)$$

The level of anisotropy is quantified by the parameters  $A$  and  $\bar{\nu}$ , defined as

$$A \equiv \frac{2c_{44}}{c_{11} - c_{12}} \quad (3a)$$

$$\bar{\nu} \equiv \frac{c_{12}}{c_{11} + c_{12}} \quad (3b)$$

The combination  $(c_{11} - c_{12})/2$  represents the shear modulus associated with the shear strain of an element whose normals are rotated  $45^\circ$  with respect to the principal directions, while  $\bar{\nu}$  is the apparent plane strain Poisson ratio associated with uniaxial loading along the principal directions. For isotropic materials  $A=1$  and  $\bar{\nu} = \nu$ , where  $\nu$  is Poisson's ratio. The randomness of the orientation of the principal directions is introduced by assigning, to each cell, a uniformly distributed random angle  $\theta$ .

The thin film *structure* is loaded, as shown in Figure 2, through the following boundary conditions

$$u_y = \Delta, \quad y=1 \quad (4a)$$

$$u_x = \sigma_{xy} = 0, \quad x=0, \quad x=1 \quad (4b)$$

$$u_y = \sigma_{xy} = 0, \quad y=0 \quad (4c)$$

These are associated with nominal (average) strain components  $\varepsilon_{yy}^n = \Delta/1$ ,  $\varepsilon_{xx}^n = 0$ ,  $\varepsilon_{xy}^n = 0$ . The finite element method is used to calculate the total reaction forces (per unit thickness)  $F_x$  and  $F_y$  shown in Figure 3, which for the unit length edges, correspond to nominal stress components  $\sigma_{xx}^n$  and  $\sigma_{yy}^n$ , respectively. The



associated nominal values of the Poisson ratio  $\nu^n$  and plane strain Young's modulus  $\bar{E}^n \equiv E^n/[1-(\nu^n)^2]$  are defined by invoking Hooke's law for the *isotropic* continuum under plane strain conditions

$$\begin{Bmatrix} \sigma_{xx}^n = F_x \\ \sigma_{yy}^n = F_y \\ \sigma_{xy}^n = 0 \end{Bmatrix} = \frac{E^n}{(1+\nu^n)(1-2\nu^n)} \begin{bmatrix} 1-\nu^n & \nu^n & 0 \\ \nu^n & 1-\nu^n & 0 \\ 0 & 0 & (1-2\nu^n) \end{bmatrix} \begin{Bmatrix} \epsilon_{xx}^n = 0 \\ \epsilon_{yy}^n = \Delta \\ \epsilon_{xy}^n = 0 \end{Bmatrix} \quad (5)$$

Equations (5) provide

$$\nu^n = \frac{1}{1 + \frac{F_y}{F_x}} \quad (6a)$$

$$\bar{E}^n = \frac{E^n}{[1-(\nu^n)^2]} = \frac{(1+\nu^n)(1-2\nu^n)}{\nu^n[1-(\nu^n)^2]} \frac{F_x}{\Delta} \quad (6b)$$

The steps described above are repeated  $m$  times for each value of  $n$ .

### Voigt and Reuss Bounds for Plane Strain

The plane strain elastic constants defined as Reuss bounds are isotropic within the plane and are calculated by averaging the single crystal stiffness matrix over all possible orientations of the random angle  $\theta$ . The average stiffness matrix is calculated as

$$[C]^{Reuss} \equiv \frac{1}{2\pi} \int_0^{2\pi} [T]^T [C] [T] d\theta \quad (7)$$

where matrix  $[T]$  and its transpose  $[T]^T$ , which transform the stiffness matrix from principle axes to those rotated by angle  $\theta$ , are defined by

$$[T] \equiv \begin{bmatrix} \cos^2 \theta & \sin^2 \theta & \cos \theta \sin \theta \\ \sin^2 \theta & \cos^2 \theta & -\cos \theta \sin \theta \\ -2\cos \theta \sin \theta & 2\cos \theta \sin \theta & \cos^2 \theta - \sin^2 \theta \end{bmatrix} \quad (8)$$

Equating the result of the integration in (7) with the stiffness matrix in (5) provides

$$\nu^{Reuss} = \frac{c_{11} + 3c_{12} - 2c_{44}}{4(c_{11} + c_{12})} \quad (9a)$$

$$\bar{E}^{Reuss} = \frac{E^{Reuss}}{[1-(\nu^{Reuss})^2]} = \frac{(1+\nu^{Reuss})}{2[1-(\nu^{Reuss})^2]} (c_{11} - c_{12} + 2c_{44}) \quad (9b)$$

The plane strain elastic constants defined as Voigt bounds are isotropic within the plane and are calculated by averaging the single crystal compliance matrix over all possible orientations of the random angle  $\theta$ . The average compliance matrix is calculated as

$$[S]^{Voigt} \equiv \frac{1}{2\pi} \int_0^{2\pi} [T]^T [C]^{-1} [T] d\theta \quad (10)$$

where the superscript -1 denotes matrix inverse. Equating the result of the integration in (10) with the inverse of the stiffness matrix in (5) provides

$$v^{Voigt} = -\frac{2s_{11} + 6s_{12} - s_{44}}{2(2s_{11} - 2s_{12} + s_{44})} \quad (11a)$$

$$\bar{E}^{Voigt} = \frac{E^{Voigt}}{[1 - (v^{Voigt})^2]} = \frac{4(1 + v^{Voigt})}{[1 - (v^{Voigt})^2](2s_{11} - 2s_{12} + s_{44})} \quad (11b)$$

in which

$$s_{11} \equiv \frac{c_{11}}{c_{11}^2 - c_{12}^2} \quad s_{12} \equiv -\frac{c_{12}}{c_{11}^2 - c_{12}^2} \quad s_{44} \equiv \frac{1}{c_{44}} \quad (12)$$

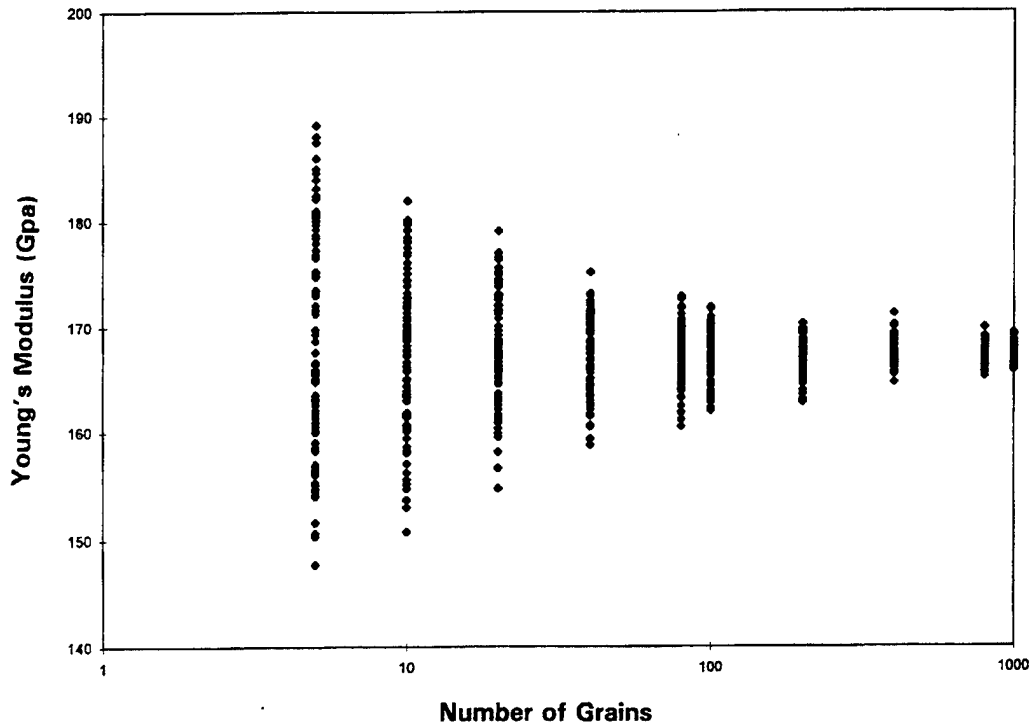


Figure 3- Scatter of silicon's nominal plane strain Young's modulus  $\bar{E}^n$  as a function of number of grains  $n$  (Reference [1]).

## Results

Typical results are presented in Figure 3, which show the scatter in silicon's ( $c_{11} = 2.55c_{12} = 2c_{44} = 160GPa$ , ( $A = 1.65$ ,  $\bar{\nu} = 0.28$ ))  $\bar{E}^n$  for  $m=100$  realizations. It is observed that even for 1000 grains the scatter is on the order of a few percent. This implies that polysilicon microdevices whose characteristic dimensions are less than  $\approx 1mm$  cannot be used in designs that rely on knowledge of the elastic modulus to within a few percent.

The coefficient of variation (COV) of  $\bar{E}^n$  of eight cubic materials, defined as

$$COV \equiv \sqrt{\frac{1}{(m-1)(\bar{E}_{avg}^n)^2} \sum_m \left[ (\bar{E}^n)^2 - (\bar{E}_{avg}^n)^2 \right]} \quad (13)$$

is presented in Table 1 as a function of number of grains in the film. In Equation (13) the subscript "avg" denotes the average value of  $m$  simulations.

Table 2 ( $m=100$ ) shows that the plane strain Young's modulus and Poisson's ratio predicted by the model for 1000 grains lie within the Voigt and Reuss bounds. Figures 4 and 5 show, for  $\bar{\nu} = 0.1, 0.2, 0.3, 0.4$ , the effects of  $A$  on  $\bar{E}^n$  and  $\nu^n$  for

Number of Cells	Aluminum	Ammonium Bromide	Argon	Calcium Fluoride	Cesium	Diamond	Gold	Silicon
Character Properties	c11=108.24 c12=62.16 c44=28.41 A=1.23 $\bar{\nu}$ =0.107	c11=29.60 c12=5.90 c44=5.30 A=0.447 $\bar{\nu}$ =0.166	c11=5.29 c12=1.35 c44=1.59 A=0.807 $\bar{\nu}$ =0.203	c11=162.80 c12=43.30 c44=33.40 A=0.559 $\bar{\nu}$ =0.210	c11=2.59 c12=2.17 c44=1.60 A=7.62 $\bar{\nu}$ =0.456	c11=950.00 c12=390.00 c44=430.00 A=1.54 $\bar{\nu}$ =0.291	c11=194.00 c12=166.00 c44=40.00 A=2.86 $\bar{\nu}$ =0.461	c11=168.00 c12=66.00 c44=84.00 A=1.65 $\bar{\nu}$ =0.282
5	0.029	0.091	0.026	0.074	0.246	0.047	0.188	0.061
10	0.022	0.069	0.015	0.056	0.205	0.037	0.118	0.041
20	0.014	0.054	0.015	0.037	0.134	0.027	0.085	0.030
40	0.010	0.033	0.008	0.025	0.096	0.018	0.062	0.021
80	0.007	0.023	0.007	0.017	0.065	0.013	0.041	0.015
100	0.006	0.026	0.005	0.015	0.064	0.011	0.035	0.013
200	0.005	0.016	0.004	0.013	0.041	0.009	0.029	0.009
400	0.004	0.012	0.003	0.008	0.032	0.006	0.019	0.007
800	0.002	0.008	0.002	0.006	0.028	0.004	0.013	0.005
1000	0.002	0.008	0.002	0.005	0.023	0.004	0.011	0.004

**Table 1- Coefficient of variation of nominal plane strain Young's modulus  $\bar{E}^n$  of various cubic materials versus number of grains;  $c_{ij} \times 10^{-6} Pa$  shown (Reference [1]).**

Materials	Character Properties			Voigt		Reuss		Model (1000 Grains, 100 Simulations)	
	c11	c12	c44	Young's Modulus	Poisson Ratio	Young's Modulus	Poisson Ratio	Young's Modulus	Poisson Ratio
Aluminum	108.24	62.16	28.41	79.0	0.349	78.4	0.351	78.7	0.350
Ammonium Bromide	29.60	5.90	5.30	23.1	0.258	20.8	0.294	22.0	0.277
Argon	5.29	1.35	1.59	4.64	0.232	4.60	0.235	4.62	0.234
Calcium Fluoride	162.80	43.30	33.40	128	0.274	121	0.292	125	0.284
Cesium	2.59	2.17	1.60	2.63	0.310	1.29	0.422	1.98	0.369
Diamond	950.00	390.00	430.00	928	0.235	901	0.247	913	0.242
Gold	194.00	166.00	40.00	94.0	0.425	74.3	0.442	86.3	0.432
Silicon	168.00	66.00	84.00	172	0.212	165	0.229	168	0.221

**Table 2- Comparison of predicted mean values of plane strain modulus  $\bar{E}^n$  and Poisson's ratio  $\bar{\nu}^n$  with Voigt and Reuss bounds ( $n=1000$ ) (Reference [1]).**

In these plots  $\bar{E}^n$  is normalized with the "isotropic" plane strain Young's modulus  $\bar{E}^{isotropic}$  obtained by equating the first entry in the stiffness matrix for cubic symmetry, for  $A=1$  (for fixed  $\bar{\nu}$ ) with that of an isotropic material, i.e.

$$\bar{E}^{isotropic} \equiv \frac{c_{11}(1+\bar{\nu})(1-2\bar{\nu})}{(1-\bar{\nu})^3} \quad (14)$$

It is observed that the mean value of the elastic constants is relatively insensitive to the number of grains for the practical range  $A < 10$ . The predicted values lie between the Voigt and Reuss bounds. It is also interesting to note that negative values of the effective Poisson ratio are realized as a result of the inherent anisotropy of the constituent grains.

Figure 6 shows, for  $\bar{\nu} = 0.1, 0.2, 0.3, 0.4$ , the  $COV$  of  $\bar{E}^n$  as functions of  $A$  for  $n=10, 100, 1000$ . These plots clearly show that the  $COV$  of the nominal Young's modulus is more sensitive to  $\bar{\nu}$  than to  $A$ .

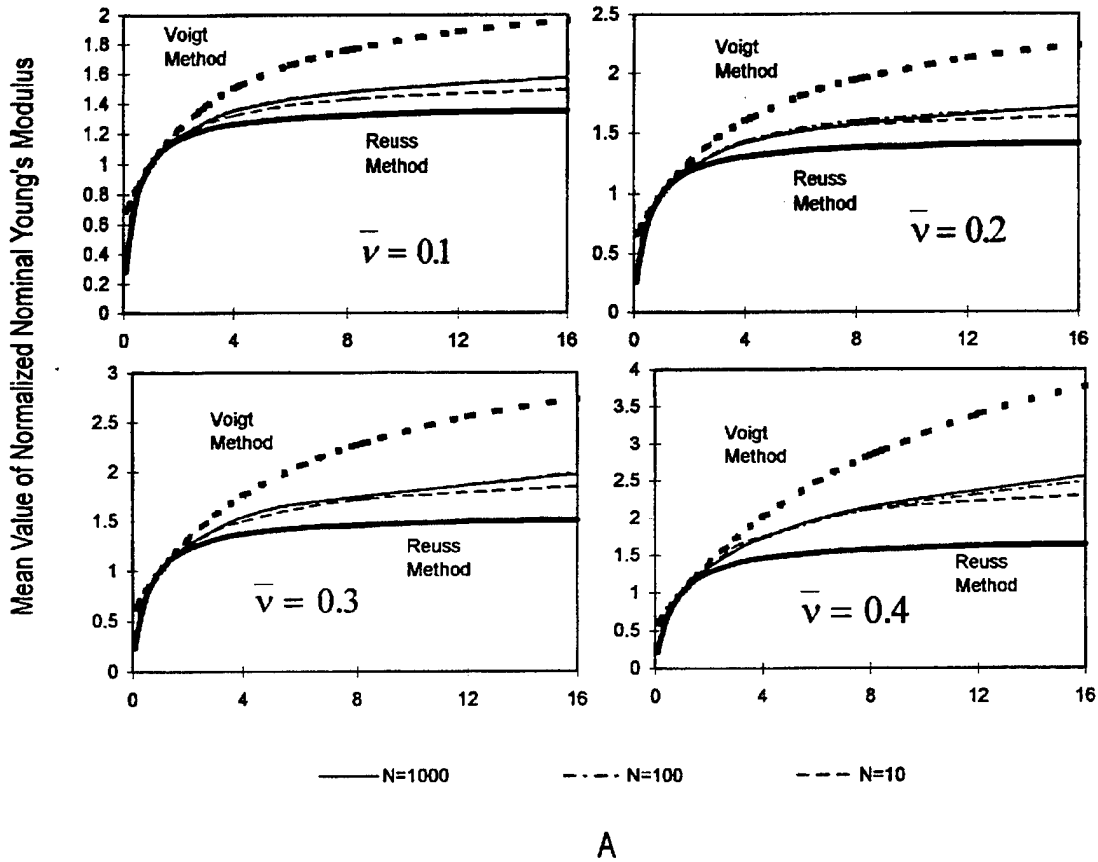
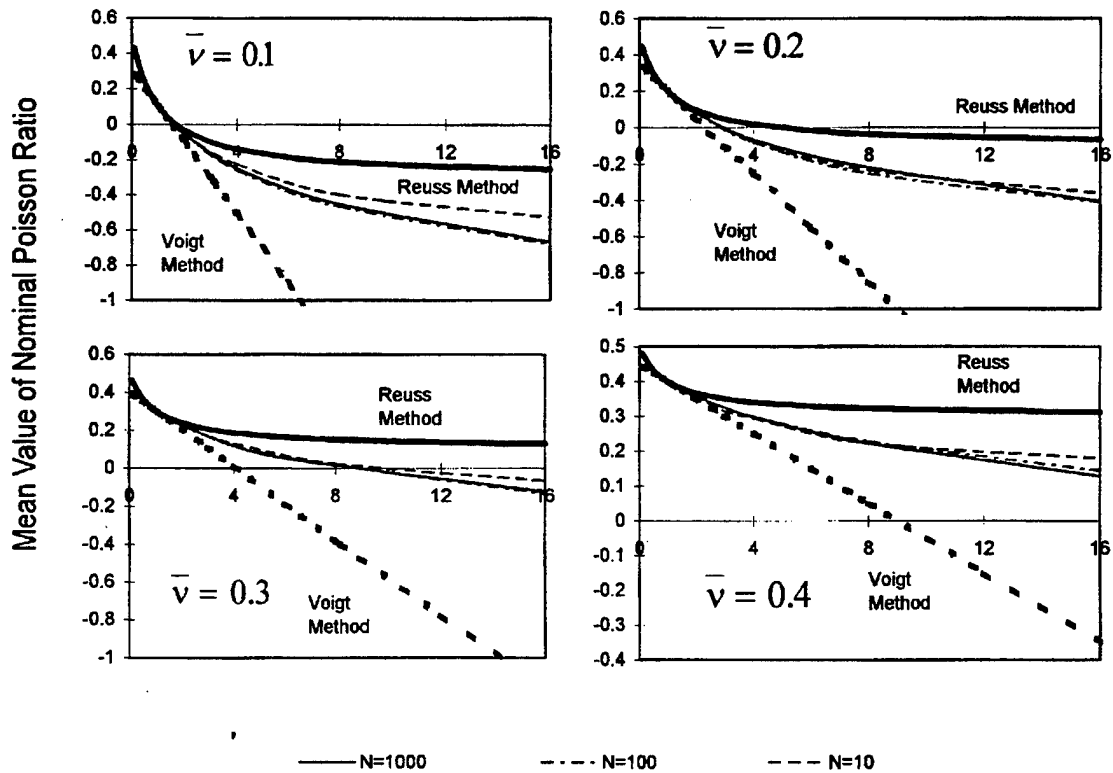


Figure 4- Mean value of normalized nominal plane strain Young's modulus  $\bar{E}^n / \bar{E}^{isotropic}$  as functions of anisotropy parameter  $A$  (Reference [1]).

Figure 7 shows the standard deviation ( $SD$ ) of  $\nu^n$ , defined as

$$SD \equiv \sqrt{\frac{1}{(m-1)} \sum_m \left[ (\nu^n)^2 - (\nu_{avg}^n)^2 \right]} \quad (15)$$

Figures 6 and 7 can be used to predict the inherent scatter in the nominal plane strain elastic constants of a thin film comprised of a cubic material.



A

Figure 5- Mean value of nominal Poisson's ratio  $\nu^n$  as functions of anisotropy parameter A (Reference [1]).

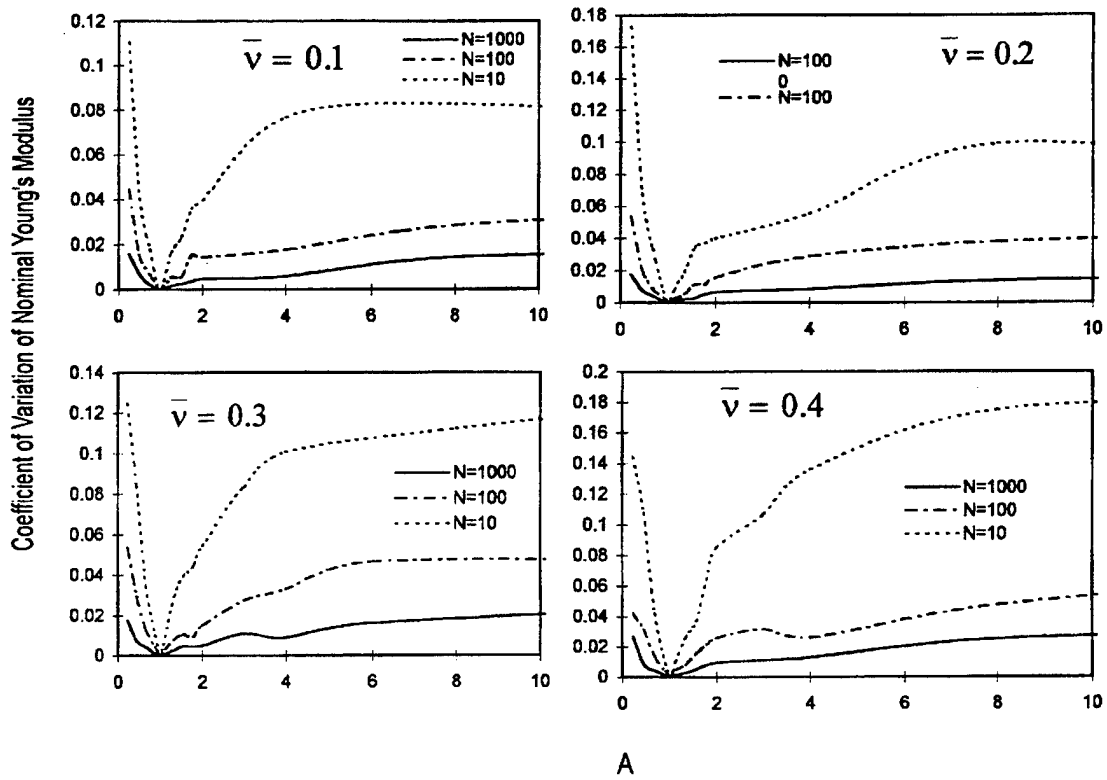
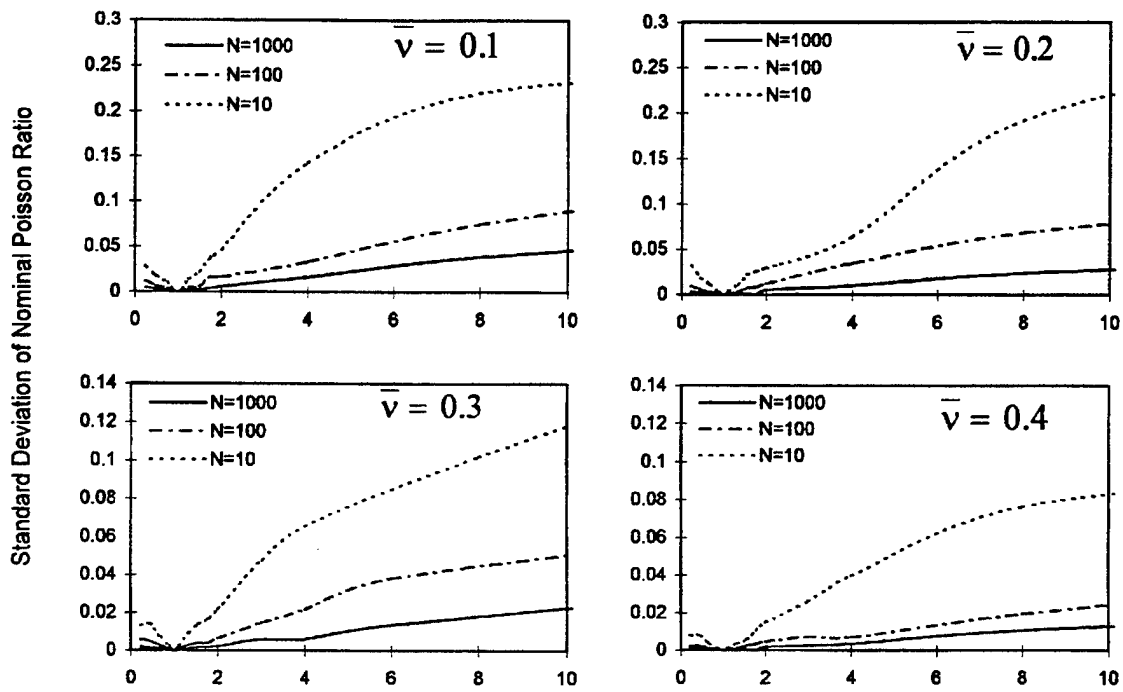


Figure 6- Coefficient of variation of nominal plane strain Young's modulus  $\bar{E}^n$  as functions of anisotropy parameter  $A$  (Reference [1]).



A

Figure 7- Standard deviation of nominal Poisson's ratio  $\nu^n$  as functions of anisotropy parameter A (Reference [1]).



### 3. REFERENCE [3]

In this report the authors developed a random field approach for characterizing the flexural and axial behavior of polycrystalline beams. The authors also suggest a methodology for extending the method to two and three dimensional grain structures. An equivalent continuous parameter random field characterization of the crystalline microstructure is developed, whereby the auto-correlation function for equivalent elastic properties of the field are generated by a moving window approach in fields of simulated crystals. The advantages of this method over the previously described Monte Carlo approach (which they also used to calculate benchmark solutions) are that (1) the randomness in the elastic modulus at a point along the beam length is incorporated in one equation, written in terms of random variables and the deterministic spatial coordinate, and (2) length scale effects are included through an autocorrelation function and correlation length. Therefore the same random field model can be re-used within the context of conventional stochastic finite element methods to calculate the mean and standard deviation of the response statistics.

The response of a beam is essentially a one dimension problem that depends on the bending stiffness  $EI(x)$ , where  $E$  is Young's modulus,  $I$  is the moment of inertia, and  $x$  is a point along the beam. In this section only the results for constant inertia are summarized. The authors did calculate examples with random variations in inertia; these can be recovered in Reference [3].

#### Calculation of random field using the finite element method

The original predictions of the model relied on a finite element stress analysis of the discretized polycrystalline structure. The first step consists of constructing Poisson-Voronoi tessellations (for a given value of the parameter that quantifies the average number of grains in a unit area) of an ensemble of polycrystalline beams, as shown in Figure 9. Next the geometry is discretized using finite elements, and a crystal orientation distribution function is assigned. Consider the axial loading case of Figure 9(a), which shows a window containing three grains. For each geometry, this window of width  $W$  and depth  $d$  at position  $x$  is subjected to a prescribed stress  $\sigma_T$ , and the average displacement of the right side of the window relative to the left is calculated. Dividing this displacement by the width of the window provides the average strain  $\epsilon_{avg}$ , and in turn the effective (tension) Young's modulus within the window,  $E_T \equiv \sigma_T / \epsilon_{avg}$ . Repeating these calculations for a sufficient number of points that span the beam provides the continuous effective modulus  $E_{eff}(x)$ , which represents the limit of  $E_T$  as  $W$  approaches zero. Typical realizations are shown in Figure 8. This ensemble of  $E_{eff}(x)$  realizations is then used to find the mean, standard deviation, and autocorrelation function of the random field  $E_{eff}(x)$ . Because this random field is to be used as an input into stochastic finite element codes, it is discretized into a set of deterministic functions and a finite number of random variables using the Expansion Optimal Linear Estimation (EOLE) method (C.C. Li and A. Der Kiureghian, "Optimal Discretization of Random Fields," *Journal of*

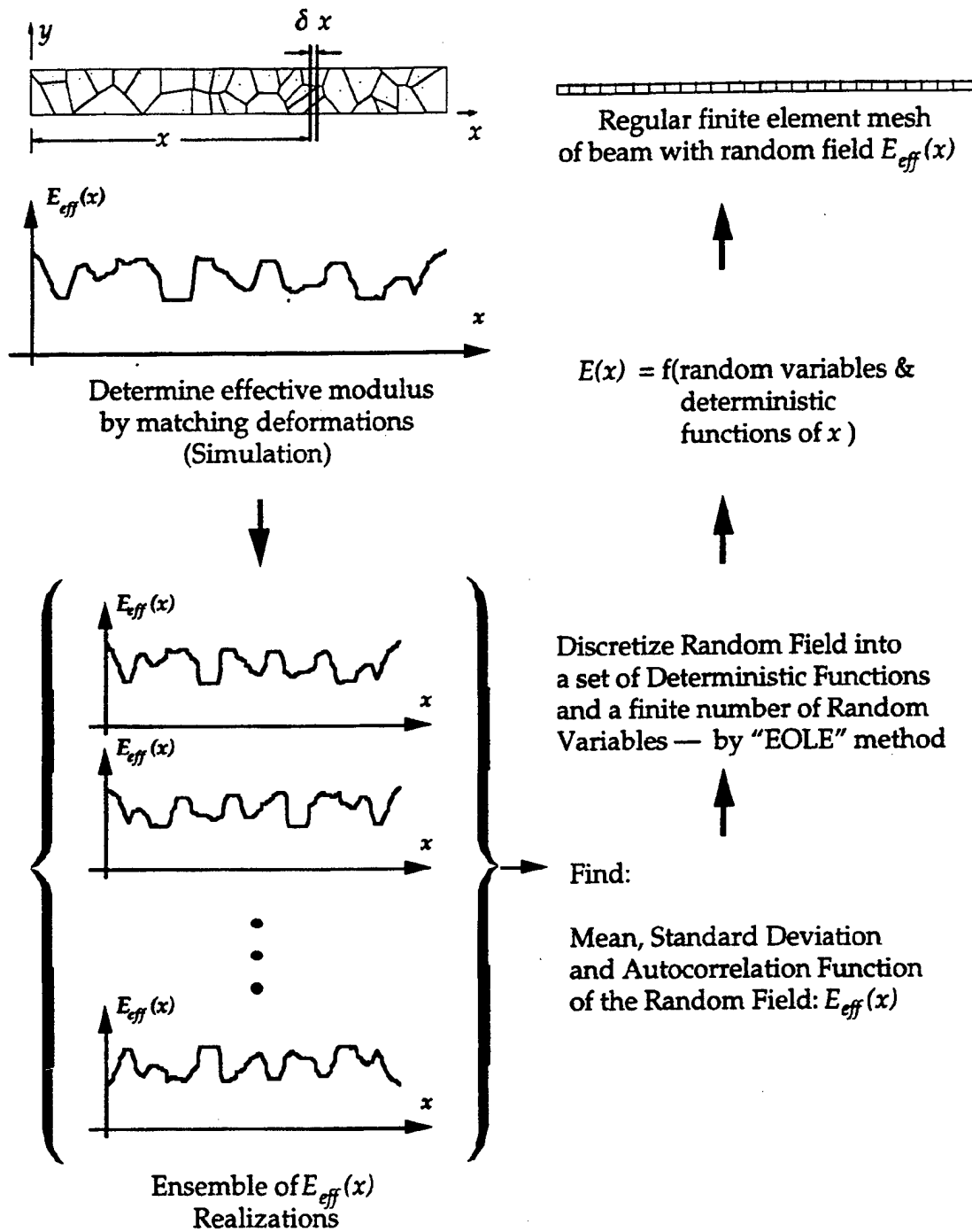
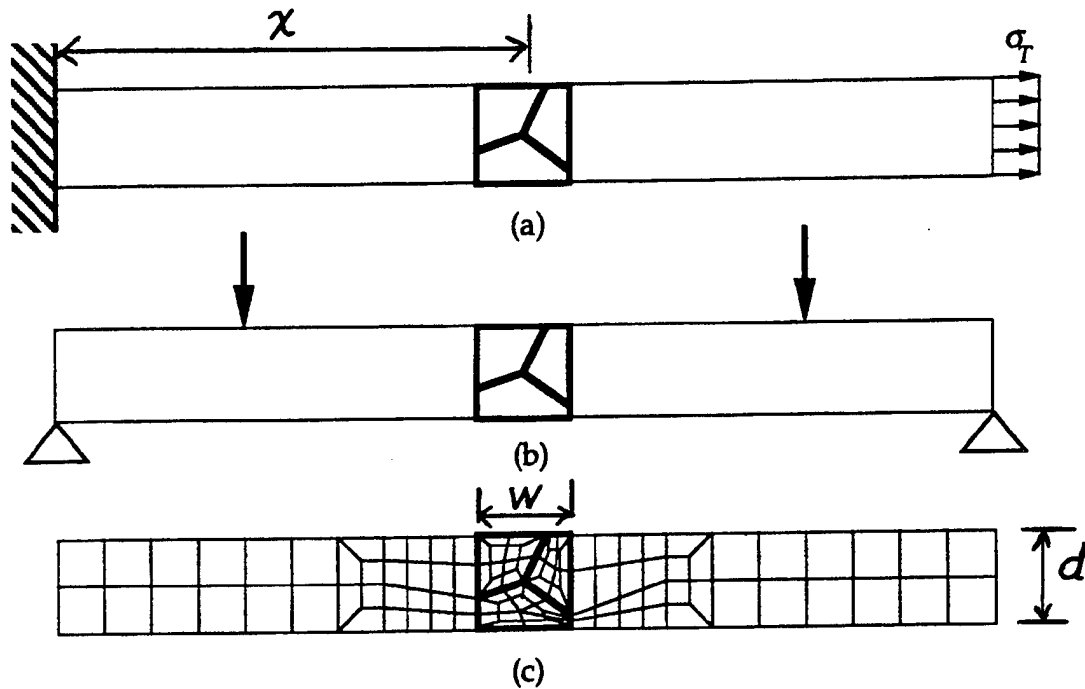


Figure 8- Random field model (Reference [3]).

*Engineering Mechanics, ASCE, Vol. 119, No. 6, pp. 1136-1154, 1993*). The flow chart of the procedure is shown in Figure 8.

The authors also calculated the modulus functions for flexural loading using the configuration shown in Figure 9(b). The details of these slightly more involved calculations are not presented here.

Because the finite element calculations require repeated remeshing of the windows, the procedure is cumbersome and computationally demanding. The authors subsequently developed explicit equations for the effective Young's modulus through an analytic-geometric approximation that eliminated the need of finite element calculations, as described next.



**Figure 9- Beam in tension (a), flexure (b), finite element model of moving window (Reference [3]).**

### Analytic-geometric derivation

Consider a vertical slice of length  $\delta x$  along the polycrystalline beam shown in Figure 8. This slice is shown schematically in Figure 10. As the length approaches zero, this slice reduces to a section of the beam, which is composed of  $n$  crystals, each with a distinct and random orientation angle  $\psi_i$  and projected area  $A_i$ . The different shadings indicate the different crystals. The distance from the axis to the top surface of each crystal is denoted by  $d_i$ . The contribution of each crystal to the effective Young's modulus in the direction of the beam's axis is approximated using standard (stiffness) transformation formulas, and can be written in terms of the angle between the principal direction and the axis, and the stiffness coefficients defined in Equation (1), as

$$E_i = E(\psi_i, c_{11}, c_{12}, c_{44}) \quad (16)$$

For uniform tension, the effective modulus is approximated as a (relative area) weighted average

$$E_w \approx \frac{1}{A_{total}} \sum_{i=1}^n A_i E(\psi_i) \quad (17)$$

For flexural loading, the standard transformed cross-sectional area approach is used. The resulting analytic expressions for the effective modulus are not reproduced here. However, it can easily be shown that for both tension and flexural loading, in the limit as the slice approaches zero, the following expression results

$$E_{eff}(x) = \sum_{i=1}^n w_i E(\psi_i) \quad (18)$$

where the weights  $w_i$  are functions of the  $d_i$ .

Using Equation (18), realizations of the random field of the effective Young's modulus along a multicrystalline beam are computed. One such realization, for flexural loading and uniformly distributed  $\psi$ , is shown in Figure 11. By generating an ensemble of such realizations, statistical characteristics of the random field (mean, variance, and auto-correlation function) were obtained using a class of models introduced by Vanmarcke (*E. Vanmarcke, Random Fields: Analysis and Synthesis, The MIT Press, Cambridge, Massachusetts, 1983*). The details are not reproduced here. A comparison of beam deflection using this approximate method with the finite element based method is shown in Figure 12. It is observed that the approximate model does a good job at predicting the deflection.

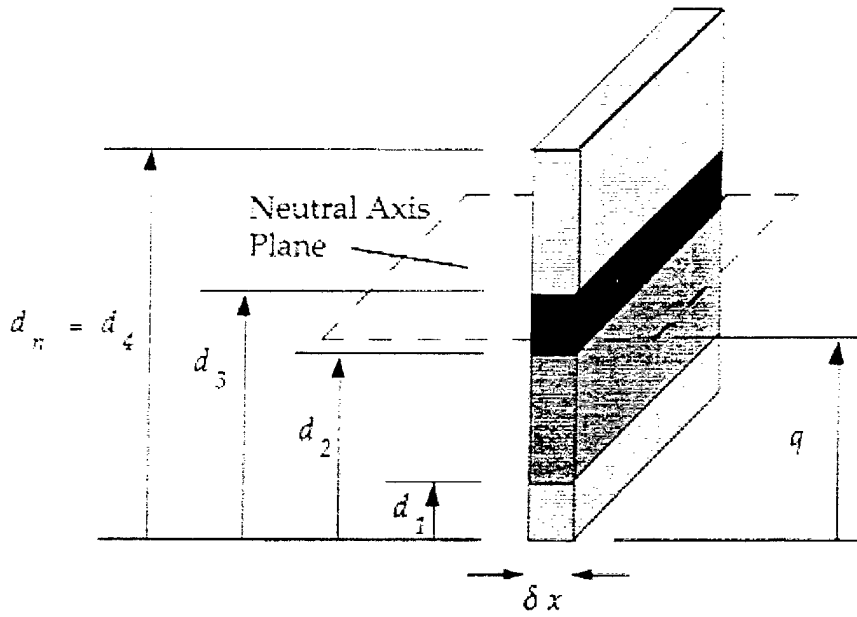


Figure 10- Cross-section of vertical slice (Reference [3])

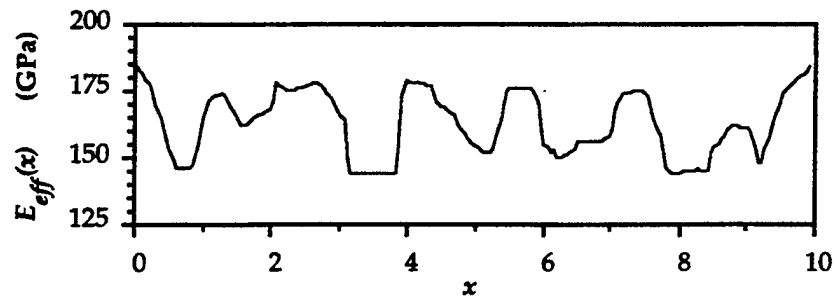
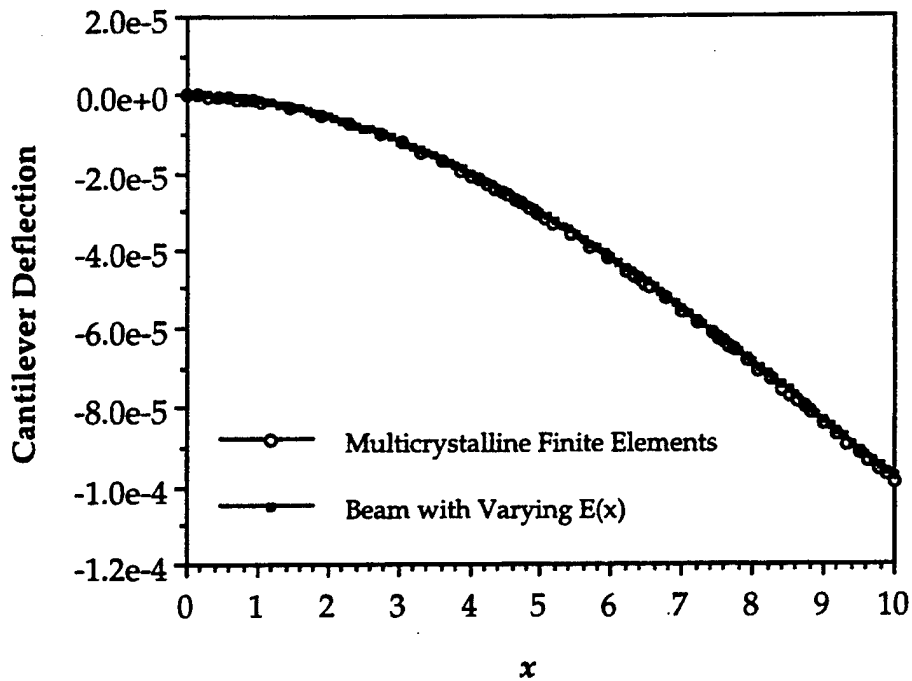


Figure 11- One realization of the (Young's modulus) random field (Reference [3]).



**Figure 12- Comparison of beam deflection using multicrystalline finite element calculations and using analytic-geometric closed form solutions.**

#### 4. CRITIQUE

The theoretical models presented in this chapter demonstrate the powerful computer-based stochastic methods available to predict the elastic properties of heterogeneous materials and structures. While they require lots of time on the computer, they are superior to classic closed-form solutions that only provide average values and wide bounds; they can be used to generate as many moments of elastic properties as desired.

## CHAPTER 10

### THE EFFECTS OF HETEROGENEITY AND ANISOTROPY ON CRACK-TIP PARAMETERS IN CRACKED POLYCRYSTALLINE FILMS

#### 1. INTRODUCTION

This section summarizes two papers that investigate the effects of heterogeneity on crack-tip parameters in cracked polycrystalline films. Specifically, the models provide quantitative estimates of how the local stress intensity factors and energy release rate differ from those associated with the assumption that the material is homogeneous and isotropic. This information is needed to determine whether fracture mechanics analyses of microelectromechanical system devices require discrete modeling of the material microstructure, or whether the assumption of homogeneity (and isotropy) will suffice. The first model, developed by the author and coworkers as part of their research on poly-Si, has been submitted for publication as

[1] *R. Ballarini, R.L. Mullen and A.H. Heuer, "The effects of heterogeneity and anisotropy on the size effect in cracked polycrystalline films," submitted for publication.*

The second model, developed Abdel-Tawab and Rodin in their study of columnar sea-ice, is described in

[2] *K. Abdel-Tawab and G.J. Rodin, "Fracture size effects and polycrystalline inhomogeneity," MSS&M Report No. 97/12, Research Center for Mechanics of Solids, Structures & Materials, The University of Texas at Austin, July 1997.*

In linear elastic fracture mechanics (LEFM) theory of homogeneous materials, the nominal stress  $\sigma_n$  is expressed in terms of the stress intensity factor  $K_I$  as

$$\sigma_n = \frac{K_I}{a^{1/2} F} \quad (1)$$

where  $a$  is the crack length and  $F$  is a dimensionless function which depends on the loading and specimen geometry. In this one parameter system, the critical stress  $\sigma_n^c$  is determined, for the desired loading, geometry, and crack length, by equating the stress intensity factor with the material's fracture toughness,  $K_{Ic}$ . The associated crack stress analysis for the homogeneous material produces a *macroscopic* (nominal or far-field) stress intensity factor, which will henceforth be denoted  $K_I^\infty$ . The critical stress intensity factor criterion is equivalent to the condition that the energy release rate, defined for *self-*

*similar* extension as  $G_I^\infty \equiv \frac{(K_I^\infty)^2}{E'}$ , reaches a critical value  $G_{Ic} = \frac{K_{Ic}^2}{E'} = 2\gamma$ , where

$E' = E$  for plane stress,  $E' = E / (1 - \nu^2)$  for plane strain,  $\gamma$  is the surface energy,  $E$  is Young's modulus, and  $\nu$  is Poisson's ratio. LEFM is based on the assumption that the "process zone" in the immediate vicinity of the crack tip, within which irreversible deformation occurs and linear elasticity breaks down, is sufficiently small compared to other relevant length scales, so that there exists an annular region surrounding it within which the stresses are dominated by the elastic stress intensity factor. Moreover, the assumption of homogeneity implicitly assumes that the process zone extends from the crack tip to a distance much larger than the crystal (grain) size, and thus engulfs and in turn is engulfed by a sufficiently large number of grains that behave as a homogeneous medium. Abdel-Tawab and Rodin (Reference [2]) suggest that a material's tendency to behave homogeneously can be screened by the grain brittleness,  $GB$ , defined as

$$GB \equiv \frac{d}{r_p} \quad (2)$$

Here  $d$  is the grain size, and  $r_p$  is the size of the process zone, which can be estimated as

$$r_p = 0.1c \left( \frac{K_{Ic}}{\sigma_u} \right)^2 \quad (3)$$

where  $\sigma_u$  represents a limiting stress appropriate for a given material system (yield stress for metals, tensile strength for brittle materials), and  $c$  is a constant close to unity. The assumption of homogeneity is appropriate for  $GB \gg 1$ ; if  $GB$  is not sufficiently large, then the irreversible deformations at the crack tip do not overwhelm microstructure induced inhomogeneity, and the details of the microstructure surrounding the process zone may have a significant effect on the fracture process. Indeed, because of the randomness of the distribution and orientation of the grains, these effects will be of a statistical nature. It has been established experimentally that the fracture toughness of most engineering materials depends on specimen dimensions. The amount of this so called "size effect", which results from differences in the relative size of the process zone in geometrically similar but different sized specimens, varies from material to material. Much research has been conducted by the fracture mechanics community in the past twenty years aimed at describing and predicting the size effect. This effort has produced scaling laws through cohesive zone models (*B.N. Cox and D.B. Marshall, Acta Metall. Mater. 42, pp. 341-363, 1994*), dimensional analysis (*Z.P. Bazant, ASCE Journal of Engineering Mechanics 119, pp. 1828-1844, 1993*), and fractal geometry concepts (*A. Carpinteri, Mechanics of Materials 18, pp. 89-101, 1994*). The main advantage of these formulations is that they can be easily implemented into analysis/design tools for predicting crack propagation in engineered structures. However, by smearing out the details of the deformation mechanisms involved in the fracture process, and by treating the phenomena deterministically and/or phenomenologically, they lose information that can be valuable in the interpretation of scatter in experimental data.

From the limited available experimental data, it appears that polycrystalline silicon does not develop microcracking in the vicinity of a dominant crack. Therefore there won't be any contributions from this phenomena to the size effect. It remains to be determined whether heterogeneity produces significant size effects.



The work summarized in this chapter focuses on characterization of the fracture mechanics parameters of a crack in a columnar aggregate of randomly orientated, perfectly bonded crystals under plane deformation. The following question is addressed: given the parameters that quantify the level of crystalline anisotropy, the number of grains in a unit volume, and a far field loading defined by  $K_I^\infty$ , what are the average values and standard deviations of the *microscopic* (local) stress intensity factors  $K_I^l$  and  $K_{II}^l$  and energy release rate  $G^l$ ? This information, which should shed some light on why the fracture toughness of brittle polycrystalline structures is prone to scatter and size effects, can be obtained only by using micromechanical models that treat the microstructural details and associated deformation mechanisms explicitly. As stated in Reference [2], the ultimate goal of such models is to develop size effect maps analogous to those for deformation mechanisms (*H.J. Frost and M.F. Ashby, Deformation Mechanism Maps, Pergamon Press, Oxford, 1982*), and that characterization of the individual size effects produced by inhomogeneity is the first step towards this end. The next logical step towards this end, is to include the effects of the microcracking (within the grains or along grain boundaries) that often develops in the vicinity of the crack tip.

In Reference [2], which focused on fracture mechanics size effects in sea-ice, an approximate analytical model and a finite element plane strain model calculated the difference between  $K_I^\infty$  and  $K_I^l$  at the tip of a *long* crack surrounded by a *large* number of brittle hexagonal crystals with *perfectly bonded* interfaces. This local parameter is needed because, for a heterogeneous material,  $G_I^\infty$  and  $\gamma$  in the fracture criterion should be replaced by  $G^l$  and  $\gamma^l$ , where  $\gamma^l$  is the local value of critical energy release rate. Abdal-Taweb and Rodin's contribution showed that, in an aggregate comprised of a very large number of grains, the grains remote from the crack tip do not induce significant differences between the macroscopic and microscopic stress intensity factors. For example, their calculations showed that even for highly anisotropic crystals,  $K_I^l$  is only twenty percent less than  $K_I^\infty$  ( $K_{II}^l$  was negligible for the nominal mode-I loading). They concluded that for such materials the contribution of inhomogeneity to the size effect is relatively weak. Moreover, their results suggest that the crack-tip parameters of materials with large values of  $GB$  are controlled by only a few grains near the crack tip, and provide a rational explanation of why fracture toughness data exhibits significant statistical effects. As they pointed out, the results are expected to change dramatically if microcracking within grains or along grain boundaries is included in the models. As will be discussed later on in this chapter, the results are also expected to change dramatically if the structure is comprised of a very few grains.

One of the issues that was not discussed in Reference [2] is fatigue. For brittle polycrystalline materials, crack growth under cyclic  $K_I^\infty$ , or under constant  $K_I^\infty$  and corrosive environments, has been quantified with power law functions of the type  $\frac{da}{dN} = C(\Delta K_I^\infty)^m$  and  $\frac{da}{dt} = D(K_I^\infty)^p$ , where  $N$  and  $t$  represent number of cycles and time, respectively, and  $C, D, m$  and  $p$  are experimentally measured constants. Because  $m$  and  $p$  are typically larger than, say 10, small heterogeneity induced fluctuations in local crack-tip parameters may suddenly become important in lifetime predictions.

In Reference [1] the authors developed a Monte Carlo finite element based model for quantifying the size effect due to heterogeneity and anisotropy in polycrystalline films. The calculations predict the average and standard deviation of the *microscopic* (local) stress intensity factors and energy release rate of a crack in a columnar aggregate of randomly orientated, perfectly bonded, orthotropic crystals (grains) under plane deformation. The boundary of the near-tip region is subjected to displacement boundary conditions associated with a *macroscopic* (far field or nominal) Mode-I stress intensity factor and average elastic constants calculated for the uncracked film with a large number of grains. The average and standard deviation of the microscopic stress intensity factors and energy release rate, normalized with respect to the macroscopic parameters, are presented as functions of the number of grains within the near-tip region, and the parameters that quantify the level of crystalline anisotropy. It is shown that for a given level of anisotropy, as long as the crack tip is surrounded by at least ten grains, then the expected value and standard deviation of the crack tip parameters are insensitive to the number of crystals. For selected values of crystalline anisotropy, the probability distributions of Mode-I stress intensity factor and stress ahead of the crack are also presented. The results suggest that the size effect due to heterogeneity and anisotropy is weak; crack initiation load and direction are governed only by the details of the grains in the immediate vicinity of the crack tip.

This model extends the calculations presented in Reference [2] to include *orthotropic* crystals and an *arbitrary* number of crystals within a unit volume. Furthermore, the model can be generalized to quantify the effects of microcracking in the process zone that often surrounds the crack tip in a brittle system. It was developed to quantify the effects of heterogeneity and anisotropy on the *scatter* and potential size effects in the *nominal* fracture toughness (critical value of  $K_I^\infty$ ) and fatigue data of microelectromechanical systems. Using a first generation microfracture specimen, they reported that the critical  $J$  integral (which provided a nominal fracture toughness) of notched polycrystalline silicon, which is one of the principal materials currently used in the fabrication of MEMS devices, exhibited significant scatter, but was not sensitive to the number of crystals in the uncracked ligament. The number of crystals in the uncracked ligament was larger than ten.

Silicon possesses cubic symmetry, a  $K_{Ic} \approx 0.8 \text{ MPa}\sqrt{\text{m}}$ ,  $\sigma_{ult} = 1.2 \text{ GPa}$ , and a crystal size  $d \approx 0.5 \mu\text{m}$ . The resulting  $GB \approx 10$  suggests that heterogeneity and anisotropy may play a significant role in the fracture behavior of polycrystalline silicon devices that are comprised of a small number of grains (connecting beams are typically a few microns wide, and may be comprised of less than ten grains). The microstructure of typical devices is (nearly) columnar. This supports the assumption of plane strain in subsequent finite element analyses.

## 2. REFERENCE [1]

### Review of near-tip mechanics

This section defines the mechanics problem and a review of the deterministic *dual length scale mechanics* near the tip of a crack in a polycrystalline material. The average

properties of the film, which enter into subsequent calculations, were calculated using the Monte Carlo method described in the previous chapter (Refer to Figure 3 of the previous chapter, and define  $l$  as the average crystal dimension). Figure 1 shows the same aggregate with a crack, loaded, as explained subsequently, with prescribed displacements at the boundary consistent with a macroscopic stress intensity factor  $K_I^\infty$  (or  $G_I^\infty$ ). The problem consists of calculating the *average* and *standard deviation* of the microscopic crack-tip parameters  $K_I^l$ ,  $K_{II}^l$  and  $G^l$  as functions of the level of crystalline anisotropy and the number of grains in a unit volume. This information is needed because the crack will extend at a critical combination of the microscopic stress intensity factors  $K_I^l$  and  $K_{II}^l$ , which are linearly related to  $K_I^\infty$ , but otherwise depend on the details of the microstructure in the immediate vicinity of the crack tip. Alternatively, the crack can be assumed to propagate at an energy release rate  $G^l$  (which is defined subsequently) equal to a critical value  $\gamma^l$ . The propagation criterion in a single crystal, which is beyond the scope of this paper, is an important issue that is receiving attention (A. Azhdari and S. Nemat-Nasser, *J. Mech. Phys. Solids* 44, pp. 929-951, 1996; A. Azhdari and S. Nemat-Nasser, to appear in *Mechanics of Materials*, 1998).

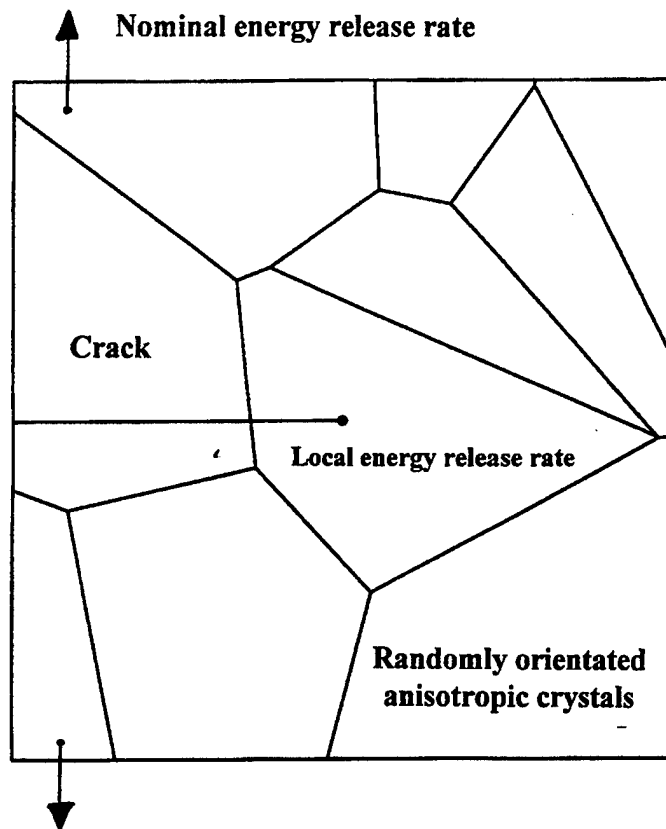
The problem of predicting crack propagation in the polycrystalline medium is complicated by the fact that function  $F$  in equation (1) now depends on details such as the number of crystals in a unit area, the relative position of the crack tip within the crystal, and the orientations of the principal material directions within each crystal.

The crystalline structure is approximated as a Poisson-Voronoi tessellation, consisting of  $n$  grains, using the approach described in the previous chapter. However, each grain is now assumed to possess either cubic or orthotropic symmetry. This is accomplished by relaxing the condition  $c_{22} = c_{11}$  in Equation (1) of the previous chapter, which results in three anisotropy parameters

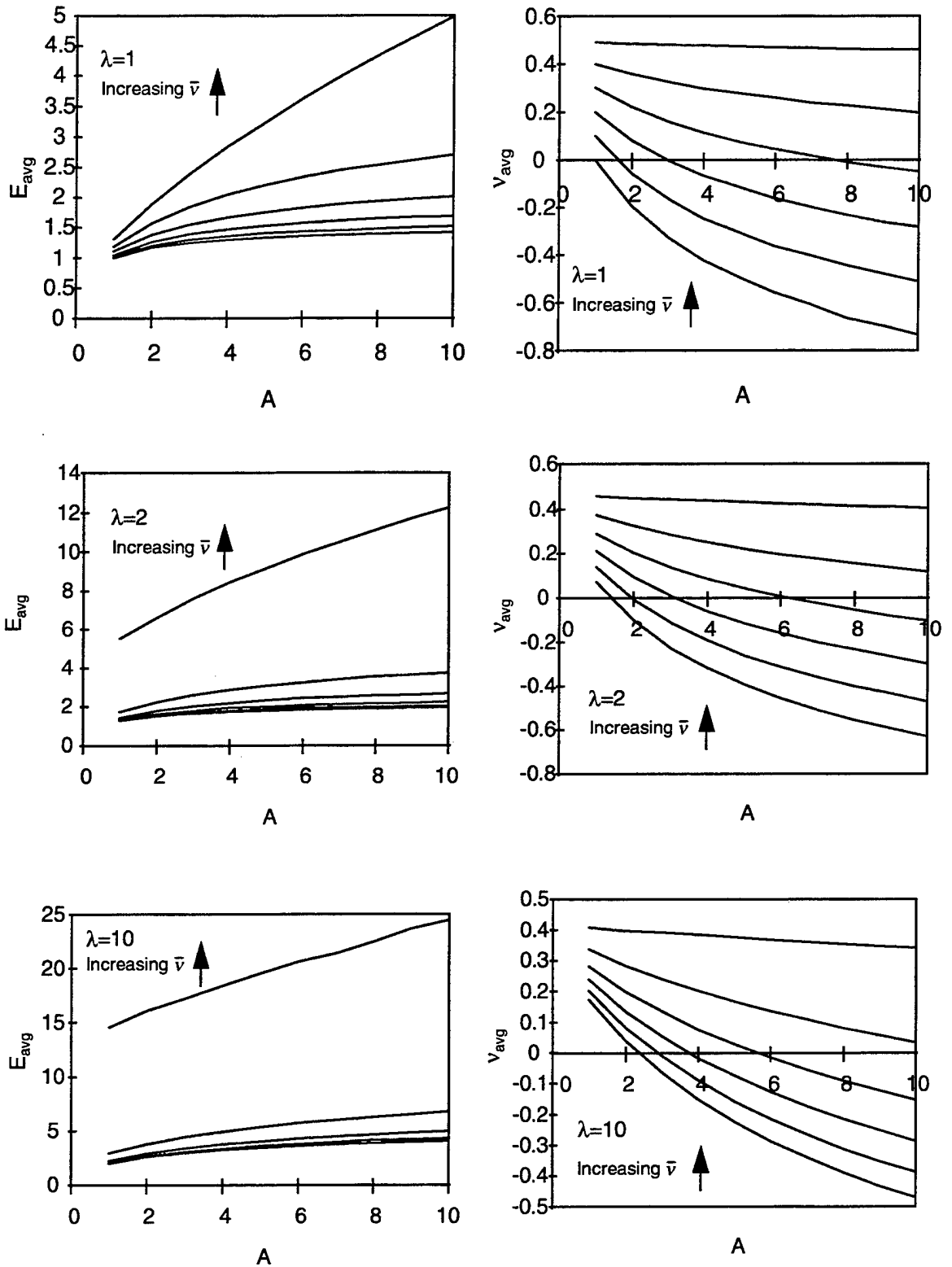
$$A \equiv \frac{2c_{44}}{c_{11} - c_{12}} \quad (4)$$

$$\bar{\nu} \equiv \frac{c_{12}}{c_{11} + c_{12}} \quad (5)$$

$$\lambda = \frac{c_{11}}{c_{22}} \quad (6)$$



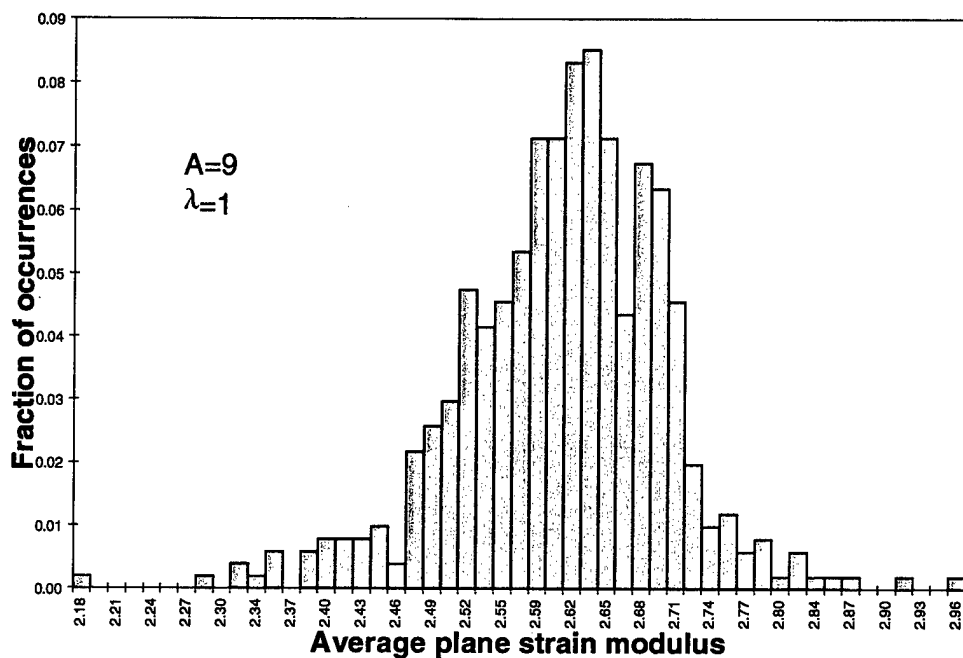
**Figure 1- Poisson-Voronoi tessellation of a crack in an aggregate of crystals (Reference [1]).**



**Figure 2- Average values of normalized plane strain Young's modulus and Poisson's ratio as functions of anisotropy parameters;  $\bar{\nu} = 0,0.1,0.2,0.3,0.4,0.5$  (Reference [1]).**

For isotropic materials  $A=1$ ,  $\bar{\nu} = \nu$ , and  $\lambda=1$ . For clarity, the following definitions from the previous chapter are repeated. The nominal Poisson's ratio and nominal plane strain Young's modulus are defined as  $\nu^n \equiv \nu$  and  $E^n / (1 - (\nu^n)^2)$ , respectively. The normalized plane strain modulus,  $E$ , is obtained by normalizing the nominal plane strain modulus with respect to the "isotropic" plane strain modulus  $E^{isotropic}$ , which is obtained by equating the first entry in the stiffness matrix  $C$ , for  $A=1$  (for fixed  $\bar{\nu}$ ), with that of an isotropic material, i.e.  $E^{isotropic} \equiv c_{11}(1 - 2\bar{\nu}) / (1 - \bar{\nu}^2)$ .

For an aggregate comprised of a very large number of grains (an average of  $n=750$  grains within a unit area of film), Figures 2 show, as functions of  $A$  and  $\bar{\nu}$ , the average values of the nominal Poisson's ratio and normalized plane strain Young's modulus.



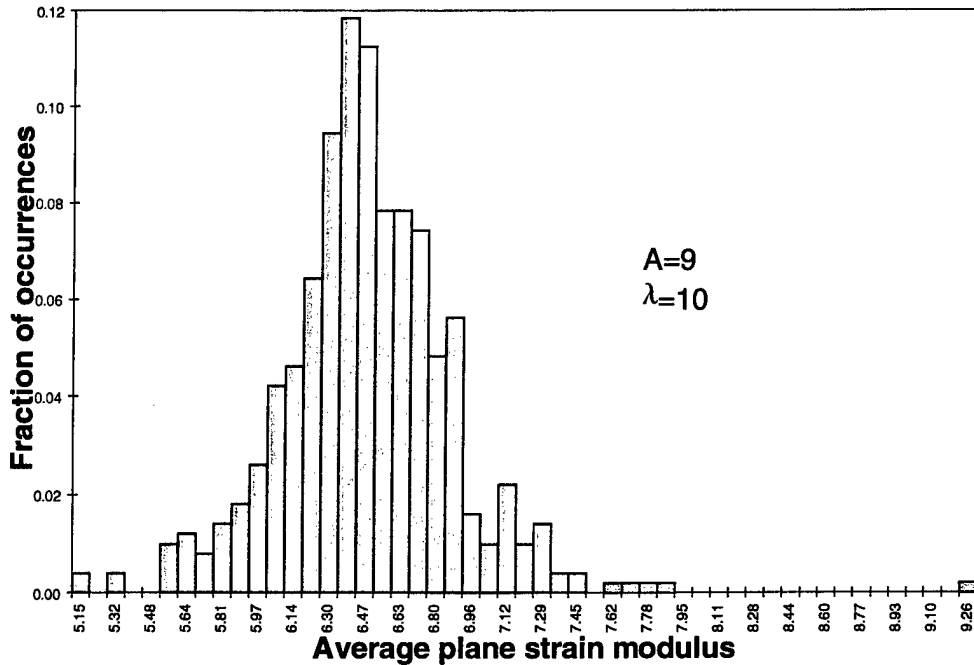


**Figure 3- Distributions of average plane strain modulus (Reference [1]).**

Figures 3 present, for highly anisotropic cubic and orthotropic crystals, the fraction of occurrences of the average plane strain modulus. It is observed that these are nearly symmetric about the mean, and are associated with a well defined peak. These distributions will be revisited later on as part of the discussion of the distributions of crack-tip parameters.

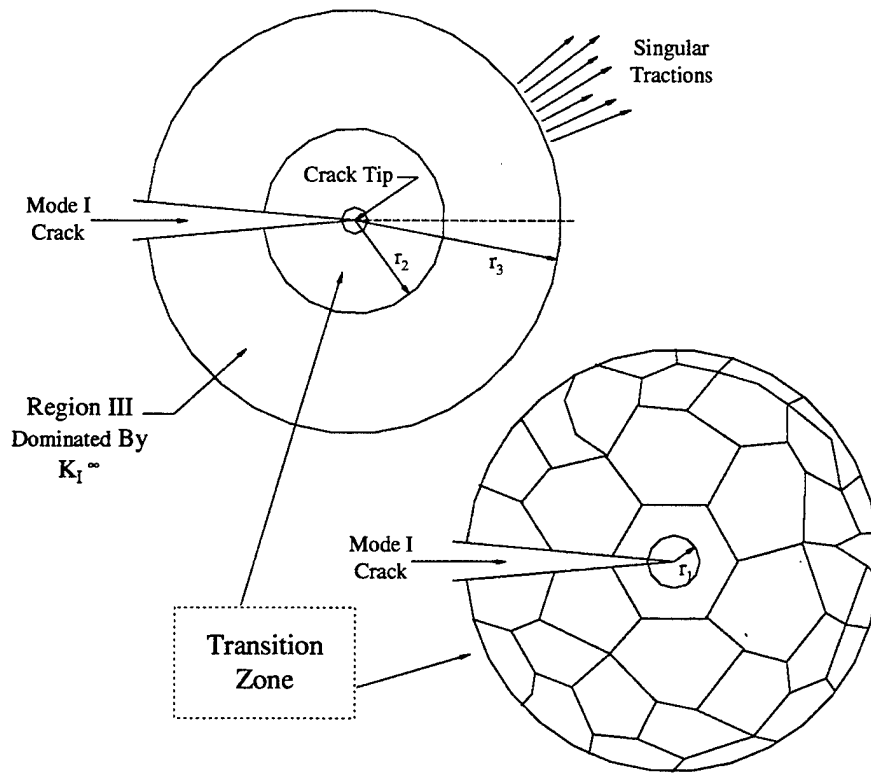


**Figure 4- A schematic representation of the regions dominated by distinct asymptotics (Reference [1]).**

The near-tip mechanics is summarized through the local-global representation of the cracked polycrystalline plane region shown in Figure 4. Let  $L$  represent the macroscopic length scale (crack length, uncracked ligament length, or any other relevant characteristic length), and recall that  $l$  represents the average grain size. For a given (deterministic) aggregate, it is expected that for large values of  $L/l$ , a near-tip, *small scale heterogeneous* zone exists, and arguments analogous to those presented for small scale process zones can be used to study the evolution of the near-tip stress fields (R. Ballarini, P.G. Charalambides and S. Islam, *International Journal of Fracture* 70, pp. 275-304, 1995; M. Jha, P.G. Charalambides and R. Ballarini, *Int. J. Solids Structures* 34, pp. 1849-1871, 1997; M. Jha, Ph.D. Dissertation, Department of Mechanical Engineering, University of Maryland at Baltimore County, 1997). For example, in small scale yielding, the near-tip plastic zones that develop with increasing load disturb the singular elastic solution giving rise to other near-tip asymptotics such as the HRR fields in deformation plasticity and power law hardening materials (J.R. Rice and G.F. Rosengren, *Journal of the Mechanics and Physics of Solids* 16 pp. 1-12, 1968; J.W. Hutchinson, *Journal of the Mechanics and Physics of Solids* 16 pp. 13-31, 1968). Similarly, it is expected that for the polycrystalline material, the heterogeneity perturbs the singular fields predicted by the homogenized asymptotic solution giving rise to dual asymptotics consistent with the dual length scales in the near-tip region. Moreover, for large  $L/l$ , the mechanical response



of the polycrystalline material at distances sufficiently away from the physical crack tip can be studied by ignoring the microstructure while employing the properties of a homogeneous isotropic medium instead. The latter properties can be calculated using the properties of the individual crystals through homogenization techniques; this paper uses the results presented in Figures 2. The stresses associated with the response of the homogeneous medium reflect average stress measures acting over the length of an appropriate microstructural unit cell. Under such conditions, the average unit cell stresses and displacements in the neighborhood of the crack tip are square root singular, and can be characterized via an isotropic macroscopic stress intensity factor  $K_I^\infty$ . These are given by (T.L. Anderson, *Fracture Mechanics Fundamentals and Applications, 2<sup>nd</sup> Edition, CRC Press, 1995*)

$$(7) \quad \begin{Bmatrix} \sigma_{xx} \\ \sigma_{yy} \\ \sigma_{xy} \end{Bmatrix} = \frac{K_I^\infty}{\sqrt{2\pi r}} \cos \frac{\theta}{2} \begin{Bmatrix} 1 - \sin \frac{\theta}{2} \sin \frac{3\theta}{2} \\ 1 + \sin \frac{\theta}{2} \sin \frac{3\theta}{2} \\ \sin \frac{\theta}{2} \cos \frac{3\theta}{2} \end{Bmatrix}$$

$$(8) \quad \begin{Bmatrix} u_x \\ u_y \end{Bmatrix} = \frac{K_I^\infty}{2G} \sqrt{\frac{r}{2\pi}} \begin{Bmatrix} \cos \frac{\theta}{2} \left[ \kappa - 1 + 2 \sin^2 \frac{\theta}{2} \right] \\ \sin \frac{\theta}{2} \left[ \kappa + 1 - 2 \cos^2 \frac{\theta}{2} \right] \end{Bmatrix}$$

where the  $r$ - $\theta$  polar coordinate is centered at the crack tip,  $G = E/2(1+\nu)$  is the shear modulus,  $\kappa = 3 - 4\nu$  for plane strain,  $\kappa = (3 - \nu)/(1 + \nu)$  for plane stress.

As shown in Figure 4, the outermost radius  $r_3$  from the physical crack tip of the zone dominated by  $K_I^\infty$  is expected to depend on the macroscopic characteristic length  $L$ , and in turn,  $r_3$  is some fraction of  $L$ . Thus, in a homogenized medium, region III as shown in Figure 4 is defined as being dominated by the isotropic singular stress field given by Equations (7) and (8). While this may be a realistic approximation for material systems with large  $L/l$  ratios, it is underscored that this approach may only provide useful stress field approximations at material points located within region III at distances from the physical crack tip which are much larger than the microstructural characteristic length  $l$ . As a result of the microstructure, it is clear that distinctly different asymptotics will dominate the mechanics at material points in region I (which contains the physical crack tip and extends to a distance  $r_1$ ), and that these will determine the crack propagation load and direction. The extent  $r_1$  of region I from the crack tip depends on the position of the crack tip relative to the adjacent crystal, and the degree of crystalline anisotropy. The distinct asymptotics dominating regions I and III discussed above are assumed to develop in heterogeneous systems with large  $L/l$ . In polycrystalline systems with nearly isotropic crystals, the dominance of region I would clearly prevail over region III, with  $r_1$  extending

to  $r_3$ . For high levels of anisotropy, the asymptotic fields in regions I and III are expected to be matched through other fields dominating the transition region II, extending from  $r_1$  to  $r_2$ .

In the immediate vicinity of the crack tip (region I), which is anisotropic, the stress and displacement components are given by (G.C. Sih, P.C. Paris and G.R. Irwin, *International Journal of Fracture Mechanics I*, pp. 189-203, 1965)

$$\begin{aligned} \begin{Bmatrix} \sigma_{xx} \\ \sigma_{yy} \\ \sigma_{xy} \end{Bmatrix} &= \frac{K_I'}{\sqrt{2\pi r}} \operatorname{Re} \left\{ \begin{array}{l} \frac{\mu_1 \mu_2}{\mu_1 - \mu_2} \left[ \frac{\mu_2}{\sqrt{\cos\theta + \mu_2 \sin\theta}} - \frac{\mu_1}{\sqrt{\cos\theta + \mu_1 \sin\theta}} \right] \\ 1 \\ \frac{\mu_1 \mu_2}{\mu_1 - \mu_2} \left[ \frac{\mu_1}{\sqrt{\cos\theta + \mu_2 \sin\theta}} - \frac{\mu_2}{\sqrt{\cos\theta + \mu_1 \sin\theta}} \right] \\ \frac{\mu_1 \mu_2}{\mu_1 - \mu_2} \left[ \frac{1}{\sqrt{\cos\theta + \mu_1 \sin\theta}} - \frac{1}{\sqrt{\cos\theta + \mu_2 \sin\theta}} \right] \end{array} \right\} \\ &+ \frac{K_{II}'}{\sqrt{2\pi r}} \operatorname{Re} \left\{ \begin{array}{l} \frac{1}{\mu_1 - \mu_2} \left[ \frac{\mu_2^2}{\sqrt{\cos\theta + \mu_2 \sin\theta}} - \frac{\mu_1^2}{\sqrt{\cos\theta + \mu_1 \sin\theta}} \right] \\ 1 \\ \frac{1}{\mu_1 - \mu_2} \left[ \frac{1}{\sqrt{\cos\theta + \mu_2 \sin\theta}} - \frac{1}{\sqrt{\cos\theta + \mu_1 \sin\theta}} \right] \\ \frac{1}{\mu_1 - \mu_2} \left[ \frac{\mu_1}{\sqrt{\cos\theta + \mu_1 \sin\theta}} - \frac{\mu_2}{\sqrt{\cos\theta + \mu_2 \sin\theta}} \right] \end{array} \right\} \end{aligned} \quad (9a)$$

$$\begin{aligned} \begin{Bmatrix} u_x \\ u_y \end{Bmatrix} &= K_I' \sqrt{\frac{r}{2\pi}} \operatorname{Re} \left\{ \begin{array}{l} \frac{1}{\mu_1 - \mu_2} \left[ \mu_1 p_2 (\cos\theta + \mu_2 \sin\theta)^{1/2} - \mu_2 p_1 (\cos\theta + \mu_1 \sin\theta)^{1/2} \right] \\ \frac{1}{\mu_1 - \mu_2} \left[ \mu_1 q_2 (\cos\theta + \mu_2 \sin\theta)^{1/2} - \mu_2 q_1 (\cos\theta + \mu_1 \sin\theta)^{1/2} \right] \end{array} \right\} \\ &+ K_{II}' \sqrt{\frac{r}{2\pi}} \operatorname{Re} \left\{ \begin{array}{l} \frac{1}{\mu_1 - \mu_2} \left[ p_2 (\cos\theta + \mu_2 \sin\theta)^{1/2} - p_1 (\cos\theta + \mu_1 \sin\theta)^{1/2} \right] \\ \frac{1}{\mu_1 - \mu_2} \left[ q_2 (\cos\theta + \mu_2 \sin\theta)^{1/2} - q_1 (\cos\theta + \mu_1 \sin\theta)^{1/2} \right] \end{array} \right\} \end{aligned} \quad (9b)$$

where Re (Im) denotes real (imaginary) part

$$p_j = c_{11} \mu_j^2 + c_{12} - c_{16} \mu_j, \quad j=1,2 \quad (10a)$$

$$q_j = c_{12} \mu_j + \frac{c_{22}}{\mu_j} - c_{26} \quad (10b)$$

the  $c_{ij}'$  are the flexibility coefficients (the components of the inverse of matrix  $C$  in Equation (4)), transformed to the global axes, and  $\mu_j$  are the roots (with positive imaginary parts) of the characteristic equation

$$c_{11}'\mu^4 - 2c_{16}'\mu^3 + (2c_{12}' + c_{44}')\mu^2 - 2c_{26}'\mu + c_{22}' = 0 \quad (11)$$

The energy release rate for self-similar extension is given as

$$G^I = -\frac{1}{2} K_I' c_{22}' \operatorname{Im} \left[ \frac{K_I'(\mu_1 + \mu_2) + K_{II}'}{\mu_1 \mu_2} \right] + \frac{1}{2} K_{II}' c_{11}' \operatorname{Im} [K_{II}'(\mu_1 + \mu_2) + K_I' \mu_1 \mu_2] \quad (12)$$

Because the crystals in a real material are randomly orientated, the behavior of the stress intensity factors and of the stresses in the vicinity of the crack is more complicated; these physical parameters can only be discussed in terms of their probability distributions. Indeed, the scatter in the stresses ahead of the crack may be large enough to render the previous near-tip discussion irrelevant. In other words, distinct asymptotics may not be observed, as will be subsequently shown.

### Near-tip finite element model

Consider the near-tip plane strain region shown in Figure 1. The physical dimensions of this zone are  $R \times R$  (with  $R=1$ ) such that  $R \leq r_3$ , where  $r_3$  signifies the boundary of region III consistent with Figure 4. In this model, the Poisson-Voronoi tessellation approximation of the polycrystalline structure is retained. The region under consideration includes the crack tip, whose position within the crystal is a random variable. The crack surfaces are traction-free. Mode-I loading is applied by prescribing, along the boundary of the region, the displacements in Equations (8). It should be understood that this model does not incorporate finite geometry characteristics. In other words,  $R$  does not directly represent a macroscopic length, rather it provides an indirect measure of a macroscopic characteristic length. The only requirement on  $R$  is that stated earlier, i.e.  $R \leq r_3$ . Various morphologies corresponding to different  $L/l$  are modeled by changing the number of crystals,  $n$ , within the modeled region. It is expected that this approach will capture the various near-tip asymptotics and the transitional characteristics from region I to region III through region II. The relation between  $R$  and  $L$  could be quantified only by modeling specific finite geometries.

The microscopic stress intensity factors are calculated using the displacement correlation technique (*R.S. Barsoum, International Journal of Numerical Methods in Engineering 11, p. 85, 1977; A.R. Ingraffea and C. Manu, International Journal of Numerical Methods in Engineering 15, pp. 1427-1445, 1980*), which involves equating the square root portion of the finite element displacement interpolation of the crack opening and crack sliding displacements, with the analytical values given by Equation (9b). These in turn are used to calculate the local energy release rate.

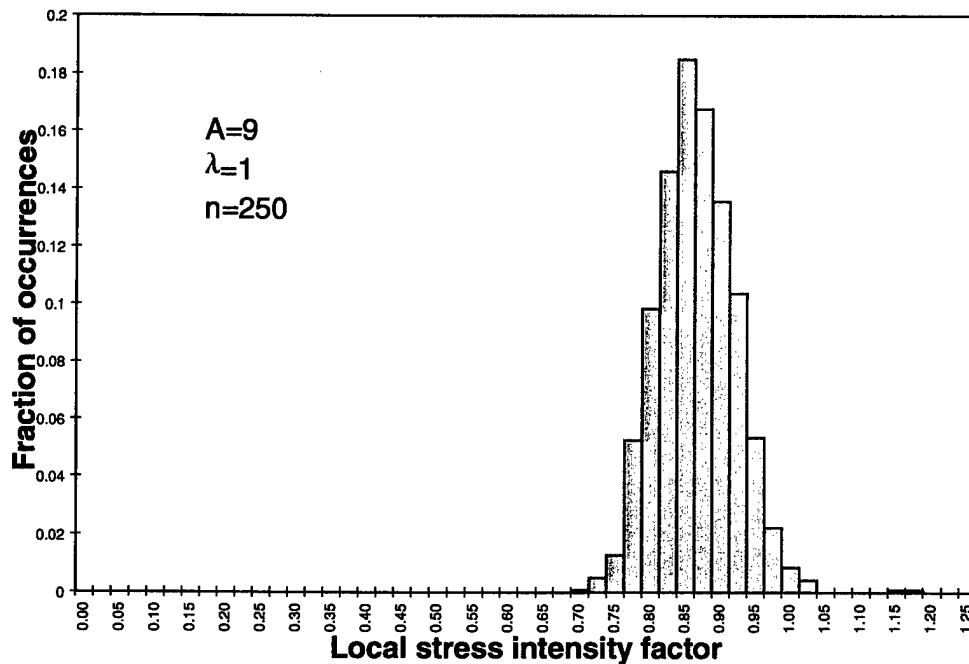
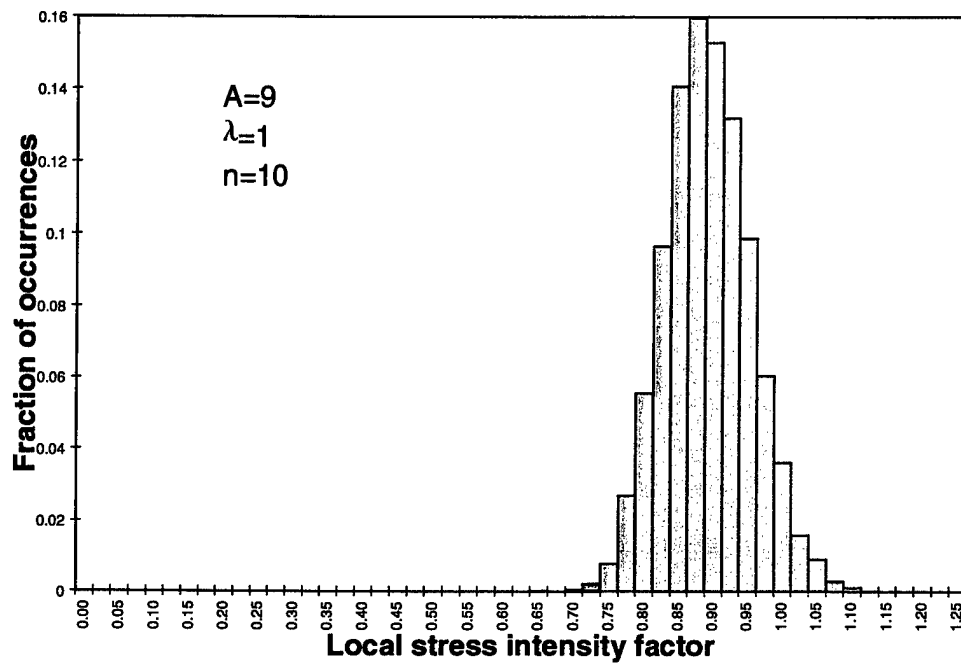


Figure 5- Fraction of occurrences of local stress intensity factor for highly anisotropic cubic crystals (Reference [1]).

Results

The average and standard deviation (denoted by subscripts *avg* and *sd*, respectively) of  $K \equiv K'_l/K'_r$  and  $G \equiv G'_l/G'_r$  are summarized in Table 1. For  $m$  simulations (the results presented in Table 1 correspond to  $m=200-400$ ), the standard

deviation of  $x$  is defined as  $\sqrt{\frac{\sum x^2}{m} - \frac{mx_{avg}^2}{m-1}}$ . The results for the isotropic crystals ( $A=\lambda=1$ ) show that the errors in the calculated stress intensity factors and energy release rates are on the order of a few percent.

For cubic crystals ( $\lambda=1$ ), the effects of anisotropy and heterogeneity on the crack-tip parameters are relatively small. Consider the results for  $n=500$ ; for the highest levels of anisotropy considered ( $A=9$ ,  $\bar{\nu}=0.4$ ), the average stress intensity factor is slightly reduced to  $\approx 0.87 \pm 0.06$  ( $\pm x$  represents  $\pm$  one standard deviation), and the average energy release rate is reduced to  $\approx 0.85 \pm 0.12$ . Moreover, the results are not sensitive to  $n$ . Polycrystalline silicon is defined by  $A=1.65$ ,  $\bar{\nu}=0.282$ ; for all values of  $n$ , the average stress intensity factor is  $\approx 0.93 \pm 0.02$ , and the average energy release rate is  $\approx 0.91 \pm 0.03$ .

The results for orthotropic crystals show that anisotropy and heterogeneity produce significant effects for highly anisotropic crystals. For example, if  $n=500$ ,  $A=9$ ,  $\lambda=10$ , and  $\bar{\nu}=0.4$ , the stress intensity factor is  $\approx 0.98 \pm 0.29$ , and the energy release rate is  $\approx 0.89 \pm 0.30$ . Moreover, for highly anisotropic crystals, the results are significantly influenced by the number of grains; for  $n=10$ , the standard deviations of the stress intensity factor and energy release rate, for the previous example, increase to 0.39 and 0.49, respectively.

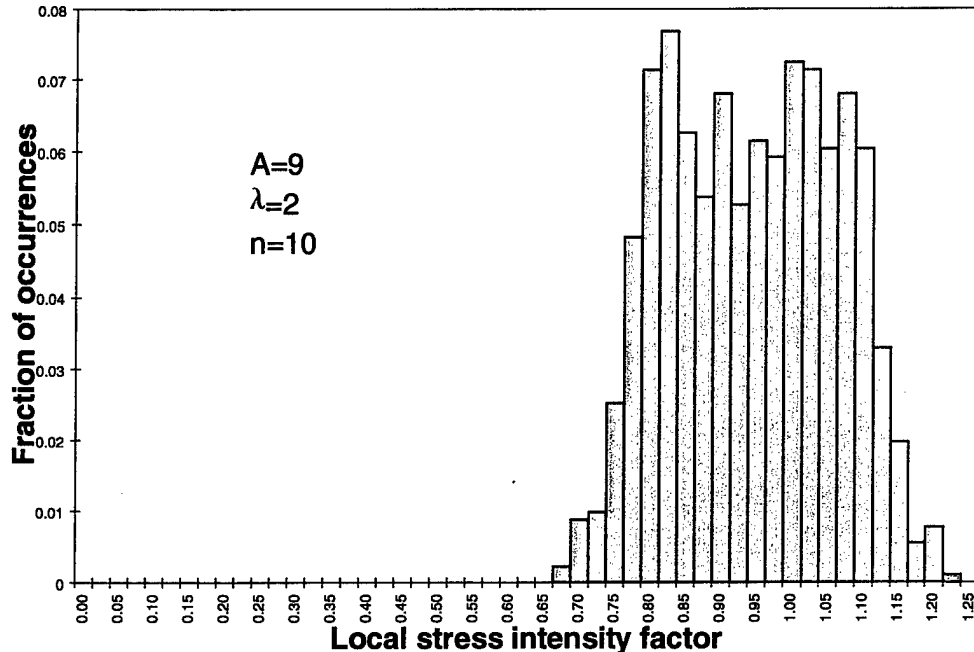
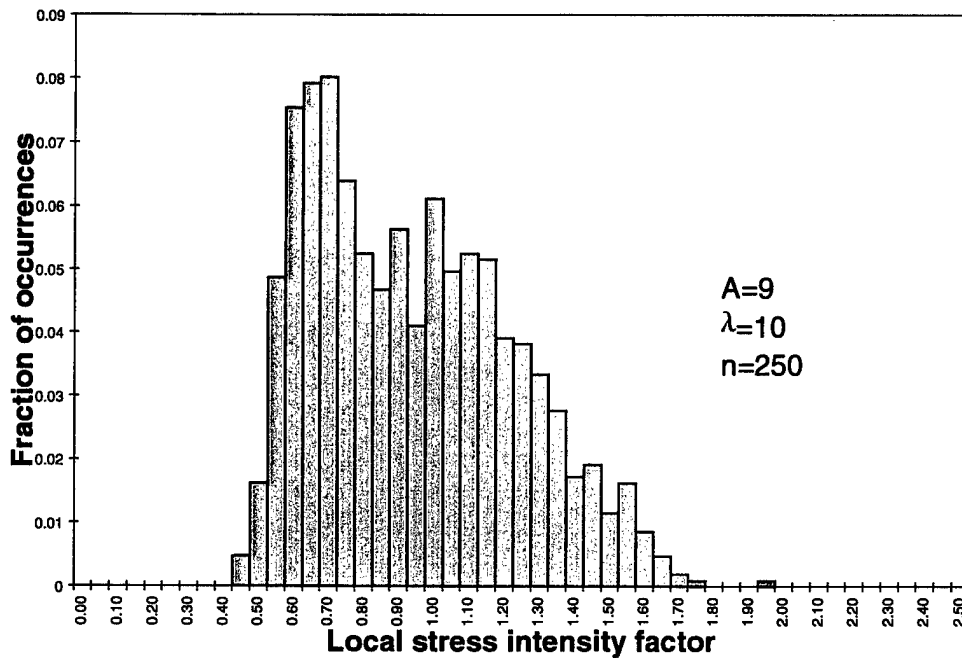
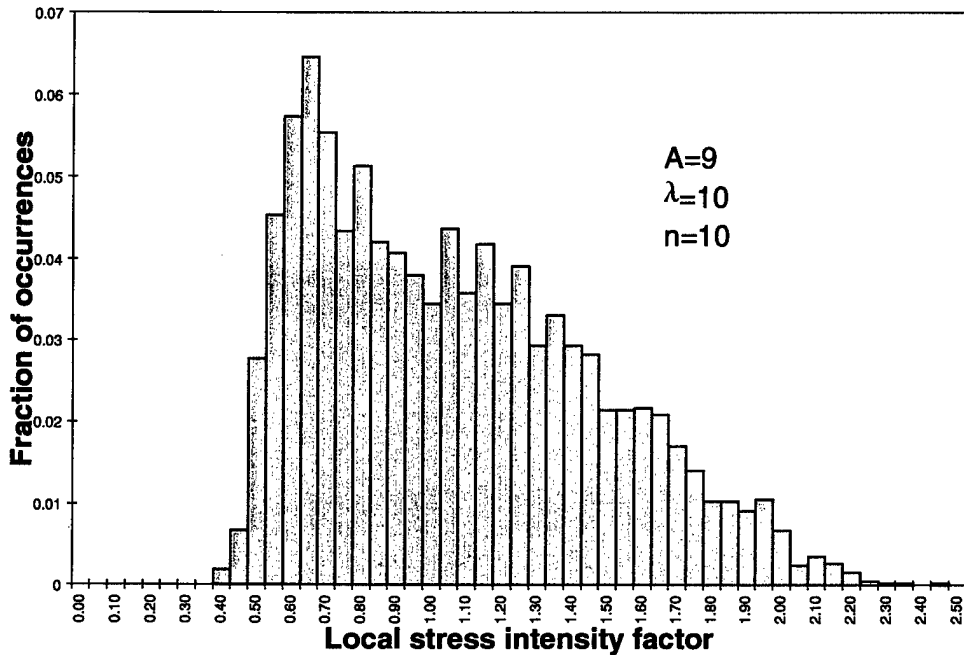


Figure 6- Fraction of occurrences of local stress intensity factor for highly anisotropic, slightly orthotropic crystals (Reference [1]).

Figures 5-7 show, respectively, the fraction of occurrences of the local Mode-I stress intensity factor for highly anisotropic cubic crystals, highly anisotropic "slightly" orthotropic crystals, and high anisotropic orthotropic crystals. It is observed that for cubic crystals, the distribution is relatively narrow and nearly symmetric about the mean, while for orthotropic crystals the distribution is wider and not symmetric. Moreover, for orthotropic crystals, a small population of realizations is associated with stress intensity factors that are more than double of the nominal. Recall that the distributions of the nominal elastic constants are symmetric for both cubic and orthotropic crystals.



**Figure 7- Fraction of occurrences of local stress intensity factor  
for highly anisotropic orthotropic crystals (Reference [1]).**

The scatter of the normalized stress  $\sigma \equiv \frac{\sqrt{2\pi R}\sigma_{yy}}{K_I^\infty}$  ahead of the crack for highly

anisotropic cubic crystals, and highly anisotropic orthotropic crystals, are shown in Figures 8 and 9, respectively. In these figures the distance from the crack tip,  $r$ , actually represents the nondimensional distance  $r/R$ , with  $R=1$ . It is observed that for cubic and orthotropic crystals, even at high levels of anisotropy, the dual length scale asymptotics disappear within the scatter; the stress is square root singular, with upper and lower bounds modulated by the deviation of the local stress intensity factor from the mean. Furthermore, the distribution of stress is nearly independent of the number of crystals  $n$ .

It is important to note that the effects of anisotropy are expected to increase drastically if (1) cracking within crystals or along grain boundaries is taken into account, and (2) if the structure is comprised of a very few grains. The authors are currently calculating these effects.



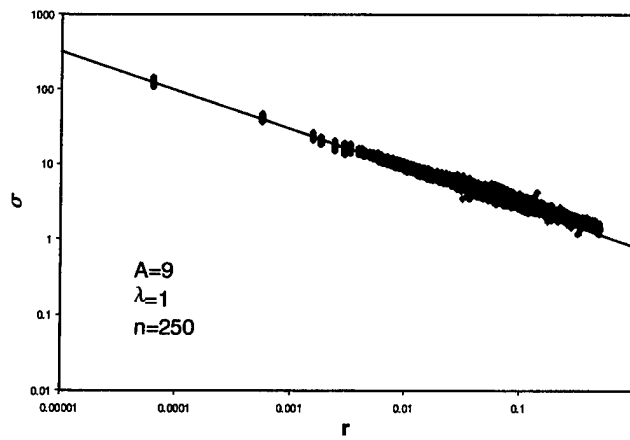
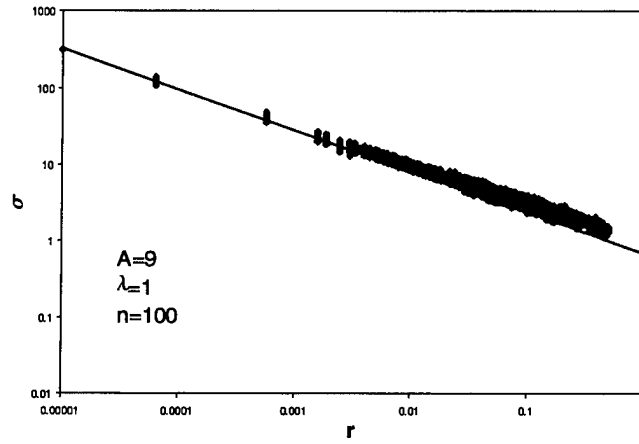
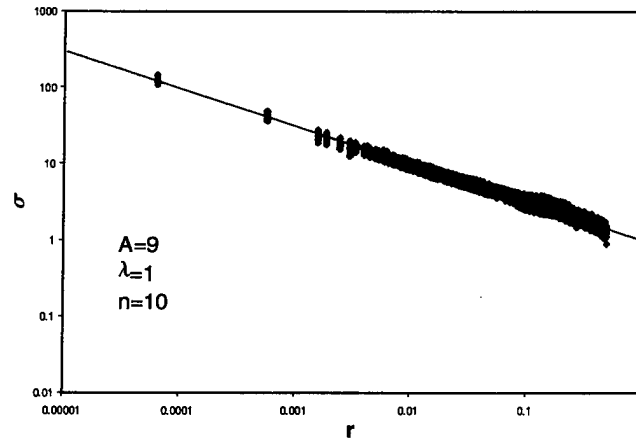


Figure 8- Scatter of normalized stress ahead of crack for several values of  $n$  ( $\lambda=1$ ,  $A=9$ ,  $\bar{\nu}=0.4$ ) (Reference [1]).

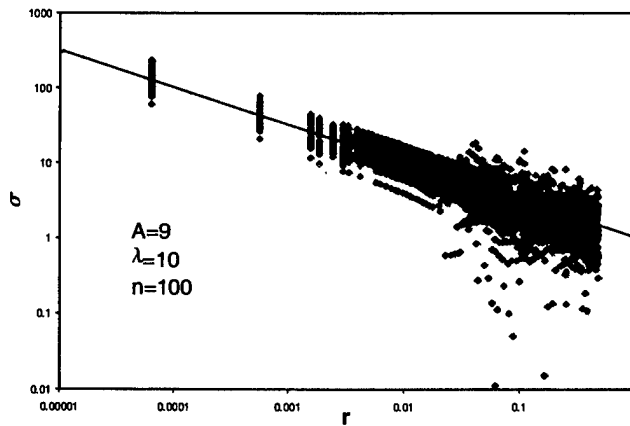
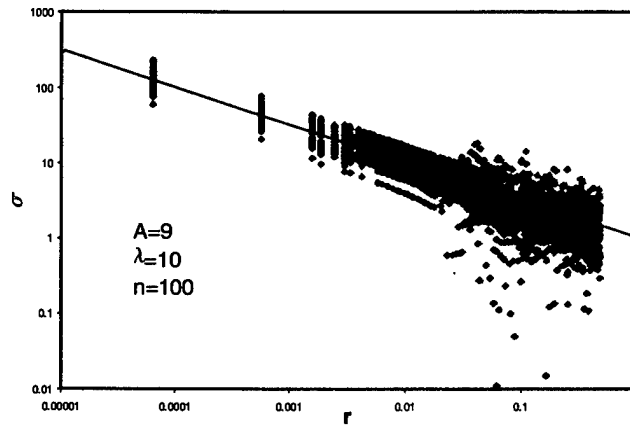
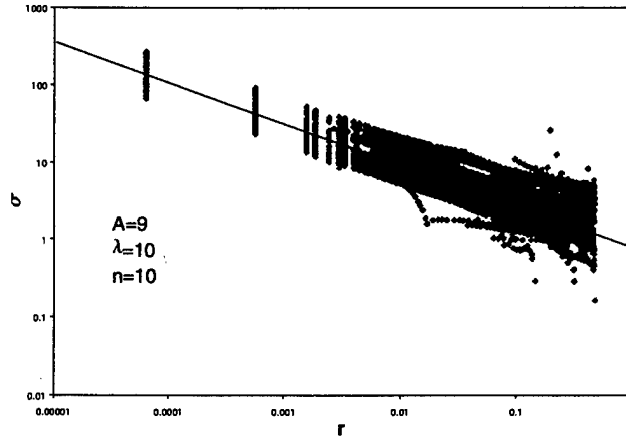


Figure 9- Scatter of normalized stress ahead of crack for several values of  $n$  ( $\lambda=10$ ,  $A=9$ ,  $\bar{\nu}=0.4$ ) (Reference [1]).

A	$\bar{\nu}$	$\lambda$	n	$K_{avg}$	$G_{avg}$	$K_{sd}$	$G_{sd}$
1	0	1	10	0.9846	0.9696	0.00692	0.01398
1	0	1	100	0.9848	0.9699	0.00664	0.01377

1	0	1	250	0.9831	0.9666	0.00405	0.0077
1	0	1	500	0.9839	0.968	7.4E-05	0.00015
1	0	2	10	0.9969	0.9818	0.11	0.1203
1	0	2	100	0.9792	0.9575	0.08638	0.08356
1	0	2	250	0.9938	0.9651	0.083	0.07982
1	0	2	500	0.9852	0.9566	0.08823	0.08569
1	0	10	10	1.035	0.9767	0.3407	0.4097
1	0	10	100	0.992	0.8872	0.2745	0.2537
1	0	10	250	0.9601	0.8665	0.2644	0.2299
1	0	10	500	0.9303	0.8395	0.2191	0.1949
1	0.2	2	10	0.9853	0.9647	0.1117	0.1224
1	0.2	2	100	0.9778	0.9574	0.08969	0.09426
1	0.2	2	250	0.9835	0.96	0.09177	0.08819
1	0.2	2	500	0.9771	0.948	0.08347	0.08796
1	0.2	10	10	1.022	0.9687	0.3543	0.4279
1	0.2	10	100	0.9242	0.8389	0.2285	0.2121
1	0.2	10	250	0.9484	0.8393	0.2372	0.2289
1	0.2	10	500	0.9043	0.802	0.2329	0.1912
1	0.4	2	10	0.9558	0.9216	0.1005	0.1155
1	0.4	2	100	0.9485	0.9153	0.08509	0.09749
1	0.4	2	250	0.9417	0.9011	0.0798	0.08157
1	0.4	2	500	0.9489	0.9047	0.08087	0.07973
1	0.4	10	10	0.8912	0.8295	0.2974	0.3599
1	0.4	10	100	0.7999	0.6814	0.1737	0.1962
1	0.4	10	250	0.8087	0.6948	0.1591	0.1861
1	0.4	10	500	0.821	0.7024	0.16	0.1941
3	0	1	10	0.9727	0.9617	0.02514	0.04963
3	0	1	100	0.968	0.9521	0.0216	0.04259
3	0	1	250	0.968	0.9519	0.01872	0.03676
3	0	1	500	0.9675	0.951	0.01883	0.03715
3	0	2	10	0.9855	0.9766	0.1248	0.1485
3	0	2	100	0.978	0.9529	0.105	0.1255
3	0	2	250	0.9705	0.9406	0.1081	0.1212
3	0	2	500	0.966	0.9424	0.1034	0.1123
3	0	10	10	1.061	1.005	0.3984	0.4662
3	0	10	100	0.9493	0.8667	0.2769	0.2766
3	0	10	250	0.9744	0.8869	0.272	0.264
3	0	10	500	0.9866	0.8936	0.2886	0.2839

3	0.2	1	10	0.9732	0.9681	0.02889	0.05746
3	0.2	1	100	0.9729	0.9615	0.1134	0.1235
3	0.2	1	250	0.965	0.9515	0.02521	0.04959
3	0.2	1	500	0.9631	0.9478	0.0253	0.04997
3	0.2	2	10	0.9922	0.9742	0.1181	0.1344
3	0.2	2	100	0.9708	0.9498	0.09824	0.1031
3	0.2	2	250	0.9827	0.9554	0.09156	0.09461
3	0.2	2	500	0.9822	0.9566	0.09097	0.09325
3	0.2	10	10	1.073	1.02	0.3866	0.4397
3	0.2	10	100	1.007	0.9227	0.2873	0.3059
3	0.2	10	250	0.9962	0.9105	0.2977	0.283
3	0.2	10	500	0.9834	0.9068	0.2634	0.2585
3	0.4	1	10	0.9597	0.9542	0.06316	0.118
3	0.4	1	100	0.9431	0.9221	0.05847	0.1119
3	0.4	1	250	0.9481	0.9313	0.05737	0.1074
3	0.4	1	500	0.9577	0.9498	0.0766	0.1456
3	0.4	2	10	0.9774	0.9557	0.1104	0.1238
3	0.4	2	100	0.9764	0.9425	0.09122	0.101
3	0.4	2	250	0.9766	0.9468	0.08848	0.09471
3	0.4	2	500	0.9688	0.9418	0.08373	0.08225
3	0.4	10	10	1.037	0.9866	0.3548	0.3915
3	0.4	10	100	0.9849	0.8779	0.2811	0.2693
3	0.4	10	250	0.9347	0.8322	0.245	0.211
3	0.4	10	500	0.9376	0.8399	0.2447	0.2211
5	0	1	10	0.9711	0.9648	0.04471	0.07122
5	0	1	100	0.9567	0.9364	0.03651	0.05684
5	0	1	250	0.9592	0.9412	0.03872	0.05649
5	0	1	500	0.9604	0.9398	0.04123	0.05033
5	0	2	10	0.9809	0.9708	0.122	0.1472
5	0	2	100	0.9621	0.9425	0.1037	0.119
5	0	2	250	0.9638	0.9488	0.1051	0.1296
5	0	2	500	0.95	0.932	0.09389	0.1007
5	0	10	10	1.055	1.022	0.4035	0.4877
5	0	10	100	0.9945	0.9171	0.3043	0.3055
5	0	10	250	0.9684	0.9034	0.2968	0.3025
5	0	10	500	0.9475	0.8725	0.2836	0.2766
5	0.2	1	10	0.9593	0.9577	0.03936	0.07897
5	0.2	1	100	0.9506	0.9396	0.0345	0.06848

5	0.2	1	250	0.9524	0.9431	0.03362	0.06683
5	0.2	1	500	0.952	0.9325	0.1455	0.1505
5	0.2	2	10	0.9759	0.9687	0.1191	0.1415
5	0.2	2	100	0.9581	0.9437	0.1003	0.1194
5	0.2	2	250	0.9723	0.9534	0.09271	0.1078
5	0.2	2	500	0.9712	0.9447	0.08757	0.101
5	0.2	10	10	1.077	1.063	0.4268	0.5295
5	0.2	10	100	0.9624	0.8901	0.2908	0.3069
5	0.2	10	250	0.9841	0.892	0.286	0.27
5	0.2	10	500	0.9676	0.8927	0.2917	0.2902
5	0.4	1	10	0.9303	0.9299	0.04891	0.09878
5	0.4	1	100	0.9123	0.8944	0.05005	0.09767
5	0.4	1	250	0.9143	0.8976	0.04615	0.09006
5	0.4	1	500	0.9229	0.9153	0.05063	0.1015
5	0.4	2	10	0.9762	0.9643	0.1165	0.1416
5	0.4	2	100	0.9662	0.9458	0.09975	0.1183
5	0.4	2	250	0.9558	0.9297	0.09285	0.1054
5	0.4	2	500	0.9677	0.9406	0.09325	0.1083
5	0.4	10	10	1.105	1.054	0.3949	0.466
5	0.4	10	100	0.9975	0.8837	0.2743	0.2613
5	0.4	10	250	0.9845	0.8991	0.2702	0.2659
5	0.4	10	500	0.9684	0.8628	0.2486	0.2308
9	0	1	10	0.9579	0.956	0.04177	0.08366
9	0	1	100	0.9386	0.9162	0.02891	0.0563
9	0	1	250	0.9372	0.9134	0.02816	0.05491
9	0	1	500	0.9444	0.9254	0.04802	0.07167
9	0	2	10	0.9678	0.9596	0.1291	0.1637
9	0	2	100	0.9439	0.922	0.1051	0.1243
9	0	2	250	0.9269	0.9031	0.09488	0.1116
9	0	2	500	0.9367	0.9143	0.09702	0.1162
9	0	10	10	1.038	1.041	0.4261	0.5412
9	0	10	100	0.9199	0.8478	0.3257	0.3755
9	0	10	250	0.9021	0.8214	0.2705	0.2901
9	0	10	500	0.9342	0.8535	0.3035	0.3358
9	0.2	1	10	0.94	0.948	0.04818	0.09767
9	0.2	1	100	0.9255	0.9172	0.04194	0.08291
9	0.2	1	250	0.9188	0.9035	0.03489	0.06888
9	0.2	1	500	0.9227	0.9111	0.03523	0.06972

9	0.2	2	10	0.9676	0.9695	0.1692	0.2056
9	0.2	2	100	0.9378	0.9171	0.0987	0.123
9	0.2	2	250	0.935	0.9131	0.1016	0.1204
9	0.2	2	500	0.9463	0.9269	0.09811	0.1199
9	0.2	10	10	1.073	1.073	0.4394	0.5444
9	0.2	10	100	0.9414	0.866	0.3021	0.31
9	0.2	10	250	0.9385	0.8598	0.2882	0.3136
9	0.2	10	500	0.921	0.8624	0.305	0.3383
9	0.4	1	10	0.9006	0.9132	0.05919	0.1214
9	0.4	1	100	0.8835	0.8786	0.06104	0.1216
9	0.4	1	250	0.875	0.8609	0.054	0.1073
9	0.4	1	500	0.869	0.8504	0.06049	0.1189
9	0.4	2	10	0.963	0.9636	0.127	0.1614
9	0.4	2	100	0.9376	0.9131	0.1017	0.1272
9	0.4	2	250	0.9387	0.9093	0.09749	0.1212
9	0.4	2	500	0.9396	0.9168	0.09734	0.1183
9	0.4	10	10	1.089	1.064	0.3915	0.4936
9	0.4	10	100	0.9735	0.9041	0.3105	0.318
9	0.4	10	250	1.009	0.9125	0.2921	0.304
9	0.4	10	500	0.9823	0.8908	0.2944	0.3047

**Table 1- Calculated crack tip parameters (Reference [1]).**

### 3. REFERENCE [2]

This paper, as far as the scientist knows, is the first to show that heterogeneity produces a weak size effect in polycrystalline films, and instead induces statistical effects controlled by a small number of grains surrounding the crack tip. The authors accomplish this through several models, the first analytic, the second finite element based.

The material that was considered is S2 ice, which is formed by columnar grains, as shown in Figure 10. The global cartesian axes are defined such that the  $x_3$  axis is along the thickness direction, and the negative  $x_1$  axis is along the crack line. The grains are assumed to be hexagonal (transversely isotropic) crystals whose  $c$ -axes are randomly oriented in the  $x_3 = 0$  plane. Thus a sufficiently large sheet is transversely isotropic with the symmetry axis along the  $x_3$  axis. The local coordinates within a grain are  $x_3'$ , which coincides with the  $c$ -axis, and the  $x_1'$ , which coincides with the global  $x_3$  axis.

#### Asymptotic analysis

The authors first formulate an asymptotic statistical estimate of  $\Delta K$ , which represents the stress intensity factor induced by grains of diameter  $d$  that lie in the region between two quasi-circular contours of radius  $Nd$  and  $N'd$  centered at the crack tip. The estimate is valid for sufficiently large  $N$  and involves the limit as  $N'$  approaches infinity. The material outside this region is assumed homogeneous.

$\Delta K$  is computed as follows. Each grain is replaced with an equivalent transformation strain, and the stress intensity factor it induces,  $\delta K$  is calculated. Then, using methods of probability theory,  $\Delta K$  is calculated as the sum over  $\delta K$ 's. The equivalent transformation strain  $\gamma$  (tensor) of a reference grain with stiffness tensor  $\hat{C}$ , embedded in a material with stiffness tensor  $C$ , is determined from Eshelby's equivalence condition (*T. Mura, Micromechanics of Defects in Solids, Martinus Nijhoff Publishers, The Hague, 1982*), which is written in terms of the ambient strain field  $\varepsilon$  and Eshelby's tensor  $S$ , as

$$\hat{C}(\varepsilon + S\gamma) = C(\varepsilon + S\gamma - \gamma) \quad (13)$$

Because the stress field induced by  $\gamma$  at a distance significantly larger than  $d$  is of interest, the authors did not calculate the exact solution of Equation (13). Rather they developed an approximate solution by assuming that (1) the reference grain is circular, (2) the elastic interaction between grains is neglected, and (3) the variation of  $\varepsilon$  within the reference grain is neglected. These assumptions, together with the assumption that the ambient field is fully described by a Mode-I loading with stress intensity factor  $K$ , provide the closed form solution

$$\gamma = \frac{K}{\sqrt{2\pi r}} (C - CS + \hat{C}S)^{-1} (C - \hat{C})C^{-1}\tau(\theta)$$

(14)

where  $S$  is Eshelby's tensor of a long cylinder, the components of  $\tau$  are the angular functions in Equations (7) associated with a Mode-I plane strain solution, and  $r$  and  $\theta$  are the polar coordinates of the grain center (Figure 12(b)). As pointed out by the authors, strictly speaking, in Equation (6) both  $S$  and  $\tau$  must be derived as solutions of anisotropic elasticity. One can prove that the symmetry of  $C$  is such that  $\delta K$  can be calculated using solutions of isotropic elasticity. Therefore  $C$  is redefined as an isotropic stiffness tensor whose constants  $E$  and  $\nu$  coincide with the corresponding in-plane constants of the original transversely isotropic  $C$  (and  $S$  and  $\tau$  are redefined as the solutions corresponding to the new  $C$ ). The constants  $E$  and  $\nu$  were calculated using the self-consistent approach outlined by Wang and Schapery (L. Wang and R.A. Schapery, "Prediction of elastic and viscoelastic properties of columnar ice," in J.P. Dempsey and Y.D.S. Rajapakse (eds.), *Ice Mechanics 1995, AMD-Vol. 207, The American Society of Mechanical Engineers, New York, pp. 33-48*). The expressions for all tensors can be recovered in Reference [2].

As shown by Hutchinson (J.W. Hutchinson, "On steady quasi-static crack growth," Report AFOSR-TR74-1042, 1974) and Lambropoulos (J.C. Lambropoulos, "Shear, shape and orientation effects in transformation toughening," *International Journal of Solids and Structures, Vol. 22, pp. 1083-1106, 1986*)

$$\delta K = \frac{\sqrt{\pi}}{16\sqrt{2}} \frac{E}{1-\nu^2} d^2 r^{-3/2} \mu \bullet \gamma$$

(15)

where  $\mu$  is given in Reference [2].

The authors sum over all crystals, assume that  $\lambda$  is a uniformly distributed random variable, and employ principles of probability theory to derive a simplified relation for the probability that  $\Delta K/K$  is less than a certain number. The details are not reproduced here. For S2 ice, which is slightly anisotropic, their model predicts that for  $N=6$ , the probability that  $\Delta K/K < 0.1$  is above 0.99; for  $N=9$ , it is above 0.9999. These calculations show that in this material remote grains cannot induce significant stress intensity factors, and consequently the heterogeneity produces a weak size effect. To check whether highly anisotropic crystals produce larger perturbations of the applied stress intensity factor, they calculated their model for a  $\psi$ -fold reduction in one of their elastic constants. Table 2 shows, for selected values of  $\psi$ , the number of grains  $N$  needed to ensure that  $\Delta K/K < 0.1$  with a probability equal to 0.99.



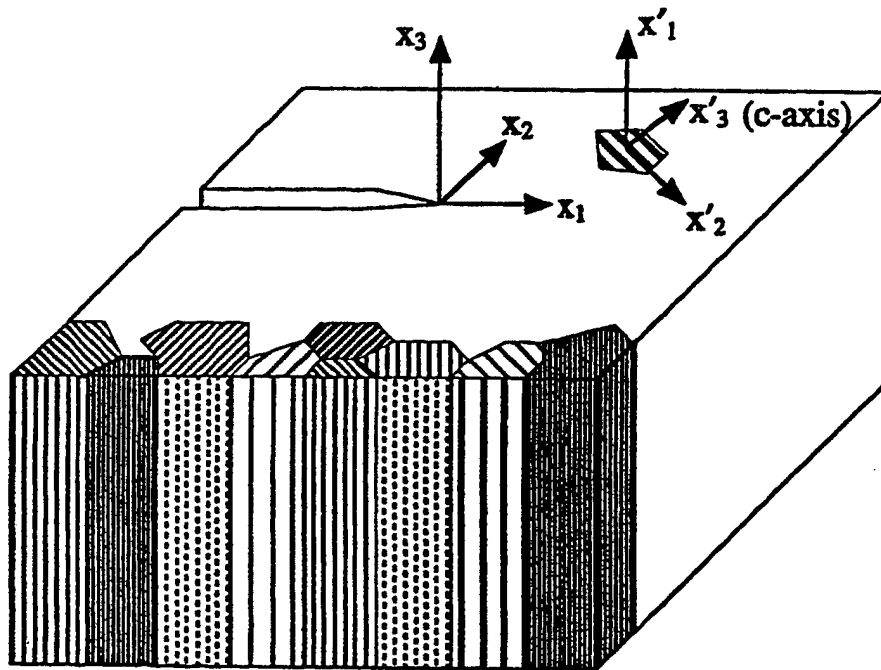


Figure 10- Fracture specimen with columnar microstructure (Reference [2]).

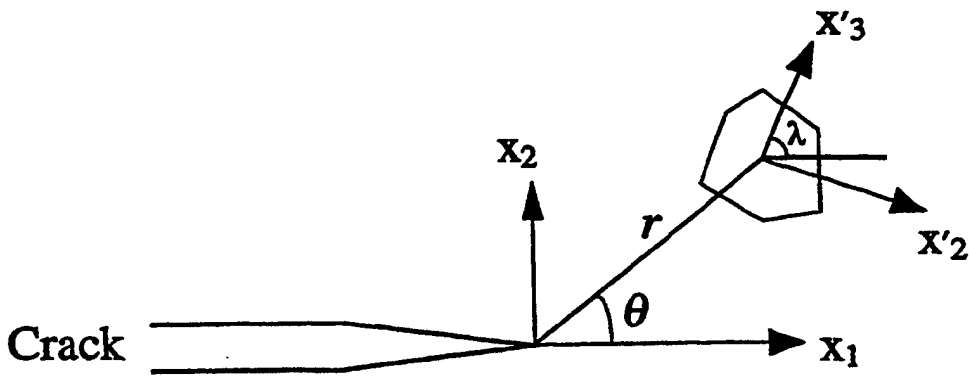
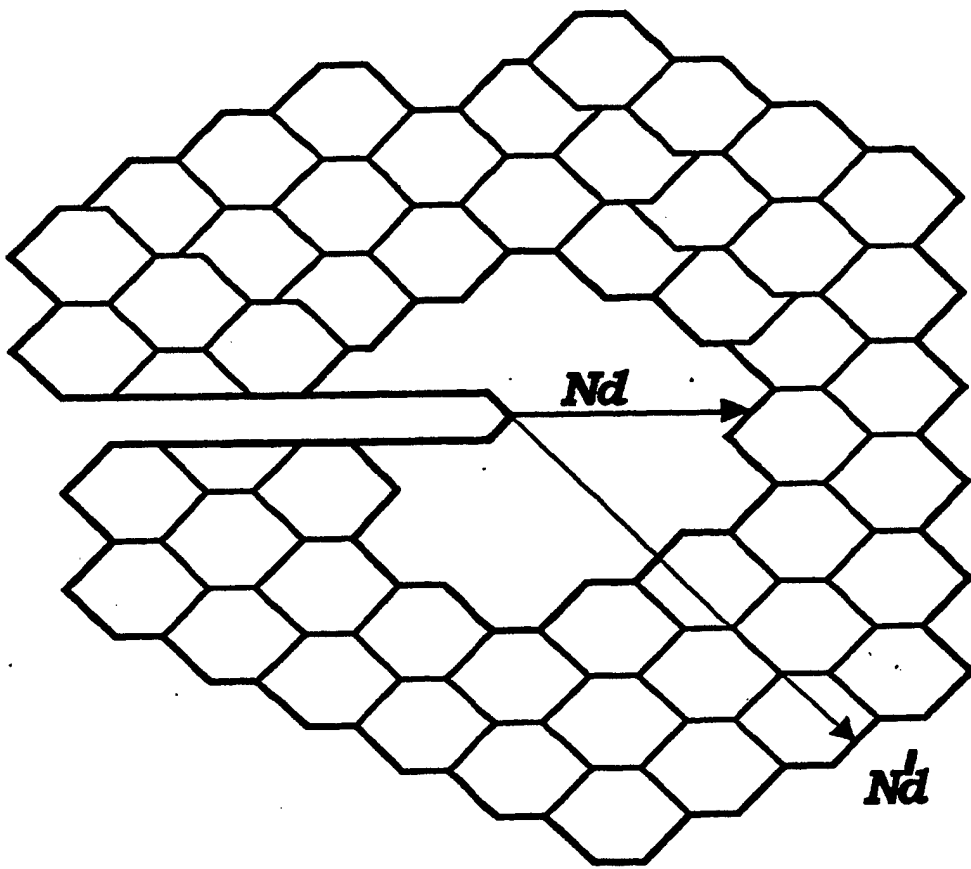
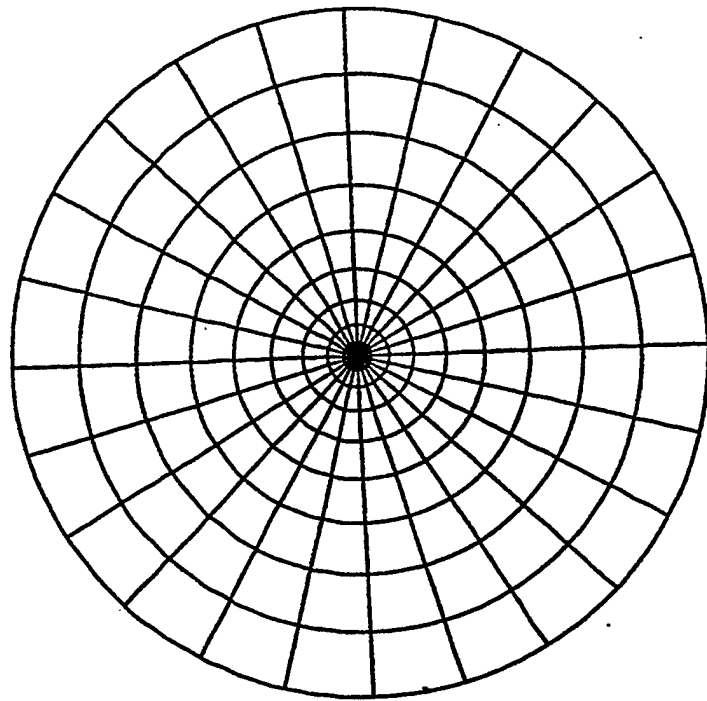


Figure 11- Analysis of  $\Delta K$  induced by remote grains: (a) specimen (b) reference grain (Reference[2]).

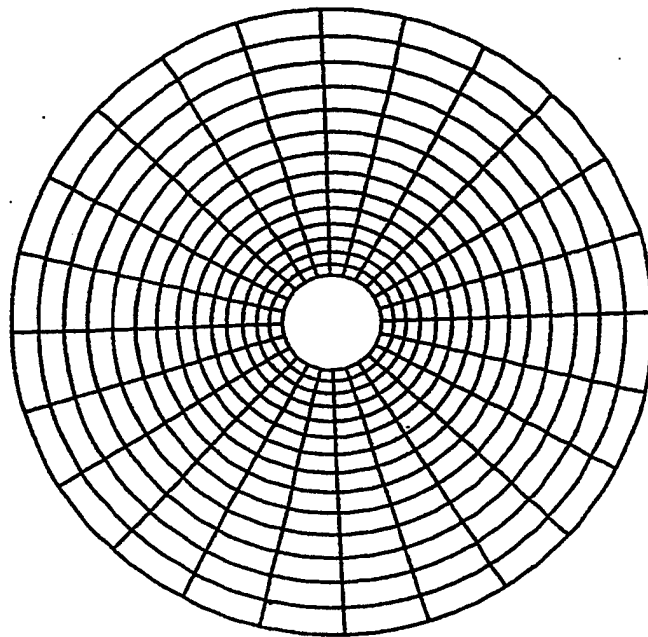
## Numerical estimates

In Reference [2] the authors also conducted finite element calculations that reinforce the notion that grains remote from the crack tip do not induce significant stress intensity factors. The polycrystalline microstructure was approximated and analyzed as a circular cylindrical grain centered at the crack tip, surrounded by quadrilateral grains (Figure 12). In each numerical experiment, the  $c$ -axis of the grain that contains the crack tip was fixed, while the  $c$ -axes of the remaining grains were either aligned with it, or randomly oriented.

The results are presented in Figure 13. The solid curve corresponds to S2 ice, while the dashed and dotted lines correspond to  $\psi=2$  and  $\psi=5$ , respectively. Remarkably, each of these curves represents four realizations, one of them being the experiment for which the  $c$ -axes of all grains are aligned, and the other three the experiments with random directions of the grains surrounding the one centered at the crack tip. These results provide additional evidence that the grains other than the one that contains the crack tip cannot significantly perturb the applied stress intensity factor.



(a)



(b)

Figure 12- Finite element mesh: (a) grain that contains the crack tip (b) remaining grains (Reference [2]).

$\psi$	N
1	6
2	8
5	13
10	33
20	266
100	588

Table 2- Evaluation of the size effect for various levels of anisotropy (Reference [2]).

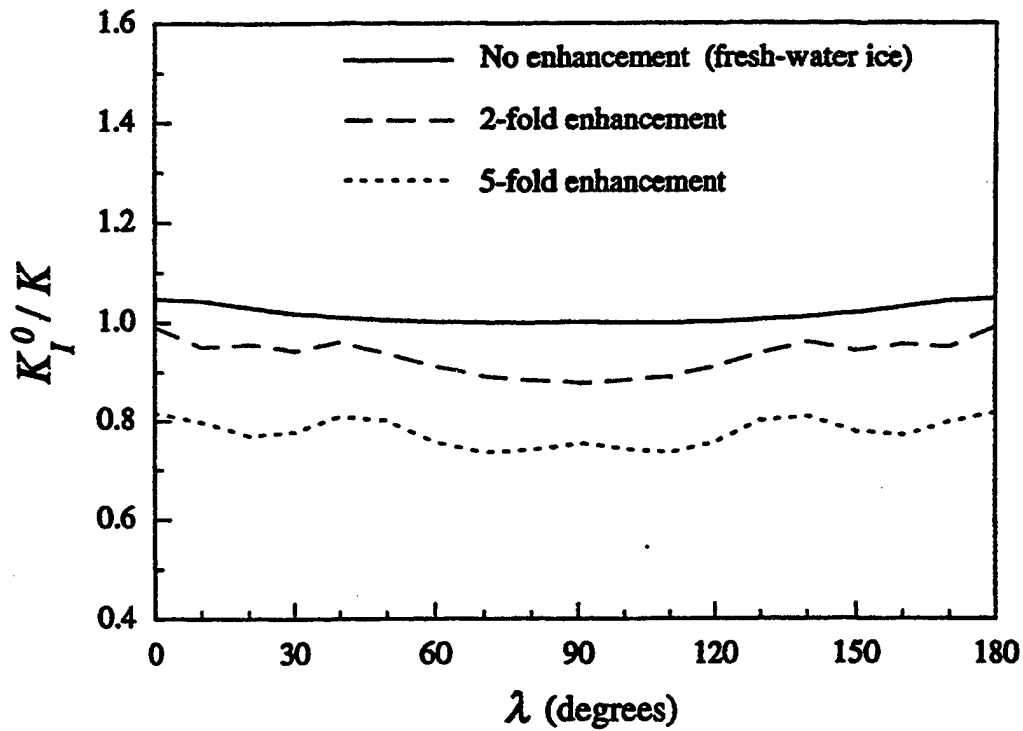


Figure 13- Normalized local stress intensity factor as a function of the angle  $\lambda$  (Reference [2]).

## **PART IV**

# **SUGGESTIONS FOR FUTURE RESEARCH**

The work described in this report is representative of the state-of-the-art of experimental characterization and theoretical modeling of the mechanical properties of poly-Si used for MEMS. It is the opinion of the scientist that the quality of the reviewed work is excellent. However, much more needs to be done if mechanical reliability of MEMS devices is to be predicted (and hopefully guaranteed).

The following research is suggested.

1. Performance criteria should be defined. At this point of the game, it is not known what potential loading and environmental conditions MEMS devices are expected to survive. Grant it these should soon be understood as new applications are envisioned. Continuous communication between device developers (who will dictate performance requirements) and mechanical characterization types is paramount.
2. Robust tests should be developed for measuring residual stresses, elastic constants, tensile strength, fracture toughness, fatigue crack growth rates, etc.. Different experimental techniques should be used for quantifying the effects of specimen geometry and loading. Those techniques that are deemed the most robust should be considered as candidates for standards. To this end, the use of round-robin testing should be encouraged. As mentioned in Chapter 1, one such exercise (funded by the Air Force Office of Scientific Research) has recently been completed. This involved measuring the Young's modulus and tensile strength of poly-Si films fabricated at MCNC. The participants included W.N. Sharpe and coworkers at JHU, George Johnson and coworkers at BSAC, S. Brown and coworkers at Exponent, and W. Knauss and coworkers at Caltech. The results are presented in Table 1 (private communication with W.N. Sharpe). Note that the Caltech results are not yet available, and that the test methods used to generate the results have been described in this report. The scientist does not have information about the resonant bending tests performed by the group at Exponent. The importance of this program cannot be overstated. For example, it resulted in a discussion at the Atlanta Spring 1998 ASTM meeting in of Committee E08.01 (an education-focused committee that serves at the current home base of MEMS materials testing) that launched a round robin program for measuring residual stresses in films produced at MCNC. This program is underway.

**Table 1- Results of round-robin testing program (courtesy of W.N. Sharpe)**

	BSAC	Exponent	JHU (using second generation system)	JHU (using second generation system)
Film thickness (microns)	2.0	2.0	1.5	3.5
E (GPa)	174	137	136	142
Strength (GPa)	2.8	2.7	1.3	1.3

3. A sufficiently large data base for mechanical properties as functions of processing techniques should be developed using the most robust procedures.
4. Mechanisms of fatigue, stress corrosion and fracture toughness have to be studied and understood. It's been convincingly demonstrated that poly-Si is prone to static fatigue. Crack growth rates should be measured for materials processed under different conditions and operating under different environments. Some evidence was presented in Chapter 7 suggesting that poly-Si may fatigue in the absence of humidity. This is but one example of an unexpected mechanism; others may appear in micron size structures.
5. Theoretical models should be developed for characterizing and predicting crack growth rates.
6. Improved statistical models should be developed for predicting the scatter in elastic constants of poly-Si and other material systems.
7. Statistical fracture models should be explored for predicting the scatter in toughness of poly-Si components comprised of a few grains.
8. Tasks 1-7 should be performed for other materials that are currently used to fabricate MEMS, and for the new material systems that will be developed for applications that current materials cannot be used (high temperature, for example).
9. Experiments should be designed to explore potential failure mechanisms in these new material systems, including interfacial fracture and creep in the SiC-poly-Si structural system developed by M. Mehregany and coworkers (*K.N. Vinod, C.A. Zorman, A. Yasseen and M. Mehregany, "Fabrication of low defect density 3C-SiC on SiO<sub>2</sub> structures using wafer bonding techniques," Journal of Electronic Materials, in press*) at CWRU and shown in the Figure.





**Figure 1- XTEM image of SiC (for high temperature applications) grown on as-deposited poly-Si (reference provided in text).**